TAMPEREEN TEKNILLINEN YLIOPISTO
TAMPERE UNIVERSITY OF TECHNOLOGY

ALI ABDOLLAHZADEH

ASSESSING DATA ACQUISITION APPROACHES IN ELECTRON TOMOGRAPHY

Master of Science thesis

Examiners: Prof. Ulla Ruotsalainen
M.Sc. Erman Acar
Examiners and topic approved by the
Faculty Council of Natural Sciences
on 7 th of October 2015

ABSTRACT

ALI ABDOLLAHZADEH: Assessing Data Acquisition Approaches in Electron Tomography
Tampere University of Technology
Master of Science thesis, 83 pages, 3 appendix pages
25.01.2016
Master's Degree Programme in Biomedical Engineering
Major: Bio-Informatics
Examiners: Prof. Ulla Ruotsalainen
M.Sc. Erman Acar
Keywords: Electron Microscopy, Electron Tomography, Image reconstruction, Saxton method, angle and dose distribution approaches

Electron tomography (ET) is a technique to reveal the interior structures of organic -subcellular macro molecules- and inorganic materials from their 2D cross sectional transmission electron microscope (TEM) projections. However, restricted radiation dose due to specimen damage and blind region of angular sampling as a result of physical constraints deteriorate the quality of the resultant tomograms. Typically, electron tomograms suffer from low signal to noise ratio (SNR) and elongation artifact in the direction of electron radiation. Different studies propose methods to tackle the constraints of ET in the data acquisition stage. This thesis is a comparative study among different data acquisition models by analyzing the resultant tomogram of each method quantitatively. We implement each model with a TEM simulator and compare the tomograms by their root mean square (RMS) and resolution. Results of TEM settings indicate that 1) reducing the acceleration voltage and increasing the defocus value intensifies the contrast. 2) Diminishing the objective diaphragm size reduces the brightness of the projections. Comparing data acquisition models states that 1) cosine model of dose distribution homogenizes the SNR of sinograms and compared to the conventional methods enhances the resolution of the tomograms. 2) Employing Saxton model for angular sampling boosts the resolution and declines the elongation artifact. 3) Combination of the cosine method of dose distribution and Saxton's model promotes the resolution, RMS value and elongation artifact significantly: resolution enhanced 1.81 times compared to the constant dose and angle distribution models in Z-direction. To conclude, emphasis on the SNR and sampling frequency of highly tilted angles outperforms the conventional data acquisition approaches qualitatively and quantitatively.

PREFACE

This thesis is accomplished in Methods and Models for Biological Signals and Images (M2oBSI) research group at the Department of Signal Processing, Tampere University of Technology, Finland between June 2015 and January 2016 under the supervision of Prof. Ulla Ruotsalainen and M.Sc. Erman Acar.

Here, I would like to express my deep gratitude to Professor Ulla Ruotsalainen, Assistant Professor Sari Peltonen and M.sc. Erman Acar for providing me a unique opportunity to conduct my research in the field of medical image processing in their group. I am thankful for their advices, insightful comments and encouragements. My special thanks goes to Erman, who has been a great supervisor and friend; I sincerely appreciate his suggestions, ideas and friendship.

I wish to thank my family for their love and encouragement, especially my parents Asef and Fatemeh who always supported me unconditionally. I am always grateful for every moment of their being.

Last but not least, I thank Lucia Gräschke for her constant support, love and company during the days I developed this work.

Ali Abdollahzadeh
Tampere, 25.01.2016

Haukamenkatu 57 1 E,
33745 Tampere, Finland
+358-414963073
ali.abdollahzadeh@student.tut.fi

TABLE OF CONTENTS

1. Introduction 1

2. Image Formation of Biological Specimens in Transmission Electron Microscopy 3

2.1 Electron Gun 3

2.2 Condenser Lenses 4

2.3 Electron Specimen Interaction 6

2.4 Mean Free Path 8

2.5 Objective Diaphragm 9

2.6 Contrast Transfer Function 10

2.7 Bright Filed and Dark Field Imaging 13

2.7.1 Bright Filed (BF) Imaging 13

2.7.2 Dark Filed (DF) Imaging 14

2.8 Scattering Contrast 15

2.9 Phase Contrast 15

2.10 Image Formation 16

2.10.1 Detector Plane 16

2.10.2 Detector Response 16

2.10.3 Detector Blurring 17

2.10.4 Shot Noise 18

3. Low Dose Imaging in Cryo Electron Tomography 20

3.1 Acceleration Voltage 20

3.2 Magnification 22

3.3 Defocus 22

3.4 Dose and Electron Radiation Damage 23

3.5 Angular Sampling 24

3.6 Exposure Time 26

4. Tomographic Image Reconstruction 28

4.1 Projection Vector - Radon Transform 28

4.2 Fourier Slice Theorem 30

4.3 Reconstruction Techniques 31

4.3.1 Direct Fourier Reconstruction (DFR) 32

4.3.2 Filtered Back Projection (FBP) 33

4.3.3 Algebraic Reconstruction Methods (ARM) 35

4.3.4 Statistical Reconstruction Methods 37

5. Resolution Measurement Approaches 40

5.1 Resolution Measurement Approaches 40

5.1.1 Fourier Ring/Shell Correlation 42

5.1.2 Even/Odd Fourier Shell Correlation 42

5.1.3 Noise-Compensated Leave-One-Out (NLOO) 43

5.1.4 Effective Estimation of Resolution in Incoherent Electron Tomography 46

6. Materials and Methods 49

6.1 Numerical Phantoms 49

6.1.1 MS2 Bacteriophage Phantom 49

6.1.2 Cellular Texture Phantom 51

6.2 Detector Calibration 52

6.3 High Resolution Imaging 53

6.4 Medium Resolution Imaging 54

7. Results and Discussions 56

7.1 Acceleration Voltage 56

7.2 Defocus Value 58

7.3 Objective Diaphragm 61

7.4 Dose Distribution 63
7.5 Reconstruction of Different Data Acquisition Methods 66
7.6 Quantitative Assessment 70
7.6.1 Root Mean Square (RMS) 70
7.6.2 FRC_{ref} 70
7.6.3 Resolution Measurement in Z-Direction 72
8. Conclusions 76
References 78
APPENDIX - Dose and Angle distributions 84

LIST OF ABBREVIATIONS AND SYMBOLS

1D	One-Dimensional
2D	Two-Dimensional
3D	Three-Dimensional
BF	Bright Field
CCD	Charge Coupled Diode
CMC	Carbon Micro-Coil
CT	Computerized Tomography
CTF	Contrast Transfer Function
DF	Dark Field
DFR	Direct Fourier Reconstruction
DFT	Discrete Fourier Transform
DQE	Detective Quantum Efficiency
EM	Electron Microscopy
ET	Electron Tomography
FBP	Filtered Back Projection
FOV	Field Of View
FRC	Fourier Ring correlation
FSC	Fourier Shell correlation
$\mathrm{FSC}_{e/o}$	Fourier Shell correlation$_{even/odd}$
$\mathrm{FSC}ref$	Fourier Shell correlation$_{reference}$
FT	Fourier Transform
FWHM	Full Width at Half Maximum
ML-EM	Maximum Likelihood Expectation Maximization
MRC	Medical Research Council
MRP	Median Root Prior
MS2	Male-Specific (bacteriophage) 2
MTF	Modular Transfer Function
NLOO	Noise-Compensated Leave-One-Out
NMR	Nuclear Magnetic Resonance
PDB	Protein Data Bank
PDF	Probability Distribution Function
PET	Positron Emission Tomography
PSF	Point Spread Function

RMS	Root Mean Square
SART	Simultaneously Algebraic Reconstruction Technique
SIRT	Simultaneously Iterative Reconstruction Technique
SNR	Signal to Noise Ratio
SPA	Single Particle Analysis
TEM	Transmission Electron Tomography

A	Atomic weight
$C1, C2$	Condenser lens
C_{DQE}	DQE value
C_{gain}	Gain value
D	Sample thickness at zero tilt angle
E	Electric filed
E_F	Fermi energy
$F(u, v)$	2D Fourier transform of
N_A	Avogadro's number
N_p	Number of input projections
$P_\phi(s)$	Projection vector
$R(k)$	Annular zone in frequency domain
U_{det}	Formed image on detector plane
U_{sc}	Scattered electron wave
$W(x, y)$	Wave function
Z_1, Z_2, τ	Sigmoid function factor
$a, b, c, \gamma 1, \gamma 2$	MTF factor
d	Radiation angle in dark field imaging
$d\sigma, d\Omega$	Differential cross section
dz	Thickness
$f(x, y)$	Two dimensional object function
$\hat{f}(x, y)$	Reconstructed image
k	Radial frequency
l	Shortest distance between electron and nucleus
s	Distance from the origin of the coordinate system
t	Time
w	Width of the potential barrier at the metal-vacuum boundary
Γ	Mean of electrons hitting a detector in an interval t
ΔF	Defocus value
Λ	Effective mean free path
Φ_w	Work function
α	Tilt angle
β	Regularization factor
δ	Dirac delta function
ε	Noise
θ	Deflection angle
λ	Mean electron rate

ϖ	system matrix
ρ	Density
σ_{el}	Elastic cross section
σ_{inel}	Inelastic cross section
σ_t	Total cross section
ϕ	Projection angle
φ	Phase shift
ω	Frequency

1. INTRODUCTION

Taking 2D cross sectional projections around an object with penetrative waves enables us to reconstruct and reveal the interior structures of the object through a technique called tomography. To obtain the projections in a full angular range, either of the specimen or detector-source pair should circulate around a single axis. In case of electron tomography, the employed projections are acquired from a transmission electron microscope. Generally TEM projections are acquired by irradiating a thin specimen with a beam of electrons accelerated with a certain voltage. The electrons which pass the specimen form an image on a detector plane and reveal the structures of the object from a specific angle [1]. Acquired projections from different angles around the specimen are reconstructed to generate an electron tomogram. Currently, high resolution electron microscopes can produce images close to atomic resolutions <10 Å. However in case of biological specimens, resolution of an electron tomogram is restricted, since physical constraints such as specimen damage and angular range of data acquisition are inherited with the electron tomography [2].

Different studies aim to tackle the constraints of the electron tomography in both data acquisition and image reconstruction stages. Transmission Electron Microscopy -Physics of Image Formation [3], and Electron Tomography -Methods for Three-Dimensional Visualization of Structures in the Cell [4] are two principle references comprising of comprehensive chapters in electron microscopy and electron tomography respectively. This thesis is a comparative study among different data acquisition approaches and evaluates the effect of each method on the reconstructed electron tomograms in terms of RMS value and resolution. The main methods applied in this work such as Saxton model of angle distribution and cosine model of dose distribution are introduced and employed in different experiments already [2, 5, 6]. Nevertheless the quantitative evaluation of their mere impact on the reconstruction has not been assessed by the time of writing this work.

This thesis is structured as follows; in chapter 2 different concepts of electron mi-

croscopy, together with the procedure of image formation is introduced. In chapter 3 low dose electron microscopy and different data acquisition methods are discussed. Chapter 4 is an introduction to image reconstruction and it's most frequent algorithms. Chapter 5 explains diverse methods of resolution measurement in electron tomography. In chapter 6 two numerical phantoms are described, adjustments employed in the TEM simulator are demonstrated and details of the experiments are defined. Chapter 7 presents and discusses the results of the experiments qualitatively and quantitatively and finally chapter 8 makes a conclusion from the acquired results.

2. IMAGE FORMATION OF BIOLOGICAL SPECIMENS IN TRANSMISSION ELECTRON MICROSCOPY

In Transmission Electron Microscopy, a thin specimen is radiated by a beam of electrons accelerated with a certain voltage. Electrons are emitted from a thermionic, Schottky, or field emission electron gun. Condenser lenses system provides user to control the quality of illumination and the area of illumination on the specimen. Collision of electrons with the specimen leads to an interaction between them; some electrons scatter elastically, some scatter inelastically, and the rest pass the specimen without any deflection. Emerged electrons from the specimen will face a diaphragm, with a very small aperture in between. Non-deflected and low angle scattered electrons pass the diaphragm aperture and the rest -highly scattered electrons- will be absorbed by the diaphragm. Then, the transmitted electrons are focused with three to eight magnetic lenses to form an image on a fluorescent screen at the end of their path. Image formed on the fluorescent screen is digitally recorded with a detector plane, depicting the electric potential distribution of the specimen [7].

In this chapter, we will clarify the mentioned concepts which contribute in forming an image in TEM.

2.1 Electron Gun

To generate a beam of electrons, an electron gun is employed. The electron beam is supposed to have high brightness, and spatial/temporal coherency. In order to emit an electron, it should receive sufficient energy to overcome its work function[1] Φ_w (see Fig. 2.1). Thermionic, and Schottky electron guns provide the energy by heating the cathode. In field emission electron gun, a very strong electric field $|E| \geq$

[1]Minimum thermodynamic energy needed to remove an electron from a solid to a point in the vacuum just outside the solid surface at absolute zero [8].

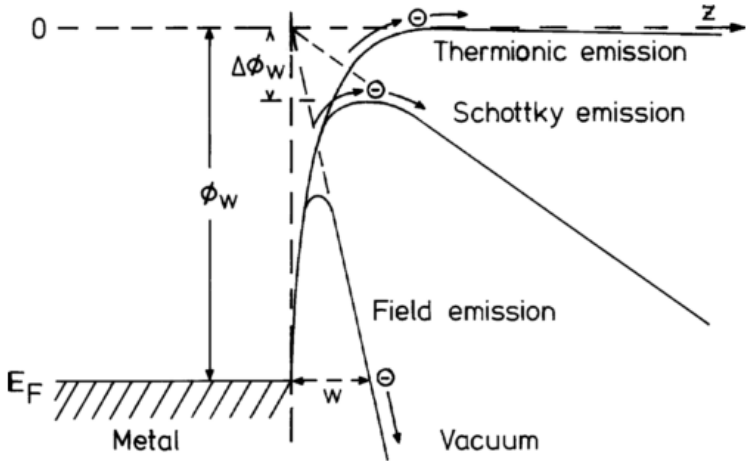

Figure 2.1 *Electrons at metal-vacuum boundary with energies almost close to Fermi energy (E_F) need to overcome the barriers of Φ_w and $\Phi_w - \Delta\Phi_w$ for thermionic and Schottky emissions respectively or can tunnel through the barrier of width w for field emission [9].*

$109\,\mathrm{V\,m^{-1}}$, very good vacuum, and a tip cathode with a radius $\leq 0.1\,\mu\mathrm{m}$ is required to extract an electron from the metal filament by quantum-mechanic tunneling effect. The advantage of field emission electron gun is within its high brightness, and acceptable spatial/temporal coherency. Also, as it can be observed in Fig. 2.1, electrons should overcome the work function of Φ_w and $\Phi_w - \Delta\Phi_w$ for thermionic and Schottky emissions respectively, but for field emission, electrons at the Fermi level can penetrate the potential barrier w by the quantum-mechanical tunneling effect [9]. In reality, obtaining a perfect spatial/temporal coherent illumination is not possible and the illumination is partially coherent, since the electrons do not contain an equal amount of energy and the size of electron source is not infinitely small. Partial coherency affects the image formation equations by introducing exponential envelops to the system transfer function; attenuation of high spatial frequencies due to both partial spatial, and partial temporal coherency [10].

2.2 Condenser Lenses

Focusing the electron beam on the desired area of the specimen and controlling the illumination aperture to obtain sufficient image intensity requires condenser lenses. The condenser system comprises of at least two lenses and a condenser aperture. The first lens C_1 is applied for narrowing -demagnification- of gun cross over (see Fig. 2.2a) and the second one C_2 is required for converging the beam and defining

the diameter of illuminated area on the specimen. Based on how C_2 is excited, beam convergence on the specimen can occur in one of these modes: in-focus, over-focus or defocus. Figure 2.2b-c illustrate the contribution of C2 lens to illumination area on the specimen. Moving from in-focus mode to over-focus or defocus modes increases the diameter of illumination over specimen. Condenser aperture is usually located below the C_2 lens and depending on the desired magnification/resolution, the condenser aperture size is changing from 1 milliradian to ≤ 0.1 for medium to high resolutions respectively [9].

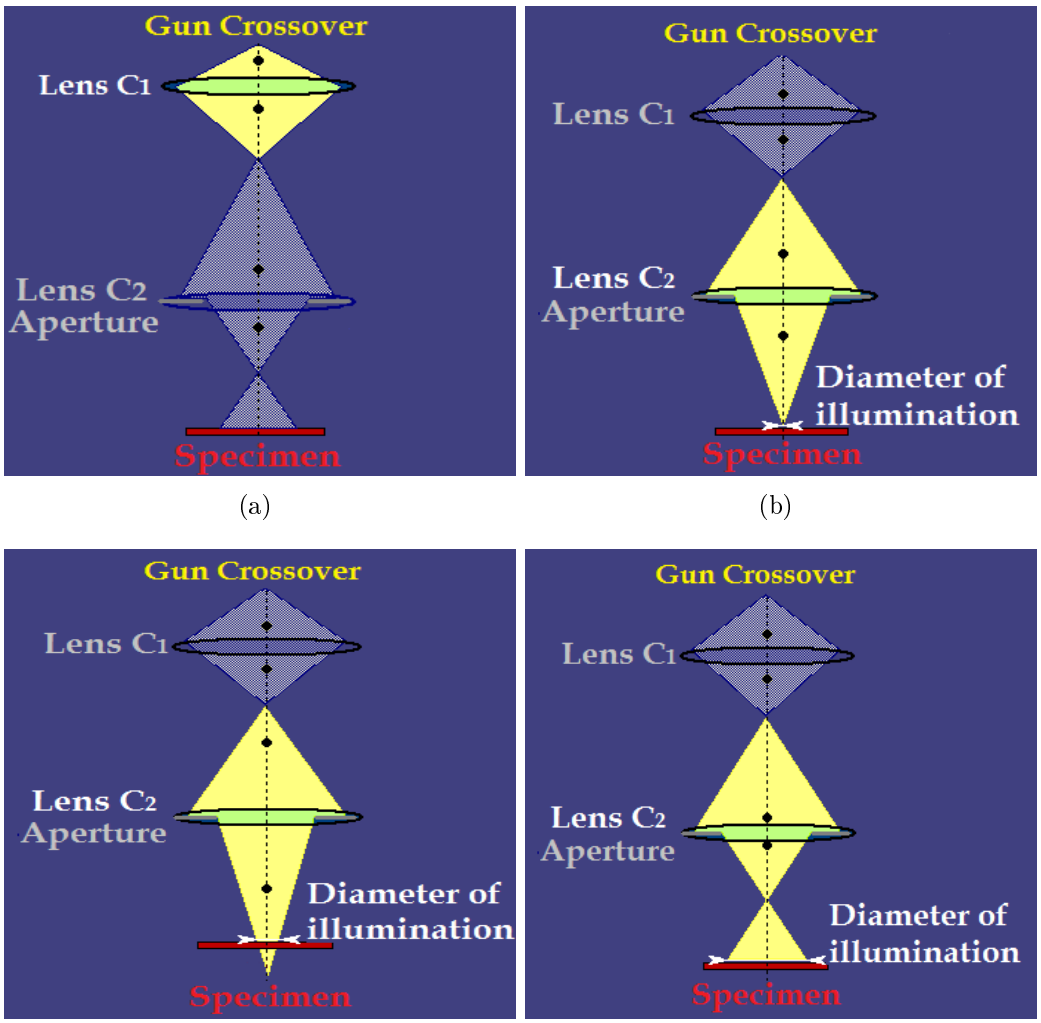

Figure 2.2 *a) Demagnification of gun cross over with C1. b) Focus mode of beam convergence with minimum diameter of illumination on specimen. c) Under-focus convergence increases the area of illumination. d) Over-focus mode with expanded diameter of illumination [11].*

2.3 Electron Specimen Interaction

The electric potential distribution within a specimen is not uniform; the specimen comprises of different atomic nuclei, each of which provides a Coulomb potential depending on the nature of that atom [12]. Irradiating the specimen, with a uniform density of electrons transmitted through condenser system, electrons will pass the specimen unscattered, elastically scattered or inelastically scattered. The probability of each of these events is measured with their scattering cross section. Each event is defined as below:

1. Most of the electrons pass through the specimen without any interactions, as there were no specimen. In an atomic view, the unscattered electron path is not close enough to any atom to experience the electric field of that atom, consequently no inclination in the electron path. More precisely, since the interior space of the specimen is represented by the electric potential distribution, unscattered electrons pass through the zones which the transverse electric field is weak [12].

2. The elastic scattering due to the potential of the nucleus is the most significant cause of contrast in electron microscopy image formation. Electrons that pass close to the atoms of the specimen will be deflected by the Coulomb potential of the nucleus. If the electron does not lose energy -energy loss is negligible- in this interaction, then the scattering is called elastic scattering. Figure 2.3 illustrates the scattering of an electron under the nucleus influence. Electrons travel in a hyperbolic path when they face the Coulomb force of the nucleus, depending on l -shortest distance between electron and nucleus. If l is too big, then the electron faces no force, and continues its straight trajectory. For a smaller l deflection angle θ increases [13, 14].

3. Inelastic scattering occurs when the incident electrons collide with the specimen electrons. In this case, the loss of energy is significant, while the deflection angle is small. Usually, the deflection angle of inelastically scattered electron is less than 5 degrees, which let these electrons to appear beside the unscattered electrons in image formation procedure. Those transmission electron microscopes advantaging from zero-loss mode can distinguish between unscattered electrons, and inelastic scattered electrons. Figure 2.4 compares a projection acquired without and with zero-loss mode.

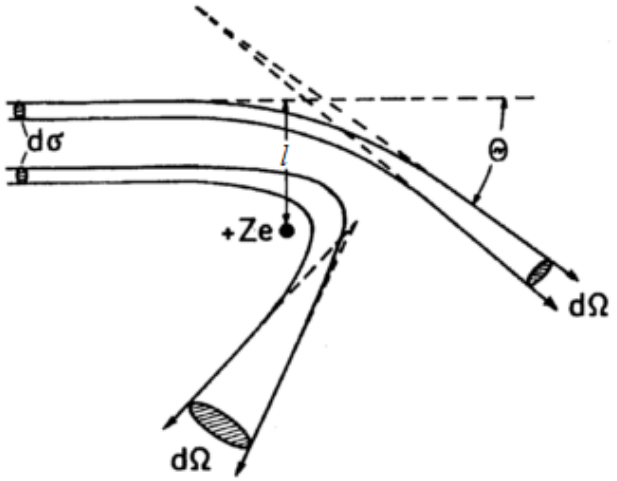

Figure 2.3 *Elastic electron scattering under nucleus effect and differential cross sections $d\sigma/d\Omega$ [13].*

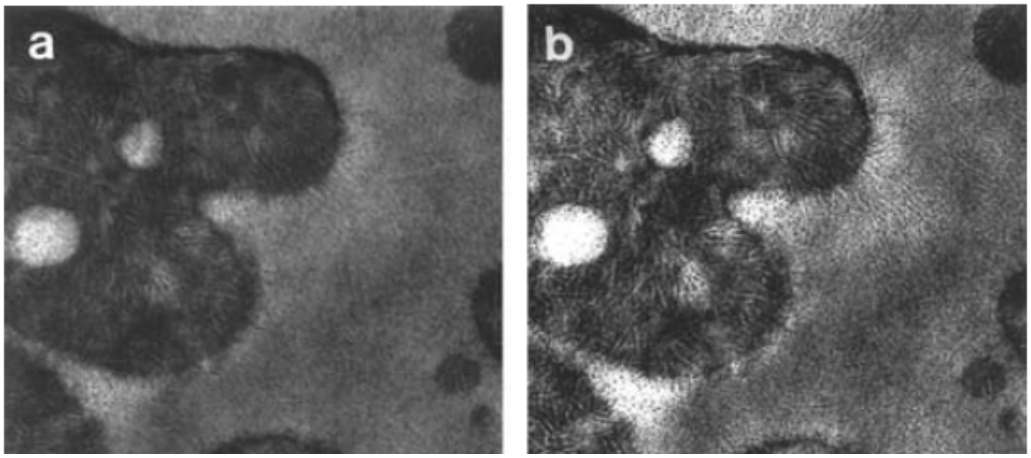

(a) (b)

Figure 2.4 *Projection acquired a) without zero-loss mode b) with zero-loss mode [15].*

Now, scattered electrons may emerge from the specimen, or undergo another scattering, i.e. either elastic, or inelastic. The probability of the second scattering increases by the increment of the specimen thickness [12, 13, 14].

In case the specimen does not generate acceptable electric potential distribution contrast, it can be stained with heavy atoms -lighter atoms selectively bound to heavier atoms. Vividly, for high resolution imaging, the specimen remains unstained,

since the detail structure of the specimen are supposed to be imaged.

2.4 Mean Free Path

Scattering cross section is the effective area which implies the intrinsic likelihood of scattering event. Total cross section σ_{el} is the sum of elastic scattering σ_{el} and inelastic scattering σ_{inel} . Thus, the scattering occurs in the small area of σ_t in the vicinity of each atom.

To count for the atoms existing in a thickness dz, mass-thickness dx is defined as $dx = \rho\, dz$, with the unit of gr/cm^2, where ρ is the density. Then, N is defined as N_A/A, where N_A is the Avogadro's number, and A is the atomic weight. Thus, we have:

$$Number\, of\, atoms\, in\, a\, thickness\, dz = N\rho\, dx. \tag{2.1}$$

Now, if the specimen with dz thickness and above-mentioned properties is irradiated with n electrons per unit area, number of scattered electrons dn would be computed as:

$$dn/n = -N\sigma_t\, dx. \tag{2.2}$$

The negative sign implies that n is decreased by scattering. Taking the integral from both sides of Eq. 2.2, we can write:

$$Ln(n) = -N\sigma_t\, x + Ln(n_0), \tag{2.3}$$

where n_0 is the number of electrons per unit area in $x = 0$. Solving Eq. 2.3 for n, we have:

$$n = n_0\, exp(-N\sigma_t\, x), \tag{2.4}$$

$$n = n_0\, exp(-x/x_t), \quad where \quad x_t = 1/N\sigma_t. \tag{2.5}$$

Equations 2.4 and 2.5 indicate that the number of unscattered electrons declines exponentially with the mass-thickness increment [13]. Considering Eq. 2.5 in a semi logarithmic scale the electron transmittance ($T(n) = n/n_0$) exhibits linear properties

as follows:

$$Ln(n/n_0) = exp(-x/x_t), \tag{2.6}$$

$$Ln(T(n)) = exp(-x/x_t). \tag{2.7}$$

In practice, in large mass-thickness values Eq. 2.7 does not remain linear due to the multiple elastic/inelastic scattering. The reason is behind the fact that, those electrons which scattered firstly with very high angles can be scattered back toward the incident direction and pass through the objective diaphragm, i.e. multiple scattering effect. Therefore by defining mean free path as the mean distance which a particle passes between two successive collisions, it can be assumed that, if the specimen thickness were smaller than the mean free path, the second collision does not occur, thus ignoring multiple scattering.

2.5 Objective Diaphragm

After interaction with the specimen, transmitted electrons i.e. both scattered and unscattered, are focused with an objective lens on a focal plane. Thus, electrons scattered with a same direction are focused there. An objective diaphragm is located at back focal plane and intercepts electrons which scattered with angles larger than θ_0. Typically, the size of diaphragm diameter (2r) is between 20-200 µm (see Fig. 2.5) [9]. The Smaller diaphragm size produces micrographs with higher scattering contrast and blocks multiple elastically scattered electrons. Almost, all the medium resolution micrographs are generated by stopping the highly scattered electrons. It should be noted that, highly scattered electrons inherent significantly important information which are vital for high resolution imaging. The size of objective diaphragm influences electron transmittance behavior -linearity of Eq. 2.7, thus the quantitative properties of image formation. Applying Eq. 2.7 despite the fact that the electron transmittance is deviating from the linearity in a tilt series, produces wrong information in 3D reconstruction. Two significant reasons for deviation from linearity in Eq. 2.7 are increment of specimen thickness and small objective diaphragm. Former reason increases multiple scattering, and the latter provides high electron interception by diminishing the size of objective diaphragm. In a study [16], using Carbon Microcoils (CMC), intensity attenuation is precisely measured relative to diaphragm aperture and specimen thickness. There it has been shown that increment of specimen thickness and small objective diaphragm increase the

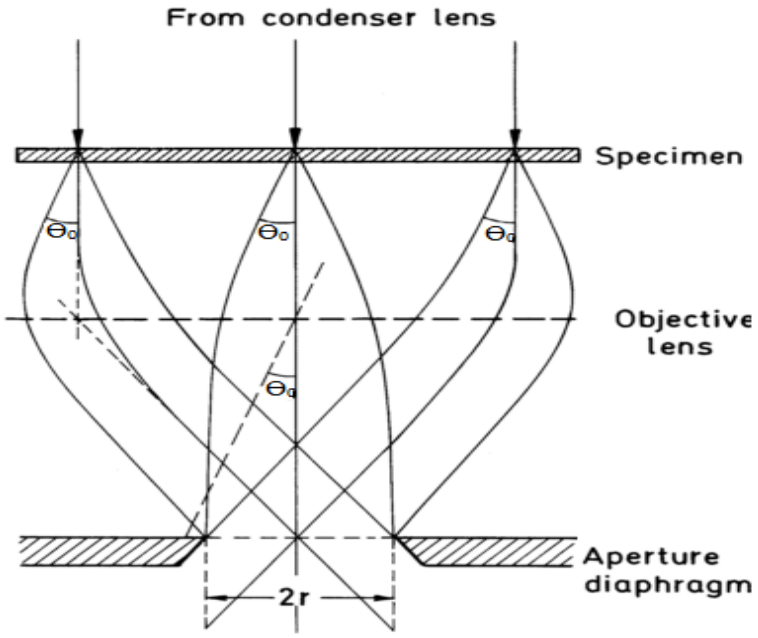

Figure 2.5 *Objective diaphragm located at back focal plane intercepts electrons sacttered with $\theta \geq \theta_0$ [9].*

artificial fluctuation in material density and inaccuracy in the shape of reconstructed specimen. Figure 2.6 depicts the effect of objective diaphragm size on reconstruction accuracy: Fig. 2.6a is the ground truth and from Fig. 2.6b to c the size of objective diaphragm decreased. Figure 2.6b shows that the object is reconstructed almost with relative uniform intensity when the objective aperture is sufficiently large but decreasing the radius of diaphragm increases inaccuracy of the reconstructed image; the edges are almost indistinguishable, streaking artifact is dominant and average intensity is low (see Fig. 2.6c).

2.6 Contrast Transfer Function

Letting the desired electrons pass through the objective diaphragm, the first intermediate image is formed by the objective lens; the image is typically provided by 50x magnification. Subsequently, the first intermediate image should be magnified by further lenses known as projective lenses. It is possible to model the projective system of a TEM in a function which acts on the electron wave. The function is called Contrast Transfer Function (CTF) and it is modulated to electron wave scattered from the specimen in frequency domain. Thus, the image formed on the detector

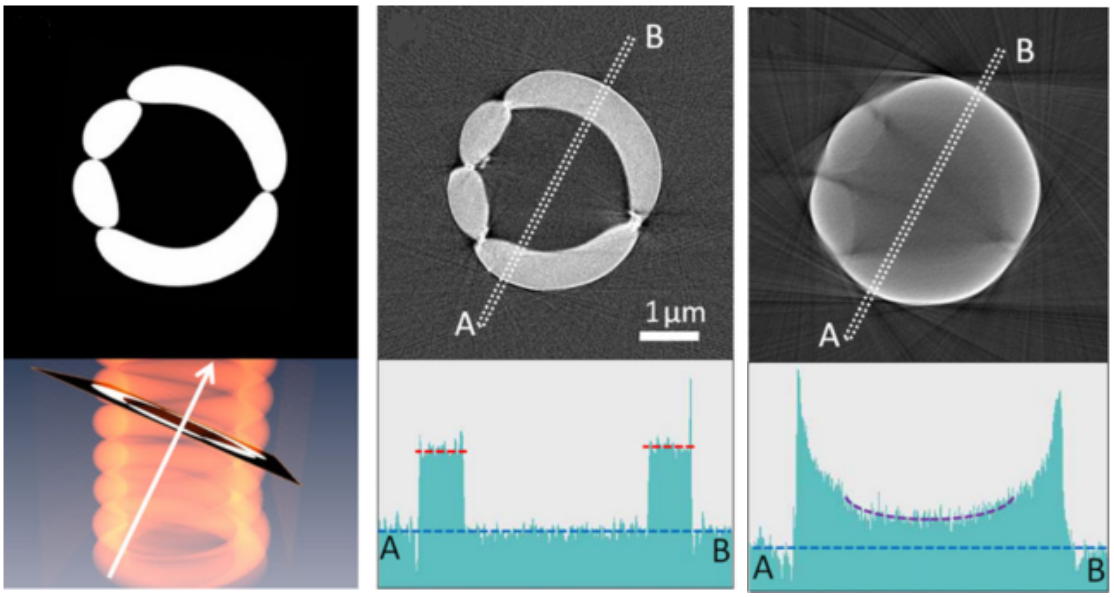

(a) (b) (c)

Figure 2.6 *Bright and dark regions belong to CMC and vacuum respectively. a) Ground truth. b-c) All the factors of image acquisition remain constant except for the objective aperture size which decreases from b to c. Intensity profiles from point A to B are shown in the bottom row [16].*

plane U_{det} , is a convolution of inverse Fourier of CTF and scattered electron wave U_{sc} in spatial domain [10].

$$U_{det} = F^{-1}\{CTF\} * U_{sc}. \tag{2.8}$$

CTF is a consequence of optical aberrations and defocus value (ΔF) -it is a function of spatial frequency. It affects the electron wave both in amplitude and phase. The amplitude of CTF is characterized by a decaying envelope indicating the amplitude decline in high spatial frequencies. This envelop directly depends on the defocus value [17, 18]. CTF also behaves in an oscillatory manner, in which the contrast reversals starts from a certain spatial frequency (see Fig. 2.7). The contrast reversals which come with the oscillatory behavior of CTF are harmful for the detected projections. For instance, suppose that in some frequency ranges a density appears black in a white background, whereas it will appear white over a black background in another frequency ranges due to the contrast reversals [19]. More precisely, in a certain frequency, CTF passes the zero point, so that no specimen information emerges in the image. In the frequency range to the next zero, the phase contrast

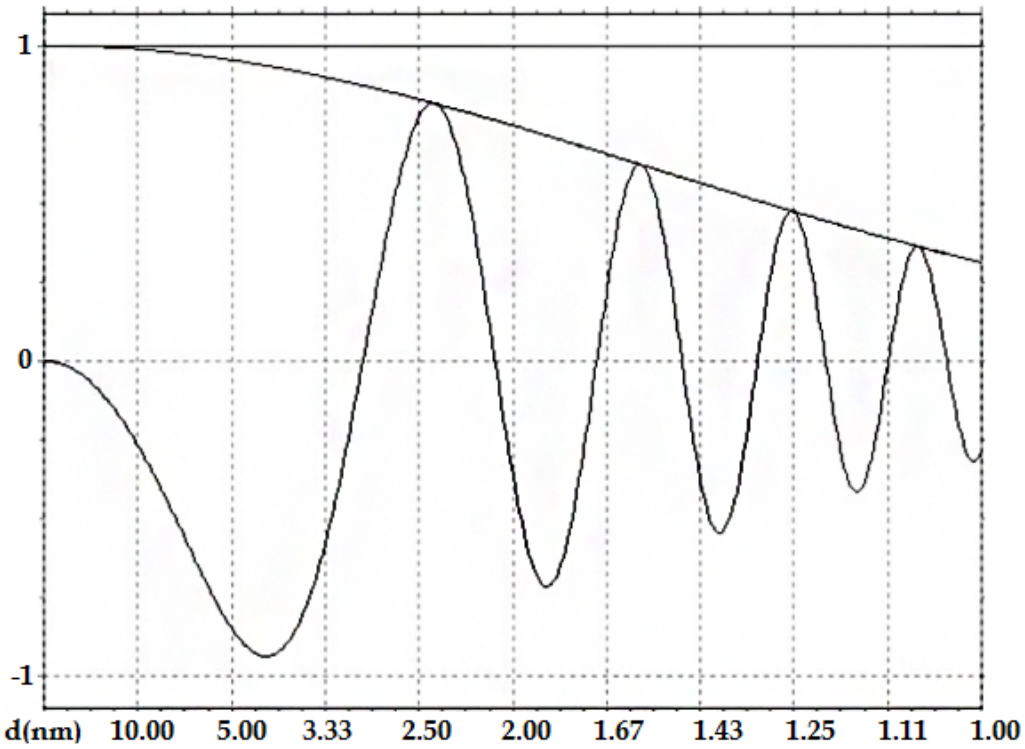

Figure 2.7 *Theoretical CTF of an EM at acceleration voltage of 200 kV. Defocus value is chosen such that zero crossing of CTF occurs at* $(2.8\,\mathrm{nm})^{-1}$ *[20].*

changes to the opposite of its previous one. It is very important to consider that the first zero-crossing of CTF defines whether the CTF correction is needed, so that if the expected resolution is beyond, then CTF correction is required to gain reliable information. For instance, as we can observe in Fig. 2.7, the first zero of CTF (where the contrast reversals start) occurs at $(2.8\,\mathrm{nm})^{-1}$ frequency, requiring CTF de-convolution for resolving details higher than this resolution [20]. It is mentioned already that defocus value controls the decline of CTF envelop thus the location of first zero. Increasing the defocus value displaces the location of first zero toward lower resolutions as it can be seen in Fig. 2.8 (zoom of each image in top row is shown in the bottom row) where different defocus values are examined at 300 KV acceleration voltage. Figure 2.8a is the original image with 0.5 nm pixel size and is supposed to be viewed with $\Delta F = 2$, 2.5 and 7.8 µm (see Fig. 2.8b-d). Details with higher resolutions are closer to the center of the image, so when ΔF is increasing the radius of unreliable information increases and moves toward lower resolutions or away from the image center. Difficulties in defining the CTF of low SNR images in cryo-tilt series is a force to choose the defocus value such that the first contrast

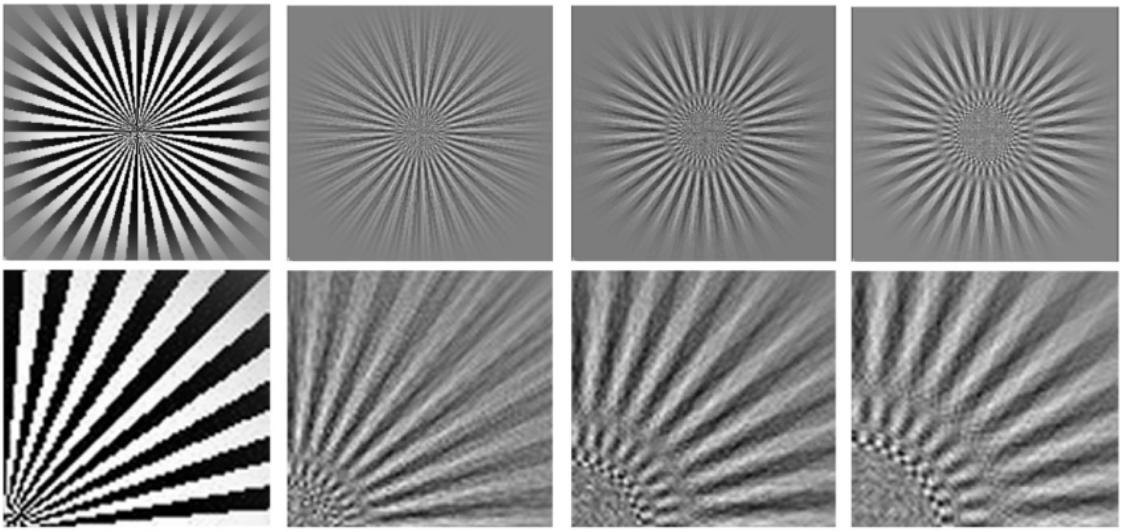

(a) (b) (c) (d)

Figure 2.8 *a) Original image which is viewed by electron microscope under 300 kV acceleration voltage and defocus of: b)* 2 µm *c)* 2.5 µm *and d)* 7.8 µm. *Bottom row is the zoomed view of top row for clearer display of the effect of CTF [19].*

reversal corresponds to the highest resolution obtained in image acquisition process. Generally, CTF correction is applied for high resolution imaging such as single particle reconstruction. Thus, practically in electron tomography CTF correction is not needed because of low resolution limits of this technique. In case CTF correction is required, it should be corrected for each single projection contributed to the reconstruction.

2.7 Bright Filed and Dark Field Imaging

2.7.1 Bright Filed (BF) Imaging

In bright filed imaging, the objective diaphragm is inserted, and absorbs all electrons scattered with $\theta \geq \theta_0$. Thus, regions where contain high mass-thickness coefficients will appear darker, in comparison with regions with low mass-thickness coefficients. Generally in BF-TEM, the background of the image appears brightly, as almost all electrons pass without scattering in regions without the specimen.

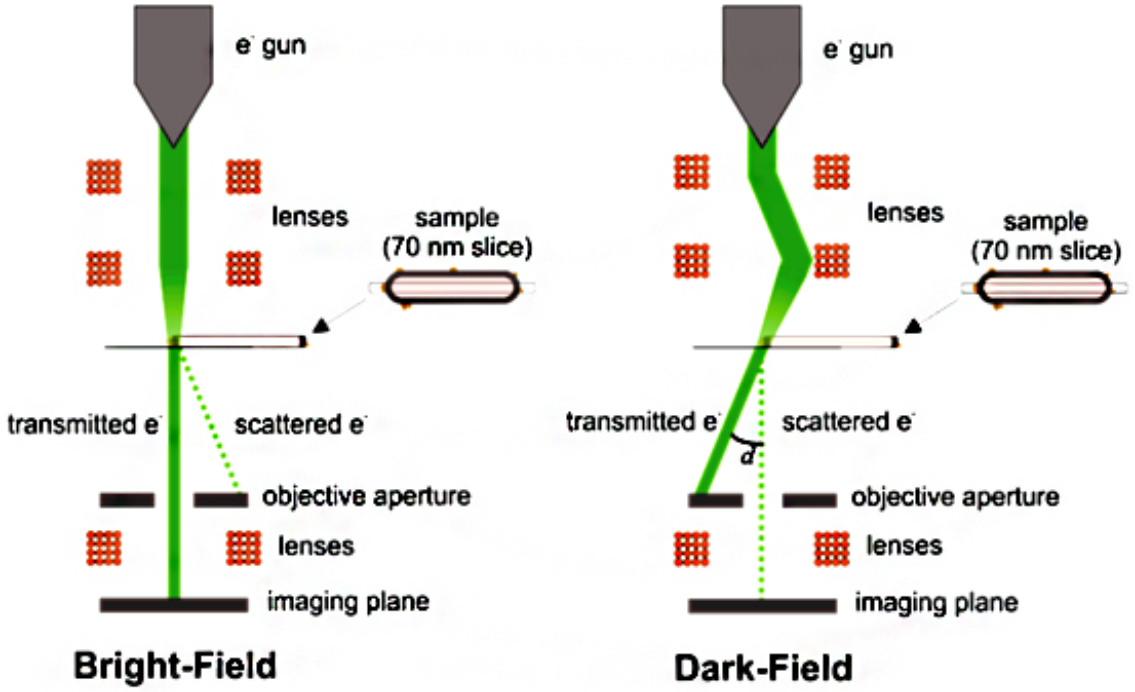

(a)

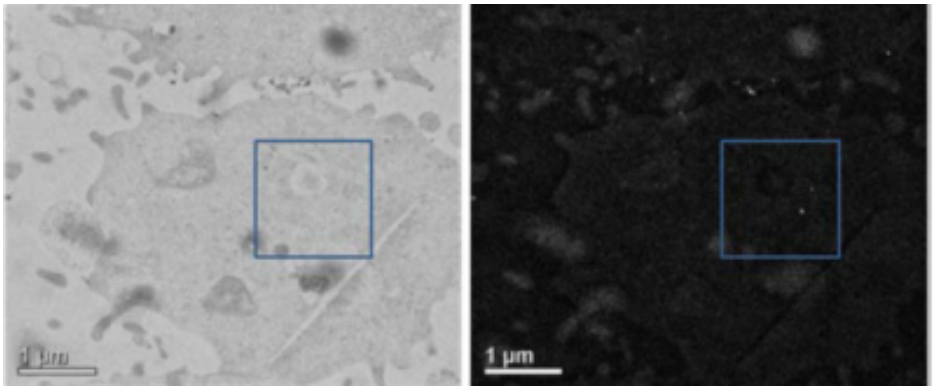

(b)

Figure 2.9 *a) Schematic of how BF and DF imaging function. b) Result of bright filed imaging (left) and dark field imaging (right) [21].*

2.7.2 Dark Filed (DF) Imaging

Dark field mode is available on typical TEM instruments. Opposite to the bright field imaging which the unscattered electrons contribute to image formation, in dark field imaging, scattered electrons participate in image formation. Considering Fig. 2.9a, in DF-TEM traditionally, the incident beam is radiated by a tilted angle like

"d" to the specimen. Transmitted electrons, i.e. unscattered electrons, pass the specimen without deflection, and would be absorbed by the objective diaphragm. On the other hand, those electrons deflected by the angle "d" continue down in parallel to the virtual microscope line. Thus, not being absorbed by the objective diaphragm, the scattered electrons create the scattering contrast in dark field imaging [21, 22]. Consequently, areas in the specimen with low mass-thickness coefficients are appeared brightly, while the background of the image is dark due to the blocking of unscattered electrons. Figure 2.9.b compares result of BF and DF imaging; in bright field imaging the background is bright and dense objects appear dark opposite to the dark filed imaging.

2.8 Scattering Contrast

To explain scattering contrast, electron movement is assumed to be particle wise. Elastic scattered electrons with deflection angles larger than objective diaphragm do not participate in image formation, thus remaining of the electrons -unscattered and inelastic scattered electrons- produce an image with scattering contrast. It means that, the scattering contrast is presented by the sum of intensities and not the summation of wave amplitudes as in purely wave-optical theory imaging. Almost all the medium resolution (2-3 nm) contrasts are created by this mechanism. Generally, scattering contrast is employed in amorphous specimens, surface replicas or biological segments. To enhance the scattering contrast in BF-TEM, inelastic scattered electrons -electrons with high loss of energy- can be filtered with energy filters [15].

2.9 Phase Contrast

In case of phase contrast, image intensity acquired by squaring the sum of the wave amplitudes. In another words, it is a superposition of the electron waves at the image plane, while they have interfering effect on each other [15]. Phase contrast is required for high resolution imaging. To understand this mechanism, the specimen is assumed to be made of large number of thin slices, each of which representing a 2D, multiplicative, complex transparency. When the incident electron wave propagates through the first slice, it will be modified and reaches the next following slice, thus will be modified again. The electron wave will be modified until it emerges from the specimen. The final modified electron wave can be represented by a multiplicative

specimen transparency function:

$$W(x,y) = |W(x,y)|exp\{i\varphi(x,y)\}, \tag{2.9}$$

where phase shift (φ) and the amplitude term |W| are projections of the potential and absorption of the specimen. The interaction will result in different phase shifts between the scattered and unscattered electrons [12]. In another words, phase shift in emerging wave is proportional to the line integral of electrostatic potential [10]. The resultant micrograph obtained from the convolution of electrostatic potential of the specimen and inverse Fourier transform of contrast transfer function. CTF is describing the imaging conditions and TEM properties.

2.10 Image Formation

2.10.1 Detector Plane

Detector plane is considered as a rectangular plane, divided into squared pixels [10]. The size of the detector plane determines the field of view (FOV), so that bigger detector plane permits for larger FOV. Considering detector plane, pixel size is a factor in defining the resolution. For a fixed magnification, the smaller pixel size leads to a higher resolution.

2.10.2 Detector Response

After interaction with the specimen, electrons reach the scintillator and result in an emission of photons. To discuss the detector response, firstly detector gain (C_{Gain}) and Detective Quantum Efficiency (C_{DQE}) are defined as:

C_{Gain} refers to the magnitude of amplification in a given system. Typically, the C_{Gain} is set so that the full well of the charge coupled diode (CCD) fulfills the complete range of digitalization in 1x gain. But, it can also be set according to the imaging situation. For instance, higher values of C_{Gain}, are appreciated in photon starved cases, which high-sensitivity mode is required. Alternatively, when higher SNRs are required, lower C_{Gain} would be selected.

C_{DQE} or shortly DQE indicates the quality of recording of electrons, and is defined as the ratio of squared output SNR and squared input SNR. Thus, it can be written

as:

$$DQE = (SNR)^2_{out}/(SNR)^2_{in}. \tag{2.10}$$

In an ideal detector, all the incident electrons are detected with the same weight, thus detective quantum efficiency is equal to one, while in practice DQE cannot gain the value of unity [23]. DQE is a function of frequency, and damps in higher frequencies, consequently it obtains minimum value at Nyquist frequency. Figure 2.10 shows the DQE in fractions of Nyquist frequency.

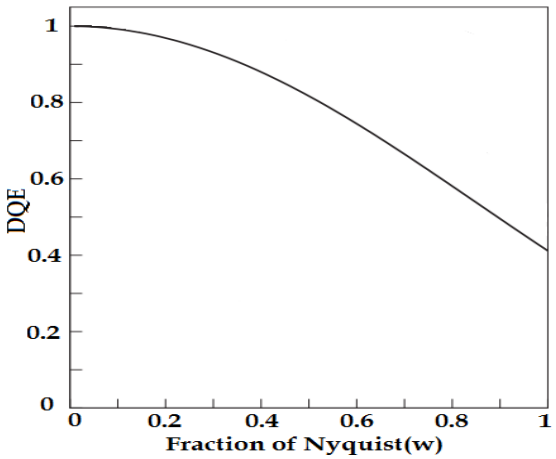

Figure 2.10 *DQE as a function of frequency (ω) is defined as fractions of Nyquist frequency) [23].*

2.10.3 Detector Blurring

Emitted photons from the scintillator will be detected on detector cells. Photons corresponding to an intensity point in scintillator are not hitting only one detector pixel, but also the nearby pixels. Thus, an intensity point in scintillator will be represented by a pixel and its neighborhood. Consequently, the intensities detected in the detector pixels are not independent, and there is a correlation between intensity of a pixel and its neighborhood. Also it should be added that, pixels with high intensity values may suffer charge bleeding. The leakage of a pixel charge to the adjacent pixels alters the point spread function (PSF) of the detector.

Modular transfer function (MTF) is the Fourier transform of PSF, and typically used

instead of PSF. The detector MTF is surveyed thoroughly by [24] and is defined by:

$$MTF(\xi) = \frac{a}{1+\gamma_1|\xi|^2} + \frac{b}{1+\gamma_2|\xi|^2} + c, \tag{2.11}$$

where ξ is the spatial frequency and a, b, c, γ_1 and γ_2 are variables to adjust the MTF. The first two terms model the head and tail parts of the PSF and c is a constant. Note that the tail of the PSF is due to the propagation of photons into the neighboring detector cells and it plays the main role in the blurring observed in the detectors. The variables in Eq. 2.11 are independent of the specimen and they are supposed to be fitted experimentally by measuring the Wiener spectrum of the detector.

2.10.4 Shot Noise

In electron microscopy, different sources of noise contaminate the measurement. The dominant source of noise in EM is shot noise; statistical fluctuation in the number of electrons counted by the detector. In the other words, the number of electrons detected in a time interval is random.

Shot noise follows Poisson distribution if following conditions observed:

- The distribution of the number of electrons depends only on the length of time interval, and not on the starting and ending instances of detection. Thus, the longer the interval, the higher the number of detected electrons.
- Arrival of electrons in each time interval is independent of any other interval, and has no effect on the number of electrons detected on other time intervals.
- In a small time interval, the probability of detecting two or more electrons is negligible in comparison to the probability of detecting one electron.

Holding the conditions, the probability of observing n electrons in the time interval t is:

$$P(n,t) = \frac{(\lambda t)^n e^{-\lambda t}}{n!} = \frac{\Gamma^n e^{-\Gamma}}{n!}, \tag{2.12}$$

where λ is the mean electron rate (electrons/second). Γ is the mean of number of electrons arrived to the detector in the interval t, and consequently, the standard

deviation is equal to $\Gamma^{1/2}$. In higher counts, Poisson distribution inclines to normal distribution.

Having mean and standard value, the SNR is calculated as:

$$SNR = \frac{\Gamma}{\Gamma^{1/2}} = \Gamma^{1/2} = (\lambda t)^{1/2}, \tag{2.13}$$

which indicates that higher irradiation time (higher dose) increases the SNR value [25].

3. LOW DOSE IMAGING IN CRYO ELECTRON TOMOGRAPHY

Cryo electron tomography is known as a bridge between light microscopy and molecular microscopy like X-ray diffraction or single particle analysis (SPA). Target specimens in cryo electron tomography are biological structures such as macromolecular complexes, small bacteria, pleomorphic viruses and slices or thin areas of cells [2]. Generally, a resolution of 5-10 nm is attainable in electron tomography reconstruction. However, still it is possible to push the attainable resolution a bit further to the range of 2-5 nm; optimizing image acquisition properties in addition to some image processing techniques to improve the resolution in electron tomography [2, 26]. From image acquisition perspective, acceleration voltage, sample thickness, magnification, defocus radiation, dose and tilt scheme are important to discuss. However, in terms of image processing, appropriate filtering of the noisy projections, contrast transfer function (CTF) correction and correct tilt series alignment are tools to enhance the maximum resolvable details of electron tomography. Our concern in this chapter is to optimize image acquisition features.

3.1 Acceleration Voltage

Acceleration voltage of an electron source plays a significant role in image formation, as it has a direct effect on mean free path. Figure 3.1 shows how total elastic and inelastic cross-sections decrease due to increase of acceleration voltage for two elements; carbon (C) as a light element and platinum (Pt) as a heavy element. Consequently, decrement in total σ_{el} and σ_{inel} enhances the mean free path as it is shown in Table 3.1. Therefore, the problem of imaging cells and organelles with complex shapes and large thicknesses can be overcome by high acceleration voltages in the range of 400-1000 kV, as the penetration power of electrons enhances with the increment of the acceleration voltage. Typically, for thin samples $\leq$ 100 nm, 100 kV electron microscope is sufficient, however for imaging thick samples, i.e. 250-500 nm,

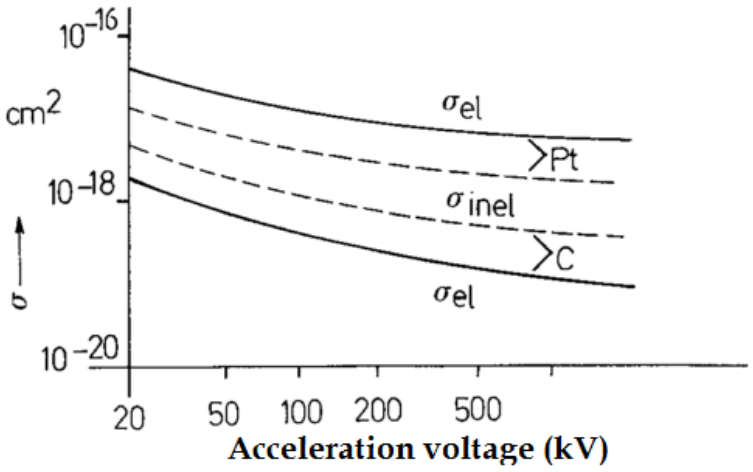

Figure 3.1 *Elastic and inelastic cross-sections as a function of acceleration voltage for carbon and platinum [12].*

intermediate (300-400 kV) or high voltage (1 MV) electron microscopes is required. It is important to consider that, possible gain in penetration power is limited [6]. Approximately, increasing the acceleration voltage from 100 kV to 300 kV enhances the penetration by the factor of two, while moving from 300 kV to 1.2 MV augments the penetration only by the factor of 1.5. Note that enlargement of mean free path enables us to irradiate the specimen with more electrons. For instance, at 300 kV, 1.75 times more electrons can be applied in comparison to 120 kV.

Table 3.1 *Elastic mean free path (nm) as a function of acceleration voltage (kV) for carbon and platinum [12].*

Acceleration voltage (kV)	Carbon	Platinum
17.3	45.9	0.03
25.2	65.5	3.78
41.5	102	5.41
62.1	145	6.57
81.8	181	7.83
102.2	216	8.95
150	321	10.9
300	518	14.7
750	632	23.6

Inspecting the acceleration voltage in terms of specimen damage, it should be considered that, either decreasing or increasing the acceleration voltage below or above certain levels increase the probability of specimen damage; below a certain acceleration voltage the probability of inelastic and multiple scatterings will enhance while above a certain acceleration voltage knock-on events[1] will increase. To have an acceptable trade-off between penetration power and specimen damage, 300-400 kV acceleration voltage is practical.

3.2 Magnification

Depending on the desired resolution, i.e. what kind of structures are supposed to be revealed, magnification is determined. Low magnification inherits larger field of view, less detail structure and higher SNR. Having magnification and detector cell size, we can define the pixel size in the specimen level as:

$$Magnification = \frac{Detector\ cell\ size}{Desired\ resolution}. \tag{3.1}$$

It should be taken into account that images from high magnifications suffer from small field of view and low SNR. Also, modulation transfer function (MTF) of detectors drops in high frequencies. Thus, in practice images are acquired by 4x greater magnification than that of desire, and then 4 pixels contribute to one binned pixel with higher SNR [2].

3.3 Defocus

As mentioned earlier, defocus value determines the location of the first zero-crossing of CTF. To overcome the effect of CTF, it is better to choose it corresponding to the maximum resolution required, i.e. the lower the defocus the higher the covered resolution. If the resolution is beyond first zero-crossing of CTF, then de-convolution of signal with an appropriate CTF as an image post-processing step is needed [20]. On the other hand, selecting high defocus values produce images with higher contrast which is advantageous in low dose electron tomography. Therefore, it is recommended to choose the highest defocus which covers the highest required frequency.

[1] An inelastic event, in which energy transferred to an atom is higher than its binding energy. [20]

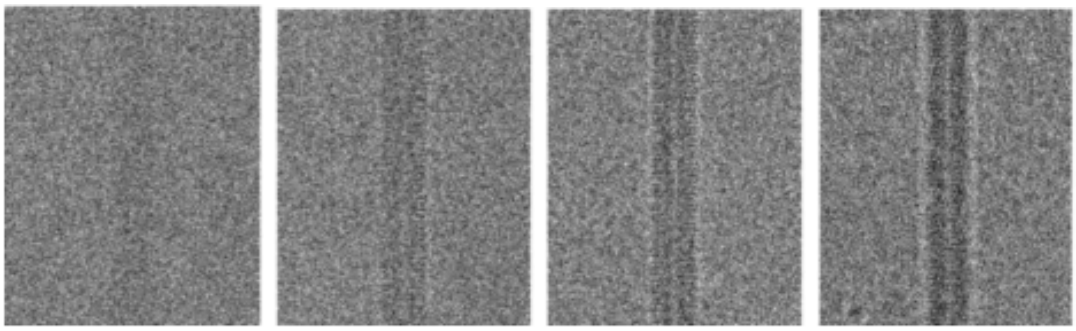

(a) (b) (c) (d)

Figure 3.2 *Imaging a portion of Tobacco Mosaic Virus (TMV), applying 66000× magnification, dose of 3000-3500 e-/nm^2 (180-210 e-/pixel), with different defocus values: a)* $\Delta F = 0\,\mu m$ *b)* $\Delta F = 1.5\,\mu m$ *c)* $\Delta F = 3\,\mu m$ *and d)* $\Delta F = 6\,\mu m$ *[10].*

Figure 3.2 shows the effect of increasing the defocus value from 0 to 6 µm that enhances the contrast of resultant projection. Note that blurriness and alteration in quantitative properties of the specimen are consequences of choosing high defocus values.

3.4 Dose and Electron Radiation Damage

Conventionally, electron dose is expressed as the number of electrons per squared nanometer (e-/nm^2). In cryo-ET, the main restrictive factor in acquiring a high resolution reconstruction is the total electron dose, since the native structure of the biological specimen should be preserved during the image acquisition. Vitrified specimen undergoes breakage of covalent bonds in high exposure of electron beams, leading to structural degradations. Figure 3.3 shows how high electron radiation forms bubbles and holes in the specimen by ionizing effect and thermal damage -energy absorbed by the specimen and converted to heat. Absorption of the energy by the specimen is defined by 1) the acceleration voltage: the higher the acceleration voltage the lower the scattering cross section and 2) the number of electrons irradiated to the specimen: the lower the dose the lower the probability of inelastic scattering events [27]. For imaging in high resolutions (at least 7 Å), total dose of 1 e-/Å^2 will not introduce harmful radiation damages to the specimen [29]. However, such a low radiation dose makes electron tomography impossible as a result of very poor contrast and SNR. Practically, high resolution 3D reconstruction is possible only through single particle analysis (SPA) by extracting different projections from

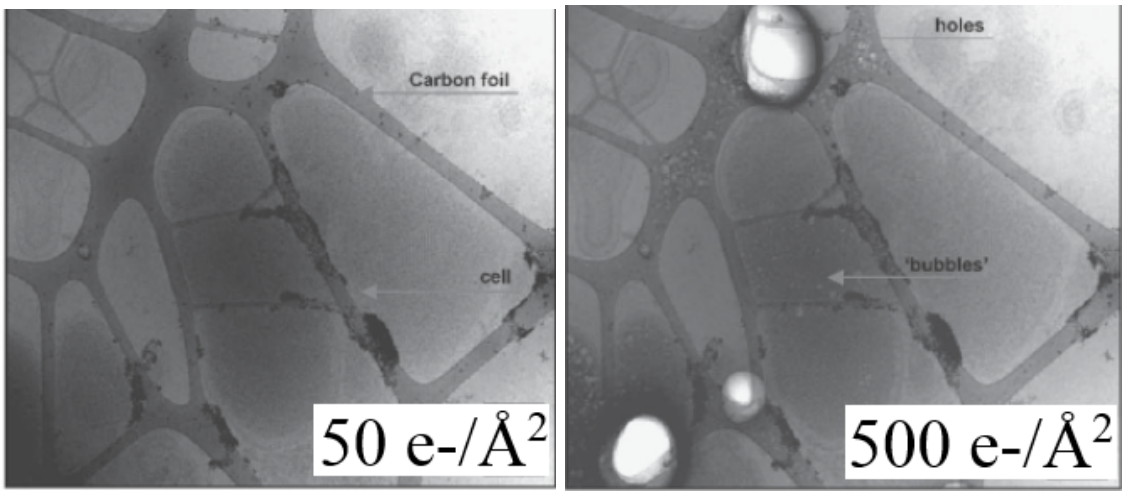

(a) (b)

***Figure** 3.3 Electron radiation damage leads to structural degradations such as forming holes and bubbles in ice embedded prokaryotic cell: a) 50e-/Å² b)500e-/Å² [28].*

different repeats of a molecule, when the macromolecular specimen takes the advantage of multiple occurrence. Most of biological specimens like cell components are imaged with low resolutions (50-100 Å) since identical structures in the copies are rare.

Allowable dose for imaging of a biological specimen is highly restricted and differs specimen to specimen. As a general statement, for an unstained biological specimen, approximately 5000 e-/nm^2 is tolerable not to undergo specimen damage. More importantly, the total amount of tolerable dose should be divided by the number of projection views [20]. Therefore, to distribute the allowable number of electrons on an image series efficiently, number of tilt images and exposure time should be computed optimally to keep the radiation as low as possible, while maximizing the SNR in acquired projections.

3.5 Angular Sampling

The approach to angular data acquisition influences resolution of reconstruction. In noise free imaging of a spherical sample, i.e. thickness of the sample is independent of tilt angle, the resolution of the reconstruction depends on diameter of the sample (D) and constant angular tilt increment (α_0) [30]. So, the resolution is determined

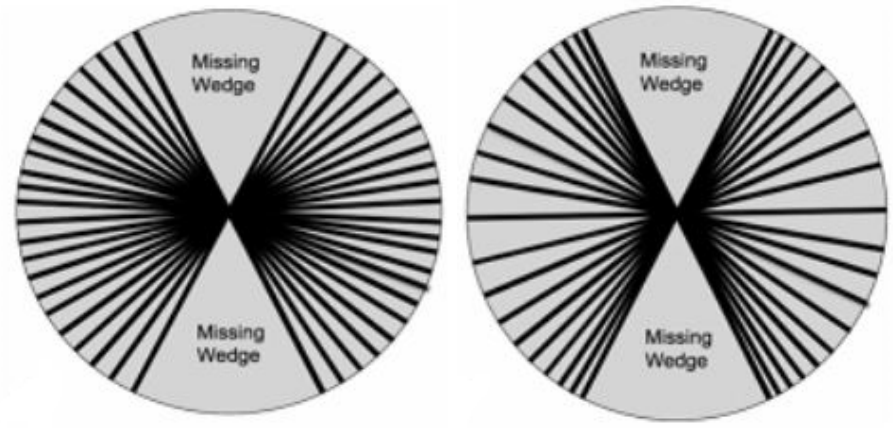

(a) (b)

Figure 3.4 *Schematic representation of angular data acquisition. Due to mechanical constraints, fully angular collection of the data is not possible, causing unsampled parts called missing wedge. a) Angular sampling applying constant tilt increment. b) Angular sampling applying Saxton method, leading to more optimal data collection [27].*

by:

$$Resolution = D\,\alpha_0. \tag{3.2}$$

In practical ET, acquired images are noise contaminated, samples have slab geometry and tilt range is limited approximately to -70° to 70° due to mechanical constraints. Violating the conditions of isotropic resolution, reconstruction suffers anisotropic resolution and Eq. 3.2 is not applicable for estimating the resolution [2]. Assuming that noise contamination and angular constraints are not modifiable, we are able to reduce the effect of slab geometry of specimen. Saxton scheme [5] is a popular approach to compensate for the increasing effective thickness in high angles. In his method, angular spacing is proportional to the cosine of tilt angle (α), so as the specimen inclines more toward high angles the sampling frequency increases. The original formula [5] is suitable for the crystalline specimen, however it has been modified and approximated as [6]:

$$\alpha_{n+1} = \alpha_n + arcsin(sin\alpha_0\, cos\alpha_n). \tag{3.3}$$

Comparing the number of tilts acquired by the constant angular increment with Saxton's scheme in Eq. 3.4) and Eq. 3.5, for a certain tilt range and α_0, Saxton's

method produces more acquisition angles. This makes the method optimal, when the electron dose is highly restricted [6].

$$Number\,of\,tilt\,angles\, = \frac{2\alpha_{max}}{\alpha_0} + 1. \tag{3.4}$$

$$Number\,of\,tilt\,angles\, \approx (\frac{2\alpha_{max}}{\alpha_0} + 1)\frac{1}{\alpha_{max}} Ln\frac{1 + sin\alpha_{max}}{1 - sin\alpha_{max}}. \tag{3.5}$$

A representation of constant and Saxton methods of angular distribution is illustrated in Fig. 3.4 [27]. The figure shows both incompleteness in fully data collection called missing wedge and the differences in density of sampling as a function of tilt angle.

3.6 Exposure Time

Ideally, tomographic image series should have similar SNR. Considering the slab geometry of the specimen in ET, by increasing the tilt angle, the effective thickness of the specimen increases with $1/\cos\alpha$. Consequently, if the exposure time for all tilt series stays constant, the SNR of high angles is insufficiently low, while the SNR of low angles is unnecessarily high leading to waste of electron dose. To compensate for the thickness increment, the exposure time (t) can obtain one of the following exponential or cosine formulas:

$$t = t_0 exp[T(\frac{1}{cos\alpha - 1})] \qquad 'Exponential\,mode', \tag{3.6}$$

$$t = \frac{t_0}{cos\alpha} \qquad 'Cosine\,mode', \tag{3.7}$$

where t_0 is the exposure time of zero tilt angle, and $T = D/\Lambda$ where, D is sample thickness at zero tilt angle, and Λ is the effective mean free path. In practice, achieving a constant SNR throughout the tilted series is not possible, as the specimen thickness is not perfectly constant over the field of view [6].

There are restriction factors influencing the exposure time in addition to the desired formulation in Eq. 3.6 and Eq. 3.7. For instance, maximum time which the conditions of the sample can be preserved for imaging or minimum time that a CCD camera needs to record the projections. Moreover, the brightness of electron gun should be enough to produce sufficient number of electrons in small periods of exposure time; with low number of electrons, the signal recorded in the detector suffers

significantly from low SNR and is not able to provide minimum count rate required for recording alignment markers [6].

In low dose electron tomography that the user is supposed to distribute highly restricted number of electrons over total number of tilt series, progress in computer-automated data collection has been of a crucial importance. Tracking, focusing, recording the images and dose distribution are done automatically. Despite all the progress in automated data acquisition, mechanical and optical imperfections should be treated after data collection [2].

4. TOMOGRAPHIC IMAGE RECONSTRUCTION

Tomography refers to non-invasive imaging using penetrative waves to reconstruct the interior structures of an object from its projections. Computerized Tomography (CT), Positron Emission Tomography (PET) and Electron Tomography (ET) are different examples of this technique. In this section, definitions, formulas and methods concerning 2D reconstruction will be introduced. Although the main objective of tomography in this thesis regards to 3D reconstruction, to understand the theory in a simpler manner we take 2D case for explanation, then it can be expanded to 3D case.

4.1 Projection Vector - Radon Transform

A projection vector $P_\phi(s)$ of a continuous two dimensional function *f(x,y)* is a collection of lines of integral passing through the object function f at a certain angle ϕ. The lines of integral integrate the values of f along their ways (see Fig. 4.1). For instance, in the case of electron tomography, each line sums the electric potential of the specimen faces in its path. In order to understand the projection vectors, firstly it is needed to define a line of integral [32]. The Lines of integral are defined by their angle ϕ with respect to Y-axis and distance from the origin of the coordinate system s. They can be written as:

$$P_\phi(s) = \int_{(s,\phi)line} f(x,y)dl \quad where, \quad s = x\,cos(\phi) + y\,sin(\phi). \tag{4.1}$$

Now, for a certain angle gathering all lines of integral spread between $-\infty$ and $+\infty$ generates a projection vector or Radon Transform ($\mathcal{R}\{f(x,y)\}$) of the object at that angle as below:

$$P(s,\phi) \equiv \mathcal{R}\{f(x,y)\} = \int_{-\infty}^{+\infty}\int_{-\infty}^{+\infty} f(x,y)\delta(xcos(\phi) + ysin(\phi) - s)dxdy, \tag{4.2}$$

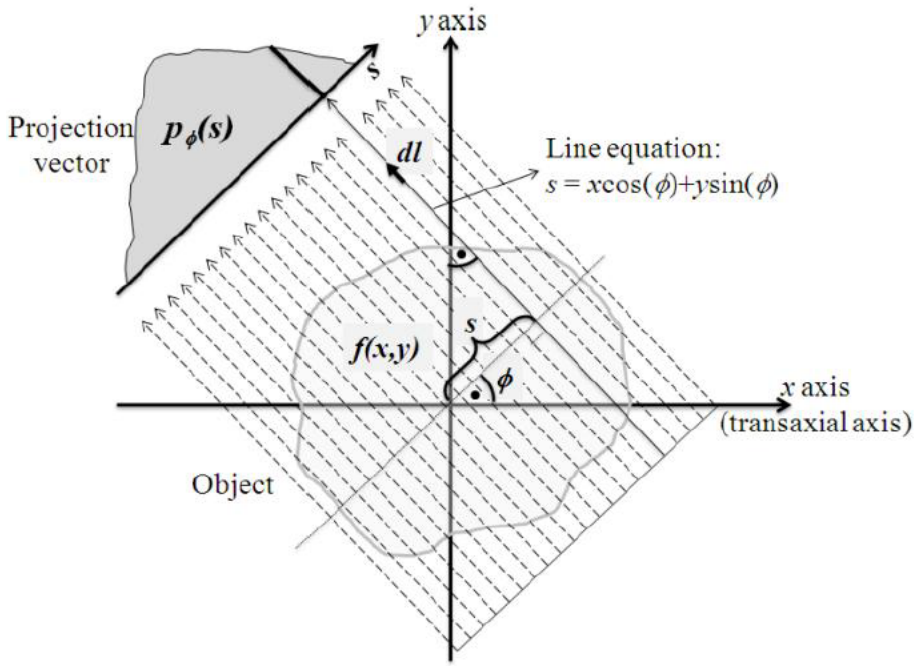

Figure 4.1 *Simple illustration of projections passing through the object f(x,y) at angle ϕ, forming projection vector $P_\phi(s)$ from the distribution of absorbing mass [31].*

where δ is the Dirac delta function. The radon transform maps the spatial domain to the projection or sinogram domain. A sinogram is the collection of the projection vectors over the angular view in which $\phi \in [0, \pi)$ and $s \in (-\infty, +\infty)$, thus a point in object function forms a sinusoidal curve. Figure 4.2a shows an object comprising of three bright circles, and its corresponding sinogram plotted based on s and ϕ in Fig. 4.2b. Each pixel in the sinogram corresponds to a line of integral at a certain angle. The sinograms are the basis of image reconstruction from projections. By defining sampling with the lines of integrals as *Radial* sampling, for an ideal reconstruction, continuous *Angular* and *Radial* samplings are needed. In reality continuous sampling is not practical, thus finite sampling substitutes the ideal infinite sampling and converts Eq. 4.2 to a discrete representation as:

$$P(s,\phi) = \sum_{0}^{M-1} \sum_{0}^{N-1} f(x,y)\delta(xcos(\phi) + ysin(\phi) - s), \tag{4.3}$$

where x, y, s and ϕ are discrete values and δ is the discrete impulse function [31].

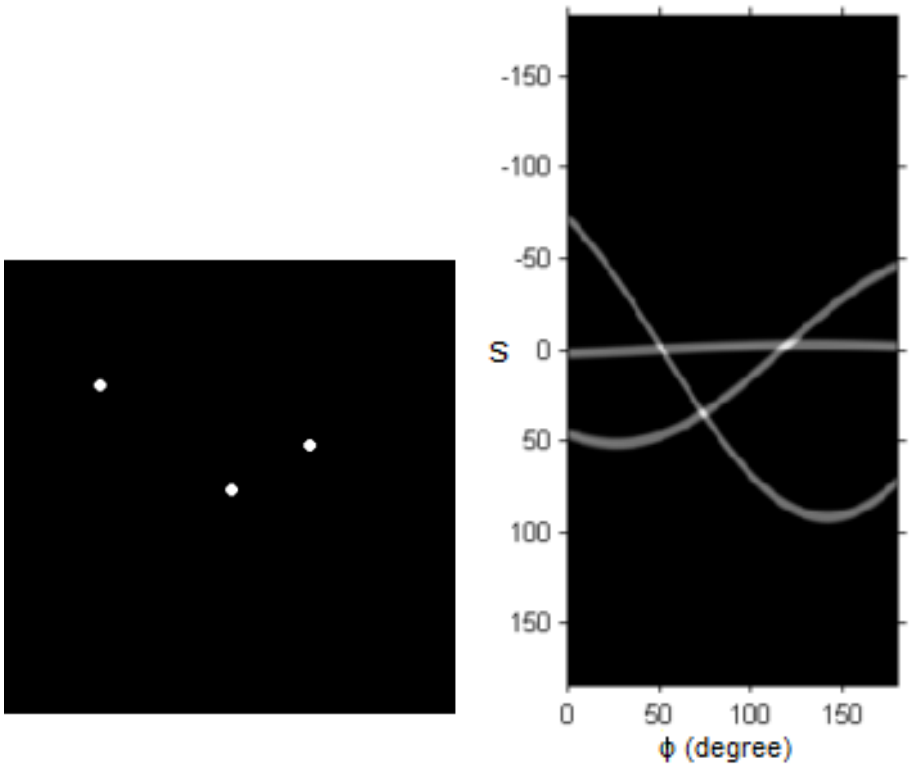

(a) (b)

Figure 4.2 *a) Object comprises of three bright circles. b) Corresponding sinogram of (a) plotted on s and ϕ coordinates [31].*

4.2 Fourier Slice Theorem

Considering parallel beam approximation, this theorem states that 2D Fourier transform of an object function corresponds to 1D Fourier transform of its projection vectors. In the other words, the 1D FT of each projection vector from a given angle corresponds to a slice that passes the origin of the 2D FT of the object at the angle where the projection vector is acquired. Thus, multiple projection vectors can be combined to obtain a discrete sampling of the whole 2D object function. Figure 4.3 illustrates the Fourier slice theorem at a certain angle ϕ. Mathematically, 1D FT of $P_\phi(s)$ can be written as:

$$P_\phi(\omega) = \int_{-\infty}^{+\infty} P_\phi(s) e^{-i2\pi ws} ds. \tag{4.4}$$

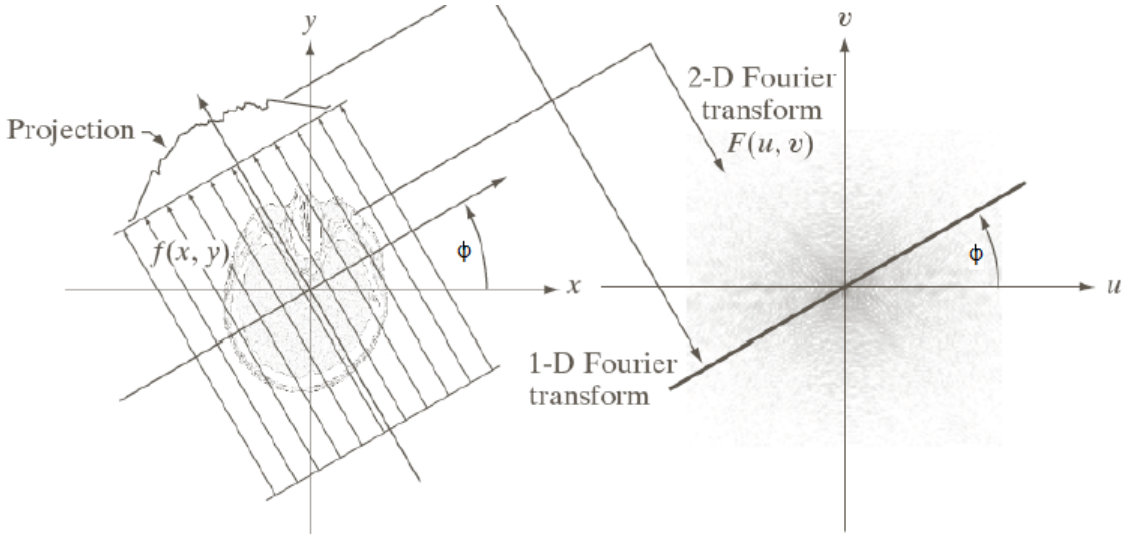

Figure 4.3 *Illustration of Fourier slice theorem; 1D FT is equal to one slice of 2D FT [33].*

In addition, *F(u,v)* representing the 2D Fourier transform of *f(x,y)* can be written as:

$$F(u,v) = \int_{-\infty}^{+\infty} \int_{-\infty}^{+\infty} f(x,y) e^{-i2\pi(ux+vy)} dxdy. \tag{4.5}$$

Now if *F(u,v)* is shown with a polar representation, considering $u = w\,cos(\phi)$ and $v = w\,sin(\phi)$, then Eq. 4.5 can be rewritten as:

$$[F(u,v)]_{u=wcos\phi, v=wsin\phi} = F(wcos\phi, wsin\phi) = P_\phi(w). \tag{4.6}$$

According to the Fourier slice theorem, having the projection vectors, discrete 2D FT of the object can be approximated. Therefore, computing 2D inverse FT will reconstruct the original object from its projection vectors [33].

4.3 Reconstruction Techniques

Considering projection vectors of an object from different angles, a reconstruction technique maps these projections to a 3D tomographic representation of the object. Technically, reconstruction of an object F from its projections is an inverse problem; solving a linear equation of the form $P = \varpi F + \varepsilon$ for F, while P is the projections, ϖ is the known system model and ε represents the noise added to the

ideal measurement. In electron microscopy noise almost follows Poisson distribution. For solving an inverse problem and reaching to a unique answer, according to Hadamard, conditions of the problem should be well-posed. It means that:

- The problem must have a solution (Existence).
- The problem must have at most one solution (Uniqueness).
- The solution must depend continuously on input data (Stability).

However, inverse problems concerning image reconstruction are generally ill-posed, i.e. they are not well-posed, and therefore only an approximation of the real answer can be obtained. Existence of non-unique answers for solving problem of reconstruction leads to many different approaches try to optimize the results [34]. Generally, different reconstruction algorithms can be divided into two main categories:

1. Analytical Image reconstruction algorithms: appropriate modification of data (sinogram) before back projection, i.e. filter before backprojection such that the reconstructed images are not blurred. Direct Fourier reconstruction (DFR) and filtered back projection (FBP) are two examples of this category.
2. Iterative algorithms: appropriate modification of data (reconstruction) after backprojection, i.e. iteratively correct the blurring of reconstructed image with the filtering algorithms. Iterative reconstruction algorithms are divided into algebraic and statistical reconstruction methods [35].

4.3.1 Direct Fourier Reconstruction (DFR)

Based on the Fourier slice theorem, taking 1D FT of each projection vector enables us to construct the 2D Fourier space of the object. By computing the inverse FT of the 2D Fourier space, an estimation of the object will be reconstructed. In this algorithm, the quality of the reconstruction depends on how accurate the discrete 2D FT of the object has been approximated. If sufficient number of projections is acquired a better reconstruction will be obtained. Nevertheless sampling the Fourier space needs consideration: for fast algorithms of 2D discrete Fourier transform (DFT), polar/radial sampling should be converted to the Cartesian/equidistance rectangular grid [36]. Figure 4.4 illustrates the interpolation from polar -shown with black

circles as available data- to Cartesian grid -shown with white circles as interpolated data. Moreover, sampling of the Fourier space is dense in the neighborhood of the origin and rather spars in high frequency regions. In this condition, to compensate for incomplete and/or non-uniform sampling in the spatial frequency domain, interpolation of the frequency space is employed. Sparsity of the samples in the high frequency regions declines the accuracy of the interpolation, which generally leads to introduction of artifacts in the reconstruction [36].

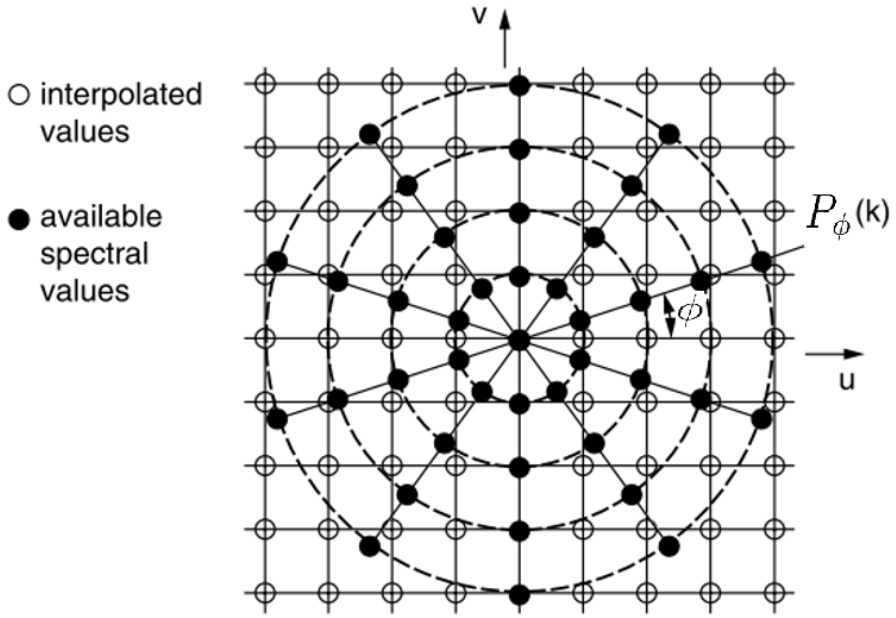

***Figure** 4.4 Interpolation from polar to Cartesian grid; available data are shown with black circles and white circles represent interpolated data [36].*

4.3.2 Filtered Back Projection (FBP)

Filtered back projection has been extensively used in the image reconstruction and known as golden standard in this field. To define the FBP, firstly back projection is defined as smearing each projection vector back to the image along the direction of its projection angle [37]. Intuitively, it is the backward operation of the projection procedure. So, if each 1D projection vector got replicated along the direction of its projection angle, sum of them would result in the back projection. Mathematically the back projection at angle ϕ can be stated as:

$$f_\phi(x, y) = P(xcos(\phi) + ysin(\phi), \phi). \tag{4.7}$$

Integrating for all projection angles from [0 π) leads us to reconstruct an image as below:

$$f_{back\,projected}(x,y) = \int_0^{\pi} f_{\phi}(x,y)d\phi. \tag{4.8}$$

And for a discrete sinogram, integral converts to finite sum of discrete back projections, where Eq. 4.8 can be written as:

$$f_{back\,projected}(x,y) = \sum_{\phi=0}^{\pi} f_{\phi}(x,y) = \sum_{\phi=0}^{\pi}(xcos(\phi) + ysin(\phi), \phi). \tag{4.9}$$

Results of the back projection is heavily blurred, this is due to oversampling of the low frequencies in Fourier domain. Reconstructed image can be formulated as:

$$\hat{f}(x,y) = f(x,y) * \frac{1}{\sqrt{(x^2+y^2)}}, \tag{4.10}$$

where $\hat{f}(x,y)$ is the reconstructed image, $f(x,y)$ is the real object map and the term $1/\sqrt{(x^2+y^2)}$ is the point spread function (PSF). Equation 4.10 shows that reconstructed image always comes with a convolution by the PSF [35]. In Fourier space the PSF appears as $1/\omega$ multiplied to *F(U,V)*. Therefore if the projection images are multiplied with $|\omega|$ in the Fourier space the effect of the PSF would be reduced. Convolution/Multiplication of the projection vectors in spatial/frequency domain with a kernel is called Filtered Back Projection. A straightforward method to construct a filter with the form of $|\omega|$ is Ram-Lak filter. Applying Ram-Lak filter emphasizes on the high frequencies more than low frequencies. This filter sharpens the edges in the reconstructed image and amplifies the noise as well. Increasing the noise applying Ram-Lak filter lays the ground for employing other filters such as Hamming and Hann filters. These two filters generate smoother reconstructions compared to Ram-Lak filter, however they keep the noise in an acceptable level. Figure 4.5 depicts the diversity of the filter response as a function of frequency which can be applied for the FBP. In case the imaging process is noiseless, with no attenuation, complete and continuously sampled and contains a uniform spatial resolution, FBP can reconstruct an object almost perfectly [37, 38, 39], however this conditions are too ideal for the real experiments. Since we are not able to model the noise and include a-priori knowledge by the FBP, reconstruction problems are usually handled with iterative techniques to produce better images.

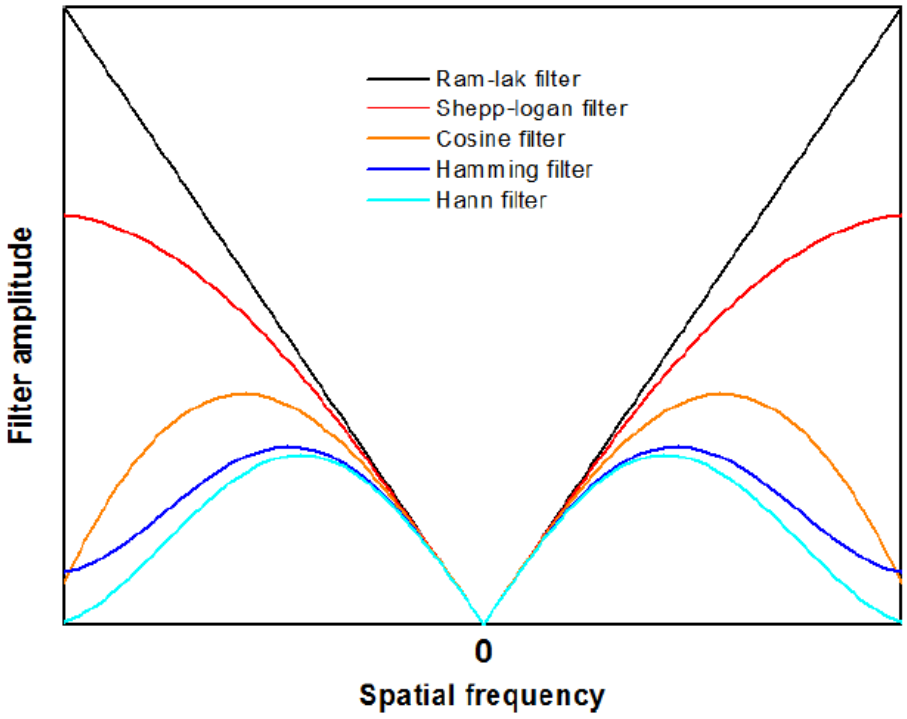

Figure 4.5 *Frequency response of different filters applicable for FBP [38].*

4.3.3 Algebraic Reconstruction Methods (ARM)

These methods are deterministic reconstruction approaches. They consider an inverse problem as a large-scale system of linear equations as:

$$\begin{bmatrix} \varpi_1 \\ \vdots \\ \varpi_N \end{bmatrix} F = \begin{bmatrix} P_1 \\ \vdots \\ P_N \end{bmatrix} \rightarrow \varpi F = P, \tag{4.11}$$

where ϖ is the system matrix, F is the unknown electric potential distribution and P is the projection matrix. In Eq. 4.11 all the elements including the object F are discrete values. A system matrix is defined as measuring the intersection path length of one specific line of integral within one specific object pixel. In another words, $\varpi_{i,j}$ is the weight of the contribution of the pixel i to the measurement j which is the length of the intersection between the pixel and the projected line. Figure 4.6 illustrates the concept of a system matrix considering that the side of each square/pixel is equal to unity [40]. As the size of measurement matrix P depends on the size of angular and radial sampling of projections, and the size of F

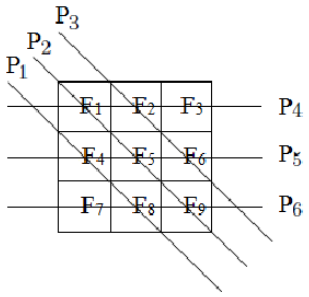

$$\begin{bmatrix} 0 & \sqrt{2} & 0 & 0 & 0 & \sqrt{2} & 0 & 0 & 0 \\ \sqrt{2} & 0 & 0 & 0 & \sqrt{2} & 0 & 0 & 0 & \sqrt{2} \\ 0 & 0 & 0 & \sqrt{2} & 0 & 0 & 0 & \sqrt{2} & 0 \\ 1 & 0 & 0 & 1 & 0 & 0 & 1 & 0 & 0 \\ 0 & 1 & 0 & 0 & 1 & 0 & 0 & 1 & 0 \\ 0 & 0 & 1 & 0 & 0 & 1 & 0 & 0 & 1 \end{bmatrix} \begin{bmatrix} F_1 \\ F_2 \\ F_3 \\ F_4 \\ F_5 \\ F_6 \\ F_7 \\ F_8 \\ F_9 \end{bmatrix} = \begin{bmatrix} P_1 \\ P_2 \\ P_3 \\ P_4 \\ P_5 \\ P_6 \end{bmatrix}$$

Figure 4.6 *F1-9 are pixel values and P1-6 are projection values [40].*

depends on the size of reconstructed image, system matrix ϖ will be a huge matrix. Computing the direct inverse of ϖ is not possible [39]. Therefore, to solve the problem, i.e. to solve the reconstruction problem, first an estimate of the unknown matrix F is taken. Then, iteratively the unknown function F is updated in a way that the error between the measured projections and calculated projections declines ($arg\,min_F \| P - WF \|^2$) or mathematically it can be written as:

$$F^{(k+1)} = F^{(k)} + \beta \frac{P_{i_k} - \varpi_{i_k}.F^{(k)}}{\varpi_{i_k}.\varpi_{i_k}} \varpi_{i_k}. \tag{4.12}$$

Equation 4.12 shows that an update estimate of the function ($F^{(k+1)}$) is calculated by back projecting the difference of forward projection of current estimation ($\varpi_{i_k}.F^{(k)}$) and deterministic projection matrix (P), then adding this difference to the current estimation ($F^{(k)}$) with a factor of β.

In severely ill posed conditions, ARM converges to a noisy reconstruction, as the method updates F row by row, i.e. a single projection value is used to update the F at a time. Therefore, different modifications of ARM such as Simultaneously

Iterative Reconstruction Technique (SIRT) and Simultaneously Algebraic Reconstruction Technique (SART) are introduced to improve the performance of ARM; SIRT updates F only when all projection views are processed and SART updates each pixel in F until all rows in one projection view are processed once [39, 41].

4.3.4 Statistical Reconstruction Methods

These methods solve the inverse problem statistically, assuming the unknown F_i is a random variable which follows a specific probability distribution function (PDF). In electron microscopy, as the shot noise is the main source of the noise, the PDF of the measurements and the noise is modeled with Poisson statistics. Generally speaking about statistical methods, estimation of the unknown random variable F should maximize the probability of occurrence of the measured data. Maximum Likelihood Expectation Maximization (ML-EM) is an iterative approach searches for the closest guess for the unknown variable F [42, 43, 44, 45, 46]. Like algebraic methods, firstly an approximation $F^{(0)}$ is used to start the iteration and then each iteration pushes the $F^{(0)}$ to minimize the distance between its forward projection and measured data as shown below:

$$F_j^{(k+1)} = F_j^{(k)} \frac{1}{\sum_i \varpi_{ij}} \sum_i [\varpi_{ij} \frac{P_i}{\sum_i \varpi_{ij} F_j^{(k)}}]. \tag{4.13}$$

As shown in Eq. 4.13, the difference between the forward projection of $F^{(0)}$ and the measured data P is calculated. Result is back projected and multiplied to the initial guess $F^{(0)}$ to obtain a new estimation for $F^{(k)}$ as $F^{(k+1)}$. Disadvantage of applying ML-EM is the convergence of this method to noisy images as the noise tends to increase heavily in each iteration. Figure 4.7 depicts the likelihood and the reconstruction error as a function of iteration number in ML-EM [47]. It shows that increasing the number of iteration enhances the likelihood monotonically, nevertheless it does not lead to a monotonic decline of the reconstruction error: from a certain point the reconstruction error starts to increase due to the noise contamination of the projections. Defining a stopping criterion for ceasing the iterations in early states provides a compromise between the noise level and quantitative accuracy. However, there exist deviations of the ML-EM such as median root prior method (MRP) where the dependency to the stopping criterion is reduced compared to the ML-EM. In image reconstruction, general tendency is to have smooth images with sharp edges [48]. In formulating ML-EM, prior knowledge is not taken into

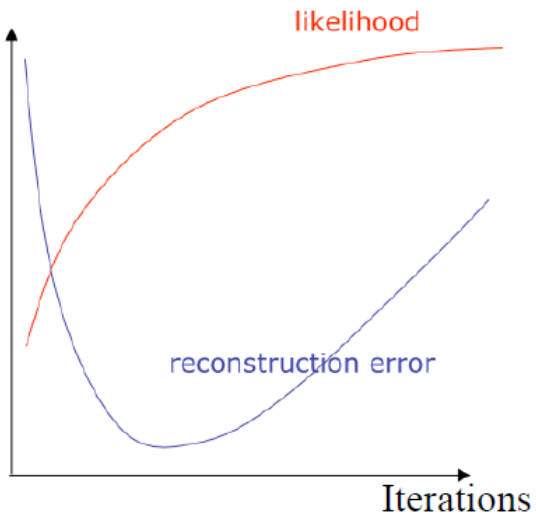

Figure 4.7 *Likelihood and reconstruction error as a function of number of iteration [47].*

consideration and only the likelihood is supposed to be maximized. By employing the prior knowledge in the ML-EM formulation, we can manipulate the reconstruction the way we desire. Below in Eq. 4.14, it is shown that how a a-priori knowledge enters the ML-EM formulation:

$$F_j^{(k+1)} = F_j^{(k)} \frac{1}{\sum_i \varpi_{ij} + \beta \dfrac{\partial M(F)}{\partial F_j}} \sum_i [\varpi_{ij} \frac{P_i}{\sum_i \varpi_{ij} F_j^{(k)}}]. \tag{4.14}$$

New term added to the ML-EM represents the a-prior knowledge. For instance, if smoothness in the reconstruction is desired, an averaging term can be added to Eq. 4.14. The influence of the a-prior knowledge can be controlled by β coefficient [47]. In such an approach, for updating a current guess, before multiplication of the error to the current state of the reconstruction, i.e. $F^{(k)}$, the error is regularized with the average of $F^{(k)}$. Figure 4.8 is a diagram of penalized reconstruction, where if we eliminate the penalization term, MLEM remains.

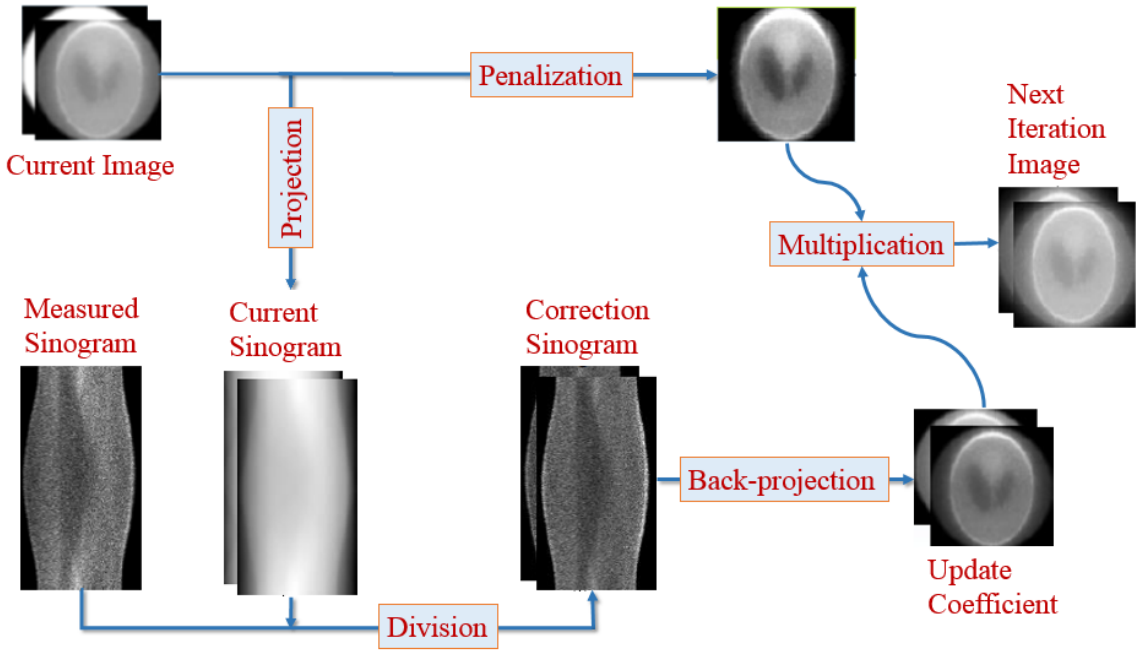

Figure 4.8 *Scheme of the ML-EM with a penalization factor [47].*

5. RESOLUTION MEASUREMENT APPROACHES

3D electron microscopy aims to depict the structure of wide range of specimens by means of different reconstruction algorithms. However, to find an optimal data acquisition approach and reconstruction algorithm, reconstructed tomograms can be compared objectively. For instance, measuring the resolution of a tomogram can tunnel to the robustness of its acquisition approaches. In this chapter, several methods for resolution assessment such as Fourier Shell correlation (FSC), Noise-Compensated Leave-One-Out (NLOO) and determination of effective resolution in incoherent ET are compared.

5.1 Resolution Measurement Approaches

Resolution of a light microscope is defined as the smallest distance between two points on a specimen which are still recognizable as two separate entities. Figure 5.1 illustrates that when two airy discs[1] merge into each other and pass the Rayleigh criterion[2] they become unresolvable. Microscope resolution is linked and limited to optical system properties and more importantly to the physical properties of particles used for imaging, e.g. in light microscopy it depends on the wave length of light source. The theoretical limit of resolution is calculated as:

$$Resolution \propto Wave\,length\,of\,light\,source. \tag{5.1}$$

Considering Eq. 5.1, electron wave is 100,000 times shorter than visible light which enables us to resolve much smaller structures with electron microscopy [51].

Having the definition of optical resolution in hand, since no external standard is

[1] A region with bright circular center surrounded by less intense rings [49].
[2] A criterion for the minimum resolvable detail [50].

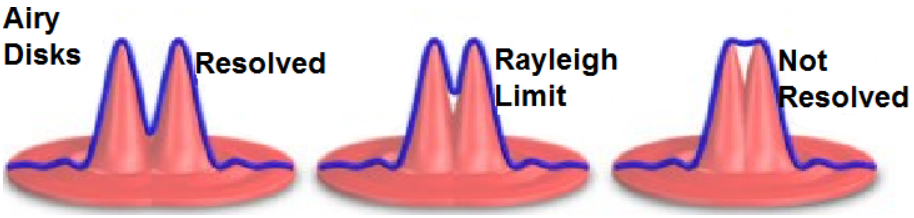

Figure 5.1 *Airy disk seperation and the Rayleigh criterion [51].*

existing for resolution evaluation in electron tomography, traditional concept of resolution is not applicable. Instead, internal consistency of the reconstruction results is defined as the resolution in electron tomography [51]. Thus, resolution in ET tries to estimate the level of details that is definitely and reliably presented in the reconstructed tomogram [19]. Some Factors affecting the resolution in ET are listed as below:

- Electron dose which directly affects SNR
- Acceleration voltage which defines electron wave length, for instance
  - Vacc = 100 kV, Relativistic wavelength is 3.70 pm
  - Vacc = 300 kV, Relativistic wavelength is 1.97 pm
  - Vacc = 1000 kV, Relativistic wavelength is 0.87 pm
- Missing wedge
- Optical system properties
- Specimen thickness
- Defocus value
- Alignment accuracy

To define the level of internal consistency in a reconstruction, Fourier shell correlation (FSC) is employed. But, unlike the single particle analysis (SPA) in which thousands of tomograms contribute to reconstruction, in electron tomography, this method is not applicable directly as the tomogram is unique. Among different approaches proposed to assess the resolution in ET, those introduced by Cardone *et al.* [52] have received considerable attention [19]. Based on cross validation, the paper

introduces two criteria; one is $FSC_{e/o}$ based on Fourier shell correlation and the other is Noise-Compensated Leave-One-Out (NLOO). These two methods calculate the average resolution in the reconstructed tomograms while for us an independent measure of resolution along Z-direction (direction of electron radiation) is required as well. Heidari *et al.* [53] proposed a method based on PSF measurement to find the effective resolution in X, Y and Z directions independently. Here we define X, Y and Z axes as the horizontal axis of the projection images, the tilt axis, and the direction of the electron beam respectively.

5.1.1 Fourier Ring/Shell Correlation

Fourier Ring Correlation in 2D [54] and Fourier Shell correlation in 3D [55] compare two Fourier transforms. The comparison implies how much the transforms are correlated with each other; correlation curve starts at a value close to one at low frequencies implying perfect correlation and declines to zero by increasing frequency [56].

Fourier Ring Correlation (FRC) between two transforms G and H is given by:

$$FRC_{GH}(k) = \frac{\Sigma_{u,v\in R(k)} Re\{G_{u,v}H^*_{u,v}\}}{\{(\Sigma_{u,v\in R(k)}|G_{u,v}|^2)(\Sigma_{u,v\in R(k)}|H_{u,v}|^2)\}^{1/2}}, \tag{5.2}$$

where u and v are components of Fourier transform and k is the radial frequency. *R(k)* indicates an annular zone in Fourier space with mean radius of k and asterisk denotes the complex conjugate. Fourier Shell Correlation (FSC) is similar to FRC except for *R(k)* which is a shell and the transform obtains three indices *(u,v,p)* [52].

Notably, resolution is constrained by noise as well as by resolving power, and it can be expressed by SNR as:

$$FSC(k) = \frac{SNR(k)}{SNR(k)+1}. \tag{5.3}$$

5.1.2 Even/Odd Fourier Shell Correlation

In Single Particle Analysis (SPA), numerous projections are existing. They are divided randomly into two sets and from each half-set a tomogram is reconstructed.

Applying FSC, resultant tomograms are compared in terms of consistency to measure the resolution. In ET, number of projections is significantly low and FSC underestimates the resolution when compared with full data set. In the studies, where a high resolution tomogram is already existing -by SPA- it can be used as a reference for computing FSC_{ref} correlation coefficients (in this thesis, as we have the ground truth, FSC_{ref} is applicable).

As standard FSC approach cannot be applied directly in ET, Cardone's model proposes dividing the tilt projections in even and odd numbers [52]. This is the most natural approach to generate two independent subsets for reconstruction, since Fourier space is covered uniformly and projection angles are spaced equally [52]. From each subset a tomogram is reconstructed independently, so FSC can estimate the resolution by measuring the correlation between Fourier transform of the tomograms. As already discussed, maximum spatial resolution in which the tomograms are mutually consistent is considered as the resolution of the tomograms [19]. However, dividing the tilt series into even and odd subsets doubles the angular step size between projections, thus according to Eq. 3.2 the resolution will be underestimated by the factor of 0.5. Theoretically, $\text{FSC}_{e/o}$ underestimates the resolution by the factor of 0.5 while in practice noise plays more severe role in constraining the resolution. To gain more realistic resolution considering noise, $\text{FSC}_{e/o}$ is redefined as:

$$FSC_{e/o}(k) = \frac{2FSC^*(k)}{FSC^*(k)+1}, \tag{5.4}$$

where FSC^* is the FSC between the two reconstructed tomograms. It is very important to consider that, since odd tilt projections are involved in generating one tomogram and evens are involved in reconstructing the other one, adjacent tilt projections are not contributing in generating the same tomogram. Therefore, if the degree of overlap between adjacent tilt projections is low, then underestimation of resolution will increase. So, when the diameter of a structure is large or when the angular step size is big, the independency between tomograms will enhance and thus the resolution underestimation [52].

5.1.3 Noise-Compensated Leave-One-Out (NLOO)

Another method proposed by Cardone *et al.* is NLOO [52]. In this approach, for each tilt projection a tomogram is reconstructed from full tilt series excluding the

projection under evaluation. Then the tomogram is re-projected in the direction of missing projection. Leaving out one projection in the reconstruction causes the resolution of the tomogram to be very close to that of the complete tomogram. Synthetic projection and missing projection are compared in terms of FRC to provide the effect of missing projection on the resolution [19]. This method is computationally expensive, however it allows to draw the resolution against tilt angle to assess the dependency of the resolution to the direction of projections. Such an evaluation is helpful when we aim to reduce the effect of missing wedge on the reconstruction. Figure 5.2 plots the dependency of the resolution as a function of tilt angle; generally increasing the tilt angle declines the resolution. Also, the plot can be considered as an indicator of the specimen damage; moving toward high angles (in this case high positive angles) inconsistency increases, thus the resolution decreases [52].

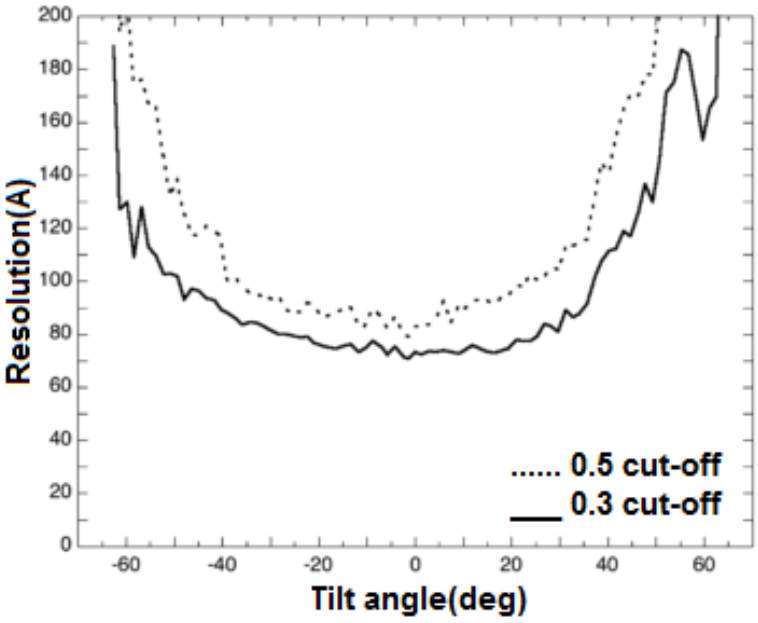

Figure 5.2 *NLOO-2D of a cryo-tomogram plots the resolution as a function of tilt angle. Resolution is measured based on two cut-off thresholds: 0.3 and 0.5 [52].*

Above-mentioned description is similar to leave-one-out cross validation method. Since projections and re-projections contain different noise statistics, noise should be compensated: noise in re-projections is lower than projections proportional to the number of projections. To estimate the noise, differences between a projection and its corresponding re-projection from a tomogram which is generated by all input projections are computed. Now, the discrepancy between a projection and its

corresponding re-projection from a tomogram created without that projection can be written as:

$$NLOO - 2D(k) = \frac{FRC_{G\tilde{G}^-}(k)}{FRC_{G\tilde{G}}(k)}, \tag{5.5}$$

where G is a projection, $\tilde{G}$ is the corresponding re-projection to G from a complete tomogram and $\tilde{G}^-$ is the corresponding re-projection to G from a tomogram without G. In addition, $FRC_{G\tilde{G}^-}(k)$ and $FRC_{G\tilde{G}}(k)$ are defined according to Eq. 5.2. The denominator is the noise compensation term. Equation 5.5 is proved in the appendix of [52], where it has been shown how Normalized Squared Difference between tomograms is stated with their FRC to ease the representation of NLOO. NLOO-2D provides a resolution for each slice, and by performing further summation it is possible to extend it to a 3D representation for N_p input projections as below:

$$NLOO - 3D(k) = \frac{\frac{\Sigma_i^{N_p}\Sigma_{u,v\in R(k)} Re\{G_{u,v}^{(i)}\tilde{G}_{u,v}^{-(i)^*}\}}{\sqrt{\Sigma_i^{N_p}\Sigma_{u,v\in R(k)}|G_{u,v}^{(i)}|^2}\sqrt{\Sigma_i^{N_p}\Sigma_{u,v\in R(k)}|\tilde{G}_{u,v}^{-(i)}|^2}}}{\frac{\Sigma_i^{N_p}\Sigma_{u,v\in R(k)} Re\{G_{u,v}^{(i)}\tilde{G}_{u,v}^{(i)^*}\}}{\sqrt{\Sigma_i^{N_p}\Sigma_{u,v\in R(k)}|G_{u,v}^{(i)}|^2}\sqrt{\Sigma_i^{N_p}\Sigma_{u,v\in R(k)}|\tilde{G}_{u,v}^{(i)}|^2}}}. \tag{5.6}$$

Theoretically, we expect that NLOO estimates the resolution more realistically compared to $\text{FSC}_{e/o}$. The reason is that number of images contributing to the computation of NLOO is higher than $\text{FSC}_{e/o}$. To depict this conclusion, resolution measurement approaches applying FSC_{ref}, $\text{FSC}_{e/o}$ and NLOO are compared in Fig. 5.3a to c. To do so, resolution of a reconstructed tomogram with angular steps of 1°, 2° and 4° is assessed with the mentioned methods. If we consider FSC_{ref} as the most accurate estimation of the resolution, results show that NLOO approximates the resolution closer to FSC_{ref} compared to $\text{FSC}_{e/o}$. Increasing the step size, i.e. decreasing the number of projections, intensifies the resolution underestimation in $\text{FSC}_{e/o}$ more than NLOO (see Fig. 5.3c). Furthermore, considering only one resolution measurement approach, for instance FSC_{ref}, the results demonstrate that decreasing the number of projections reduces the resolution. Considering FSC_{ref}, 0.5 correlation criteria occurs at 0.07, 0.06 and 0.05 1/Å when the step size is 1°, 2° and 4° respectively [52].

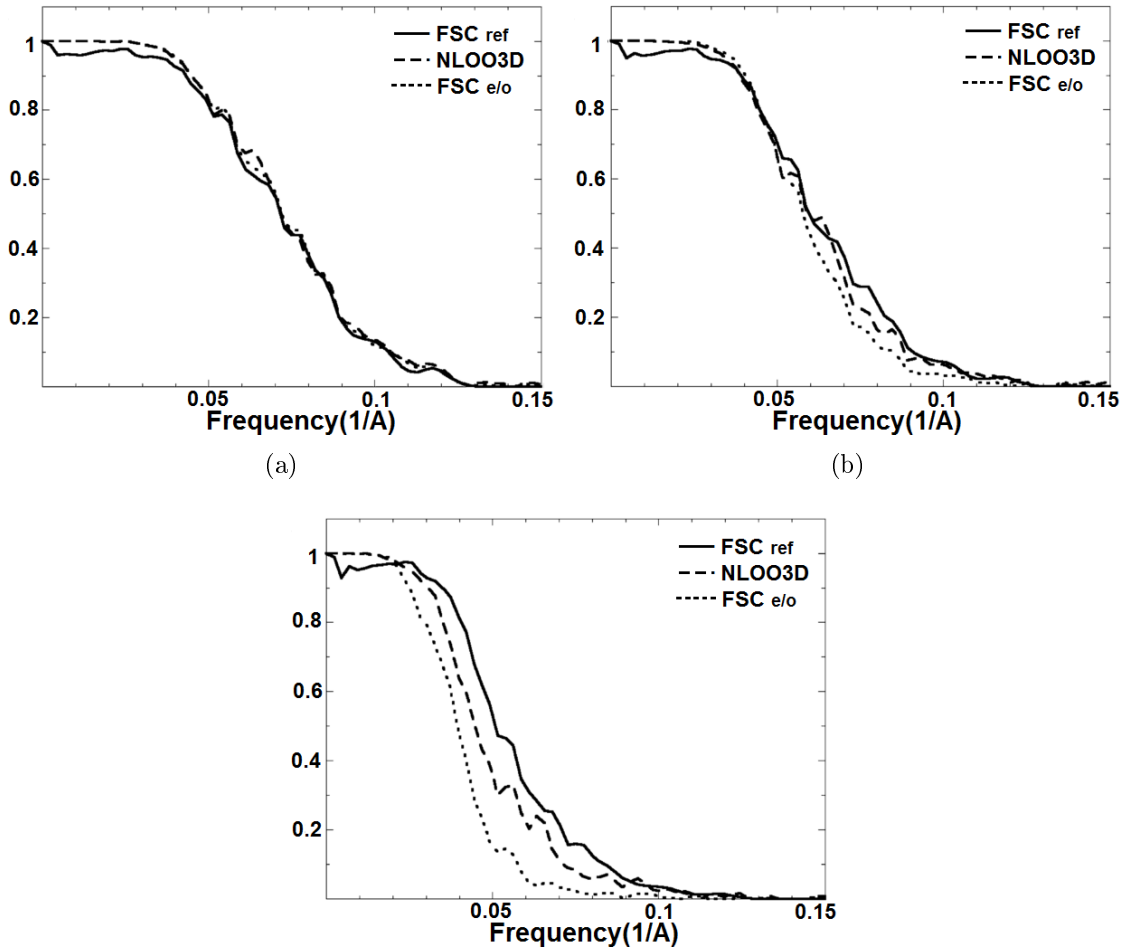

Figure 5.3 *Comparison of FSC_{ref}, $FSC_{e/o}$ and NLOO in measuring the resolution from one tomogram. Tilt angle ranges between* -68° *to* +68° *with angular increment of a)* 1° *b)* 2° *and c)* 4° *[52].*

5.1.4 Effective Estimation of Resolution in Incoherent Electron Tomography

Independent resolution determination along X, Y and Z axes enables us to survey the effect of different approaches in data acquisition and data reconstruction in each axis separately. Specifically, measuring the elongation artifact in Z-direction provides an important insight to assess data acquisition methods. As already mentioned, $FSC_{e/o}$ and NLOO do not take the resolution anisotropy into account [53] and estimate the average of resolution in all axes. Therefore, employing directional point speared function (PSF) can contribute to determination of resolution in each direction.

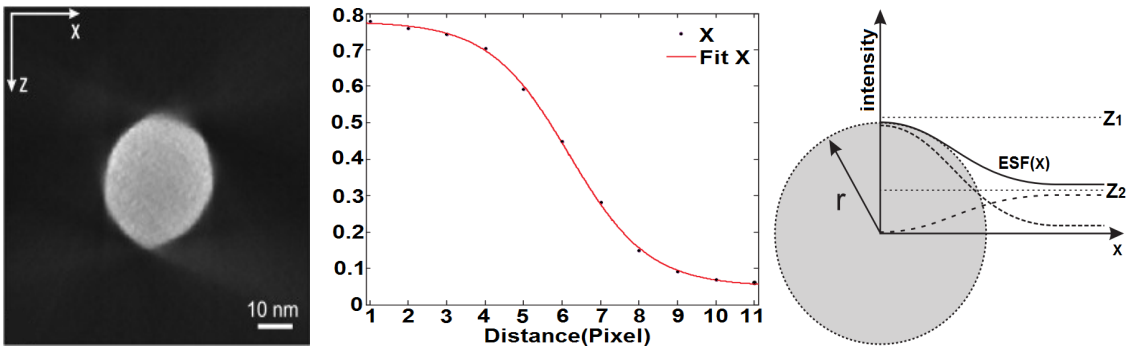

(a) (b) (c)

Figure 5.4 *a) Central slice of the reconstructed tomogram on XZ plane. b) Intensity profile (a) along the Z-axis as the function of distance from the center of tomogram. c) Fitting (b) on a hypothetical circle, in which the radius of the circle (r) represents the distance where the intensity is equal to* $(z_1 + z_2)/2$ *[53].*

Measuring the PSF in Z-direction is applied on gold particles where the intensity of the reconstructed tomograms is theoretically constant. Considering this assumption, two perpendicular slices from the center of reconstructed tomogram are taken. From the slices, three intensity profiles along the X, Y, and Z axes are extracted. Figure 5.4a shows the central section on XZ plane and Fig. 5.4b depicts the intensity profile along X-axis. Expectedly, the edges of the particles produce a step edge convolved with a 1D PSF, called Edge Spread Function (ESF). Now, to find a mathematical representation of ESF, intensity profiles are fitted in a sigmoid model as [53]:

$$ESF(x) = \frac{z_1}{1 + exp(\frac{r-x}{\tau})} + \frac{z_2}{1 + exp(-\frac{r-x}{\tau})}, \tag{5.7}$$

where, z_1 and z_2 are the intensities of the gold particle and the background respectively. x is the pixel number and r is where the intensity exactly stays between z_1 and z_2 and τ defines the width of step function (see Fig. 5.4c). Since PSF is the first derivative of ESF, calculating the first derivative of Eq. 5.7 results in a logistic distribution. The Full Width at Half Maximum (FWHM) of this distribution is the approximation of resolution which is equal to 3.53 τ. Figure 5.5 illustrates the relation between ESF and PSF and how to determine resolution from FWHM in PSF which is equal to 0.353 τ in ESF [53].

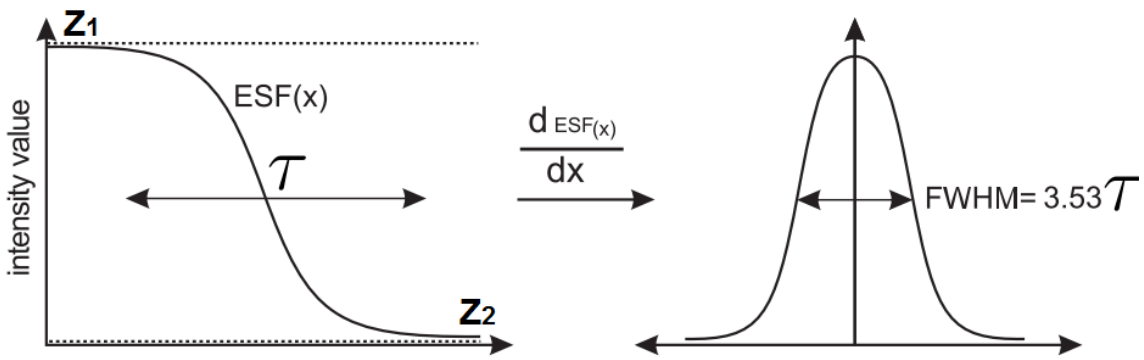

Figure 5.5 *The schematic of resolution determination using ESF and PSF. FWHM defines the resolution which is equal to 3.53 of* τ *[53].*

6. MATERIALS AND METHODS

To comprehend the effect of different factors in electron microscopy, several experiments were designed to examine the role of each in image formation. To implement the experiments, TEM-simulator developed by H. Rullgård *et al.* [10] was employed. Numerical phantoms are system's input and projection images are the output of the simulator. In this chapter, firstly we will explain the structure of two synthesized phantoms: 1) a high resolution phantom of a Male-Specific bacteriophage 2 (MS2 bacteriophage) and 2) a medium resolution phantom representing a texture of cells. Secondly, the EM adjustments for each experiment are demonstrated. However, as the simulator is comprised of many compartments, we will only focus on those which are relevant to our work.

6.1 Numerical Phantoms

6.1.1 MS2 Bacteriophage Phantom

To provide a phantom presenting realistic distribution of electron density within a molecule, MS2 bacteriophage is selected. Protein Data Bank (PDB) as the single repository of information about the 3D structures of proteins, nucleic acids and complex assemblies [57] archives the structure of lots of macromolecules such as MS2 bacteriophage. The PDB format is a standard representation of macromolecular structure data created in 1970 and used by numerous software packages till today. The PDB files are derived from X-ray diffraction and Nuclear Magnetic Resonance (NMR) studies [58]. The structure of a MS2 bacteriophage is discussed in detail in [59] and its PDB file is downloaded from [60]. The file specifies the structure of one unit of MS2 virus. To construct a bigger representation of the virus, several transformations are applied on this unit. Since the PDB format is not a voxel-based representation of the structures, we converted the PDB files to Medical Research Council (MRC) format to employ them as phantoms; The MRC becomes an indus-

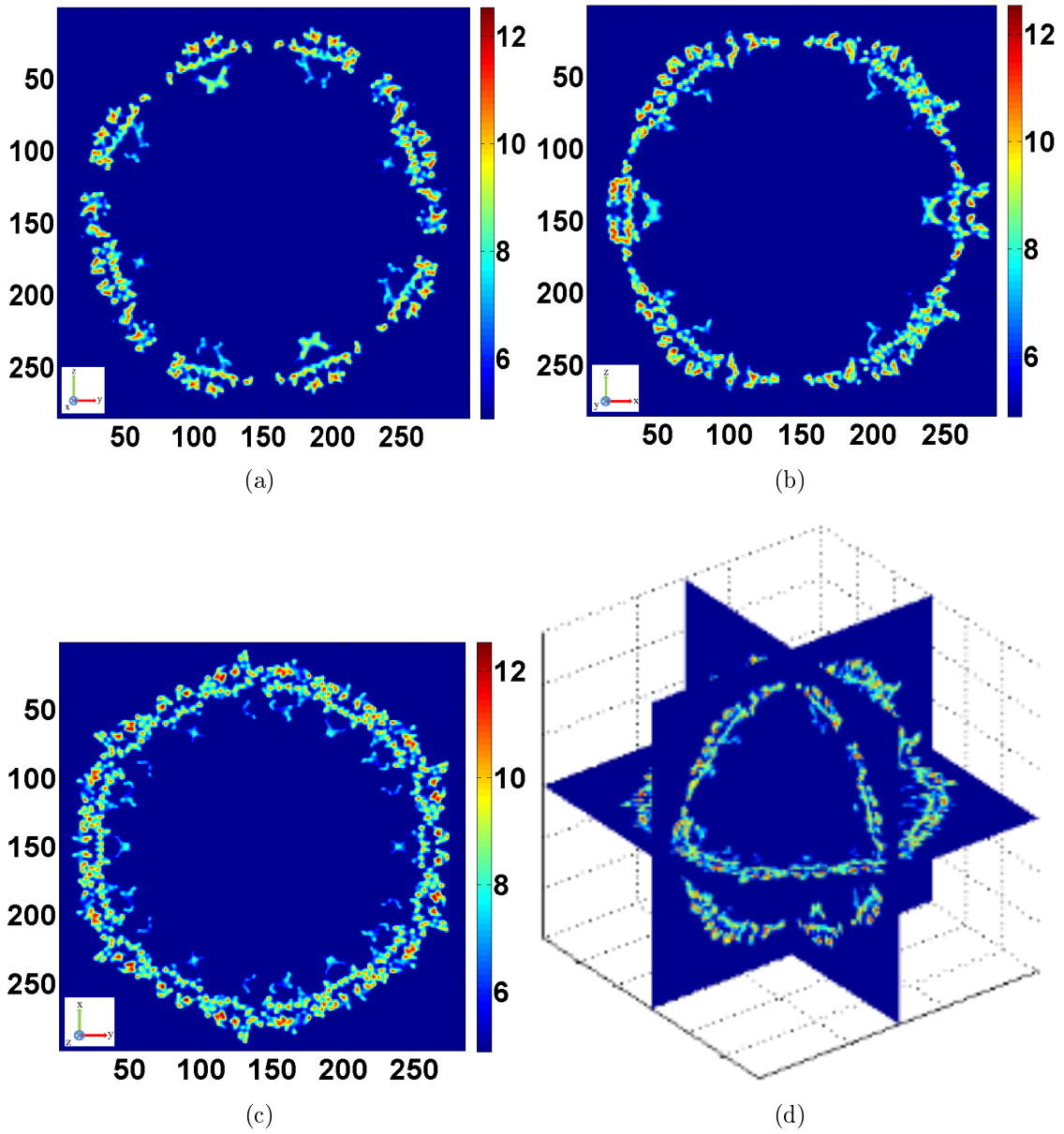

Figure 6.1 *150^{th} slice of MS2 bacteriophage phantom: a) YZ view b) XZ view c) XY view. d) 3D view of the phantom.*

try standard in cryo electron microscopy [61] and represents the map of electron density distribution. Moreover, we can define the voxel size before converting the PDB format to MRC. In our work, to generate a high resolution phantom, voxel size is selected as 0.1 nm. We will call this phantom MS2 bacteriophage phantom or shortly MS2 phantom. Figure 6.1 illustrates the 150^{th} slice of the phantom in YZ, XZ and XY view in addition to its 3D representation. Also, Table 6.1 demonstrates

the numerical properties of the phantom; a 300×300×300 volume with the electrostatic potential distribution in the range of 4.8 to 11.9. As MS2 phantom contains more details, it is employed for finding the optimal data acquisition parameters such as acceleration voltage, defocus value and electron dose. In terms of 3D reconstruction, MS2 phantom is more suitable for high resolution reconstruction techniques such as Single Particle Analysis (SPA) but not for the electron tomography; as the voxel size is 0.1 nm, generating an acceptable projection with appropriate contrast, magnification and meanwhile preserving the Nyquist sampling frequency requires high electron dose for each single projection. Imaging under this condition is not possible in ET as tens of projections are needed which pushes the total electron dose much higher than the allowable dose limits.

Table 6.1 *Properties of MS2 and cellular texture phantoms.*

Property	Voxel Size (nm)	Volume Size (pixel)	Volume Size (nm)	Min. Electrostatic Potential	Max. Electrostatic Potential
MS2 Bacteriophage Phantom	0.1	300×300×300	30×30×30	4.8	11.9
Cellular Texture Phantom	2.5	256×256×100	640×640×250	0.1	2.5722

6.1.2 Cellular Texture Phantom

For the simulation of electron tomography, a 3D phantom is required in which its projections contain decent SNR and contrast, even under low dose microscopy. Therefore, a representation of cellular texture is generated as a phantom with 2.5 nm voxel size and 640×640×250 nm length in X, Y and Z directions respectively. This phantom does not require high magnification for proper imaging and preserving Nyquist sampling frequency. Figure 6.2 illustrates the 128^{th} slice of the phantom in XZ and YZ planes, 50^{th} slice in XY plane and its 3D representation; cells are demonstrated as circles centered at random locations, containing random electric potentials between 0.1 and 2.57. Numerical properties of the phantom are presented in Table 6.1.

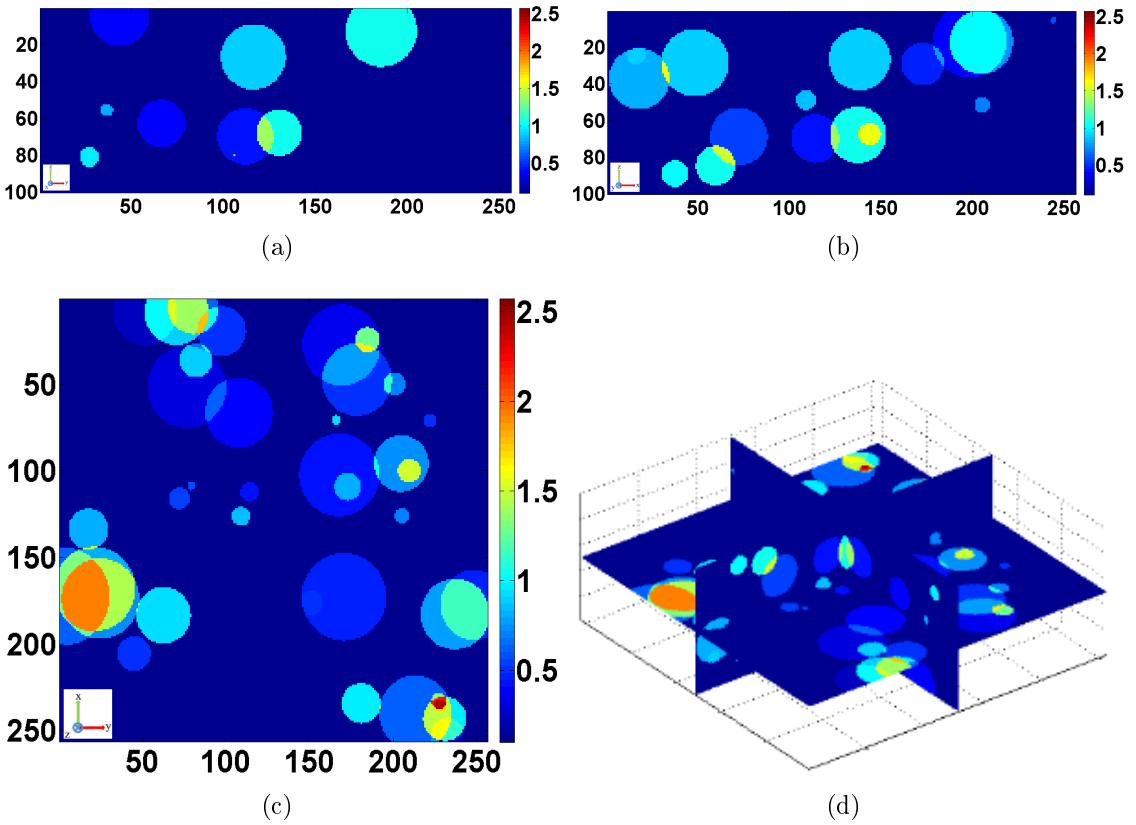

Figure 6.2 *128^{th} slice of cellular texture phantom: a) YZ view b) XZ view. c) 50^{th} slice of cellular texture phantom in XY view. d) 3D view of the phantom.*

6.2 Detector Calibration

Detector parameters such as C_{gain}, C_{dqe} and MTF -described in chapter2- are calibrated off-line, i.e. independent of any specimen. To calibrate the detector, blank images of real TEM and TEM simulator at a certain electron dose are compared. C_{gain} calibration depends on average number of counts in the readout and C_{dqe} adjusts the agreement of variance between simulated and experimental data. Calibration and setting of the MTF parameters contribute to agreement between the power spectra of the two blank images [10]. Table 6.2 defines Det.1 and Det.2 settings applied for detector adjustment; Det.1 setting is used in the of case MS2 bacteriophage phantom and Det.2 setting is applied when the cellular texture phantom is employed. Calibration of the MTF parameters in Det.1 and Det.2 are extracted from [10] and [24] respectively.

Table 6.2 *Det.1 and Det.2 are two settings for detector parameters.*

Property	Detector Plane (Pixel)	Pixel Size (nm)	C_{gain}	C_{dqe}	MTF -a	MTF -b	MTF -c	MTF -γ_1	MTF -γ_2
Det.1	400×400	15	10	0.4	0.7	0.2	0.1	10	40
Det.2	1024×1024	10	2	0.7	0.46	0.22	0.25	1724	24.5

6.3 High Resolution Imaging

For high resolution imaging, MS2 bacteriophage phantom which is embedded in ice is employed -the thickness of ice is 100 nm in the edge and 50 nm in the center. The impact of defocus value, acceleration voltage and objective diaphragm size are assessed with the resolution of 5 Å in 0° tilt angle; to refer to each experiment easier, we call them *Exp. Defocus*, *Exp. Acc_ voltage* and *Exp. Obj_ diaphragm* respectively. Total dose is set to 4000 e-/nm^2. Only in one experiment under the category of assessing acceleration voltage, total dose increases from 4000 e-/nm^2 to 6800 e-/nm^2; this experiment is called *Exp. Acc_ voltage* β. The aim of this experiment is to compare between contrasts produced by high acceleration voltage and high electron dose in one hand, and low acceleration voltage and low electron dose on the other hand. Those factors which remain constant during high resolution imaging will be described in Table 6.3 and those which change corresponding to each experiment are defined in Table 6.4.

Table 6.3 *Constant parameters of the simulator for high resolution imaging.*

Magnification	Spherical aberration[a] (mm)	Chromatic aberration[b] (mm)	Focal length of the primary lens (mm)	Aperture angle of the condenser (milliradian)	Beam energy spread (eV)
30000	2	2	3	0.1	1.3

[a] An optical problem occurs due to increased refraction of light rays when they strike a lens close to its edges, in comparison with those that strike closer to the center [62].

[b] A common optical problem which happens when a lens either does not bring all wavelengths of color to the same focal plane, and/or when wavelengths of color are focused at different positions in the focal plane [63].

Table 6.4 *Defocus value, acceleration voltage, objective diaphragm size and total electron dose for high resolution imaging.*

Experiment	Defocus Value (µm)	Acceleration Voltage (kV)	Objective diaphragm size (µm)	Total dose (e/nm^2)	Phantom
Exp. Acc_voltage	6	100,200,300	50	4000	MS2
Exp. Acc_voltage β	6	300	50	6800	MS2
Exp. Defocus	0,2,4,8	200	50	4000	MS2
Exp. Obj_diaphragm	6	200	10,50,100	4000	MS2

6.4 Medium Resolution Imaging

To evaluate the effect of different dose and angular distribution methods under the context of low dose electron tomography, cellular texture phantom is employed. Limited total electron dose and specimen thickness push the resolution to medium range -here 1 nm. Despite the limitations mentioned in the theoretical sections, to present better comparisons among different dose and angular distribution approaches, higher electron dose and resolution are selected. Six experiments (Exp.1-6) are designed to explore the role of dose and angular distributions on image formation.

To design the experiments, range of tilt angles is selected between $-60°$ and $60°$. In the first three experiments (Exp.1-3) only dose distribution models are considered. Constant, cosine and inverse-cosine[1] models of dose distribution are assessed while the total dose is constant. These three experiments (Exp.1-3) acquired by $1°$ incremental steps resulting in 121 projections. Then, two experiments individually specified for angular distribution. Experiments 4 and 5 employ Saxton and inverse-Saxton[2] methods for distributing 121 angular steps between $-60°$ and $60°$ while their dose distribution follows constant model. To define the initial increment step

[1]Distribution of electron dose is opposite to the cosine model of electron distribution. Therefore, projections with lower angles (around zero) receive higher electron dose and increasing the tilt angle declines the number of irradiated electrons.

[2]Opposite to Saxton angular distribution; sampling rate is high at low angles (around zero) and declines by increasing the tilt angle.

Table 6.5 *Constant parameters of the simulator during Exp.1-6.*

Acceleration voltage (kV)	Beam energy spread (eV)	Objective diaphragm size (µm)	Defocus value (µm)	Magnification	Resolution (nm)	Total dose (e-/nm^2)
300	0.7	20	6	10000	1	30250

Table 6.6 *Summary of angular and dose distribution methods for Exp.1-6.*

Experiment	Angular distribution	Dose distribution	Phantom
Exp.1	1°	constant model	cellular texture
Exp.2	1°	cosine model	cellular texture
Exp.3	1°	inverse-cosine model	cellular texture
Exp.4	Saxton method	constant model	cellular texture
Exp.5	inverse-Saxton method	constant model	cellular texture
Exp.6	Saxton method	cosine model	cellular texture

for the Saxton method, we need to define the desired number of angular steps or a limitation for the minimum exposure time/minimum electron dose. To take the latter strategy, the initial increment step was altered iteratively so that the condition of minimum electron dose was observed -the same approach is applied to find the initial increment step in inverse-Saxton method. In our experiments, to be able to compare the results of different experiments, total number of steps is selected as 121 which leads to 1.25° and 0.64° as initial increment steps in Saxton and inverse-Saxton models. Lastly in Exp.6, Saxton method of angular distribution is combined with cosine model of dose distribution to assess if the combination can enhance the quality of reconstruction better than the other methods.

Parameters which are constant among all the experiments are shown in Table 6.5 (values related to spherical aberration, chromatic aberration, focal length of the primary lens and aperture angle of the condenser lens can be found in Table 6.3). Imaging resolution is 1 nm according to 10,000 magnification and 1 µm detector pixel size. Table 6.6 shows the summary of angle and dose distribution methods employed for each experiment. Also, in the appendix precise values of the tilt angle and electron dose for each study are entailed.

7. RESULTS AND DISCUSSIONS

In the previous chapters, we introduced the theoretical backgrounds required for the data acquisition and reconstruction stages. We synthesized two numerical phantoms and designed several experiments, each of which demonstrates a data acquisition model. To compare the electron tomograms, we suggested various means of resolution measurement. This chapter presents the results of the experiments and evaluates them qualitatively and quantitatively. The order of the chapter is to firstly demonstrate and discuss projections of different TEM settings (optimal TEM adjustments are applied in experiments 1-6). Secondly, reconstructed tomograms from different dose and angular distribution models are assessed and compared in terms of RMS, resolution and elongation values. Table 6.4 and 6.6 of the previous chapter demonstrate the name and features of each experiment.

7.1 Acceleration Voltage

Acceleration voltage affects image formation in different contexts: specimen damage, mean free path, dose and contrast. Figure 7.1a-c show the projections of MS2 phantom acquired from Exp. Acc_voltage where the voltage varies from 100 kV to 300 kV while the dose is kept constant. Results show the variation of the contrast with respect to the acceleration voltage: electrons with low energy levels (accelerated with a low voltage) produce projections with better contrast compared to the electrons with high energy levels. Since highly accelerated electrons pass the specimen with fewer interactions, their corresponding projections suffer from low contrast (compare Fig. 7.1a and c). In addition, Fig. 7.1d depicts the output of the Exp. Acc_voltage β in which we intensified the electron dose for a constant acceleration voltage. In Fig. 7.1d acceleration voltage is 300 kV and electron dose increased from 4000 e-/nm^2 to 6800 e-/nm^2. As increasing the acceleration voltage (till a certain point) decreases the specimen damage, we can irradiate the specimen with more electrons. Result of this experiment indicates that we can compensate

the low contrast of the high acceleration voltages with dose augmentation (compare Fig. 7.1a and d). To conclude, note that to select an optimal acceleration voltage, type of the sample -organic/inorganic, specimen thickness, specimen damage, resolution and contrast of the projections should be considered at the same time. For imaging a thin bio-sample low voltages $\approx$ 80-120 kV are preferred. Increasing the sample thickness requires higher acceleration voltage. Keeping the specimen thickness constant, intensifying the acceleration voltage reduces the contrast. Moreover, high resolution imaging requires high acceleration voltages $>$ 300 kV due to the shorter electron wave length in high voltages compared to the low ones. As the experiments are simulation, we cannot cover the effect of specimen damage, however in real imaging either of very low and very high acceleration voltages damage the specimen.

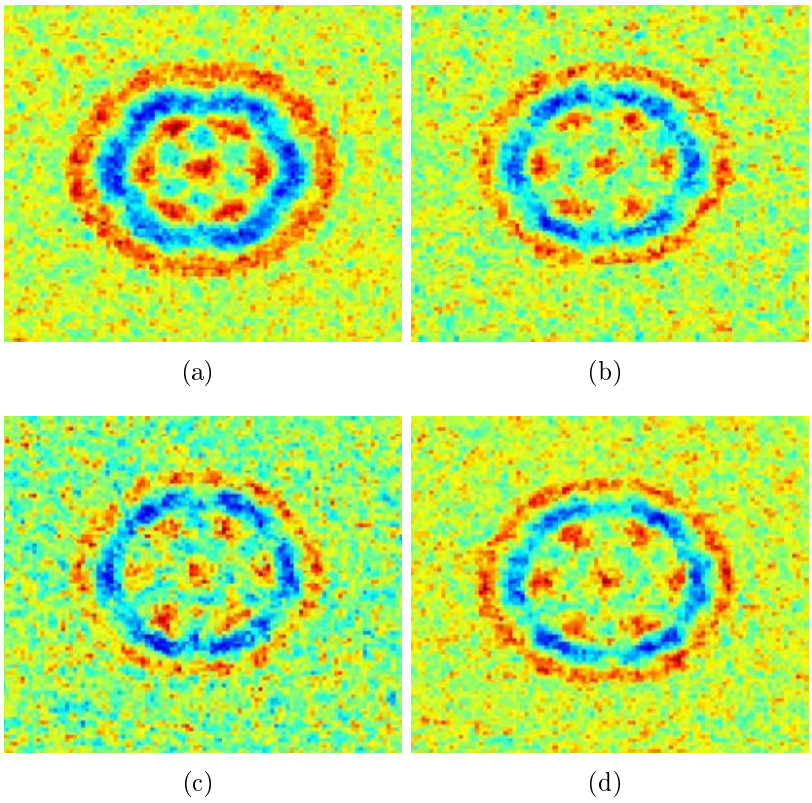

Figure 7.1 *Effect of acceleration voltage on image formation (MS2 phantom): a) 100 kV b) 200 kV c) 300 kV, when electron dose is 4000 e-/nm^2. d) The acceleration voltage is kept at 300 kV while the electron dose is increased to 6800 e-/nm^2.*

7.2 Defocus Value

To evaluate effect of defocus value on image formation, MS2 phantom was employed. The defocus value was altered from 0 to 8 µm while other factors remained constant (see Exp. Defocus in Table 6.4). Resultant projections of both noisy and noiseless simulations are depicted in Fig. 7.2; original images are 400×400 pixels, however images presented here are cropped to 100×100 pixels from the center.

To compare the results objectively, Fig. 7.3 plots the intensity profiles of both noisy and noiseless simulations of Fig. 7.2. The plots indicate how the outcome of an in-focus imaging (defocus is 0 µm) drowned in noise and lacks a meaningful profile. By increasing the defocus value from 0 µm to 8 µm the variance of the background reduces, the contrast improves and the similarity between the intensity profile of a noiseless projection with its corresponding noisy projection enhances. The reason is that large defocus values cause interfering of the scattered and unscattered electron waves which enhances the contrast of the projections. Nevertheless as a result, increasing the defocus value reduces the resolution of the projections. Note that the defocus value determines the first zero-crossing of the CTF function as well. So, a compromise between an appropriate contrast and preserving the details of the specimen is required; we select the largest defocus value with respect to the highest desired resolution. If the desired resolution is beyond the first zero-crossing of the CTF, then the acquired projections should be de-convoluted by their CTF function. As it is mentioned before, CTF correction is not required in electron tomography when the acquired resolution is within the first CTF zero-crossing point. In the current study, defocus value is selected in the range of 4-8 µm to generate projections with acceptable contrasts and in the meantime preserving the high resolution structures of the phantoms.

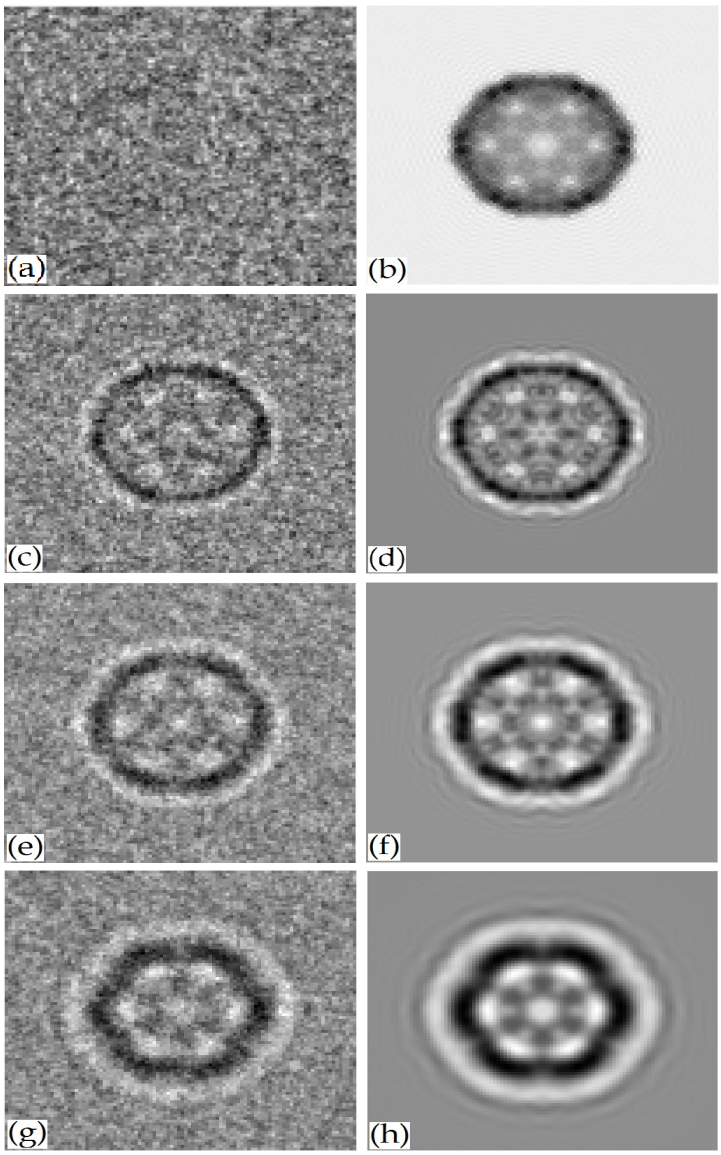

Figure 7.2 *Noisy (left column) and noiseless (right column) presentations of the projections under different defocus values (MS2 phantom): a,b)* 0 µm *c,d)* 2 µm *e,f)* 4 µm *and g,h)* 8 µm.

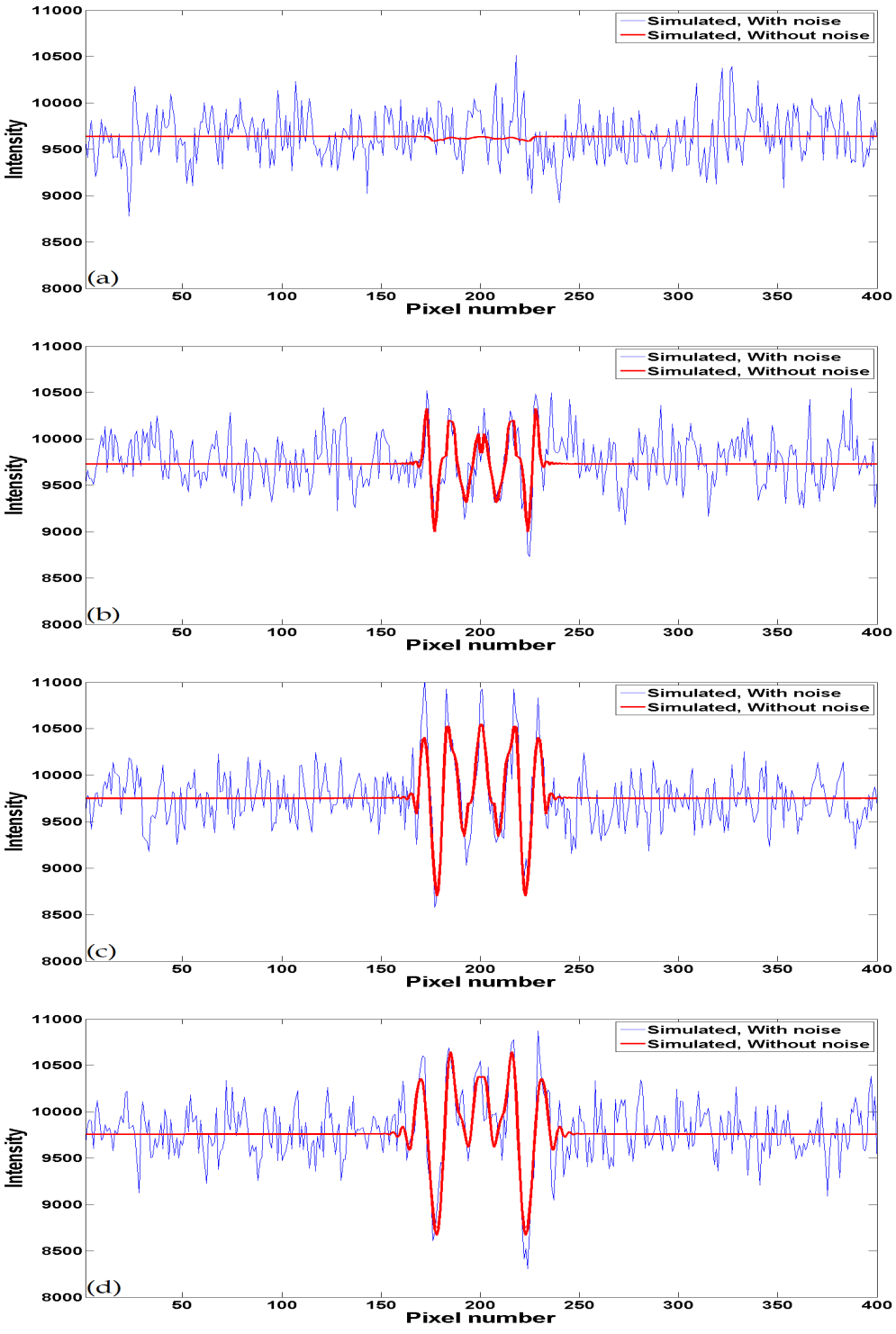

Figure 7.3 *Intensity profiles of the noisy and noise-free simulation pairs: a)* 0 µm *b)* 2 µm *c)* 4 µm *and d)* 8 µm. *Red and blue lines plot the noisy and noise-free simulations respectively.*

7.3 Objective Diaphragm

Figure 7.4 illustrates the projections resulted from different objective diaphragm size (10 µm, 50 µm and 100 µm) while MS2 phantom is employed. Theoretically, we expect that diminishing the objective diaphragm size boosts the contrast and declines the brightness of the projections by intercepting highly deflected electrons. Considering Fig. 7.4, among the projections slight differences of contrast are detectable. The projection acquired from a small aperture size (10 µm) appears sharper compared to the one corresponding to 100 µm aperture size. Diminishing the diaphragm size results in interception of large number of electrons deflected even with low angles. Thus, only those electrons which experience no electron-specimen interaction or experience it very weakly are allowed to pass small diaphragms. In such a condition projections contain sharper features. By enlarging the diaphragm size, even those electrons which are highly deflected by the interactions may pass the aperture and degrade the resultant projections in terms of contrast. Assessing the brightness of the projections, we can observe in Fig. 7.4a to c that the brightness is intensified as the diaphragm size enlarges: cold colors of the background alters to warm, since a large diaphragm size allows more electrons to pass and hit the detector.

At the end, to have a concise presentation of the effect of different TEM settings on image formation, we summarized them in Table 7.1. This table demonstrates the effect of increasing and decreasing of the acceleration voltage, defocus value and objective diaphragm size on the projections.

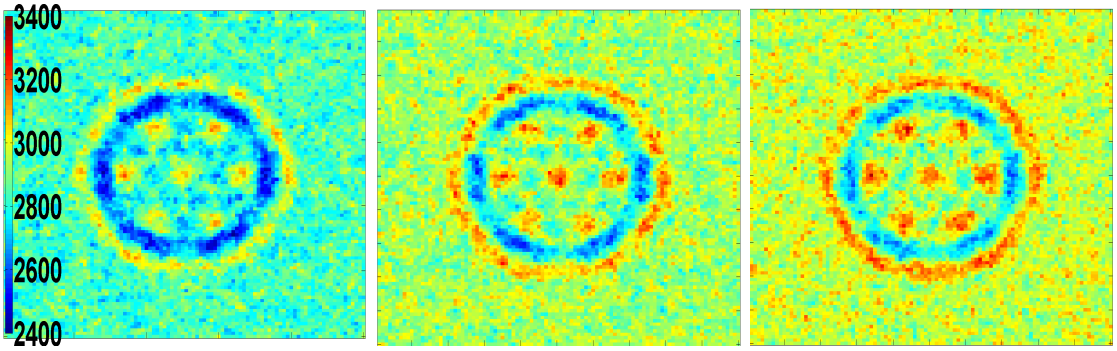

Figure 7.4 *Results of variation in objective diaphragm size (MS2 phantom): a)* 10 µm *b)* 50 µm *and c)* 100 µm.

Table 7.1 *Effect of different TEM settings in a summary.*

TEM setting	Increasing the value	Decreasing the value
Defocus value	Enhances the contrast	Reduces the contrast
	Blurs the high resolution structures	Preserves the high resolution structures
Acceleration voltage	Reduces the contrast	Enhances the contrast
	Thicker specimens can be applied	Suitable for thin samples and biological specimens
	Improves the resolution	Declines the resolution
	Increases the specimen damage by knock-on effect	Increases the specimen damage due to increasing the inelastic interactions
	Enhances the allowable total dose	
Objective diaphragm size	Reduces the contrast	Enhances the contrast
	Enhances the average number of electrons hitting the detector	Decreases the average number of electrons hitting the detector

7.4 Dose Distribution

In electron tomography, specimen damage is an important factor forcing us to consider deeply how to spend our limited number of electrons; we desire the highest isotropic resolution with the lowest specimen damage. Here, results of different dose distribution approaches are assessed in the projection stage.

In the case of the constant dose distribution all projections receive equal number of electrons, i.e. $30250/121 = 250$ e-/nm^2 for 121 projections. When dose distribution follows the cosine or inverse-cosine models, number of electrons per projection is relative to the cosine of the tilt angles. In the cosine model, the projections with low tilted angles receive fewer electrons since the effective thickness of the specimen is small. Tilting the specimen toward high angles enhances the specimen thickness which necessitates electron dose increment. For instance, in $\pm 60^\circ$ the specimen thickness is doubled in comparison to 0°, thus the electron dose. The cosine model of electron distribution contributes to keeping the SNR level approximately constant in a tilt series. In the inverse-cosine model of electron distribution, we decline the number of electrons by increasing the tilt angle, so that the low angles are irradiated with more electrons compared to the highly tilted angles. Applying the inverse-cosine model intensifies the contribution of low tilted angles in the reconstruction compared to the high angles. Figure 7.5 plots the generated intensities of the constant, cosine and inverse-cosine models against the tilt angles, when no specimen is involved. Considering the projections in the range of 0°-60°, intensity of the constant model drops exponentially due to increment of the transience path. Intensity of the inverse-cosine model declines steeply, since dose distribution model strengthened the effect of the transience path increment. In this case, projections corresponding to the low angles are almost 4 times brighter compared to the high angles. Intensity of the projections related to the cosine model of dose distribution is kept approximately constant throughout the tilt range (almost till 50°). The reason is that we compensated the effect of the transience path increment in the high angles by irradiating them with more electrons. To produce an almost perfect constant intensity against the tilt angles, the cosine model can be substituted with an exponential model of dose distribution.

To study more illustratively about the differences among dose distribution models, Fig. 7.6 depicts the results of Exp.1-3 (Table 6.6 defines the experiments) where each row corresponds to a model: the constant, cosine and inverse-cosine models

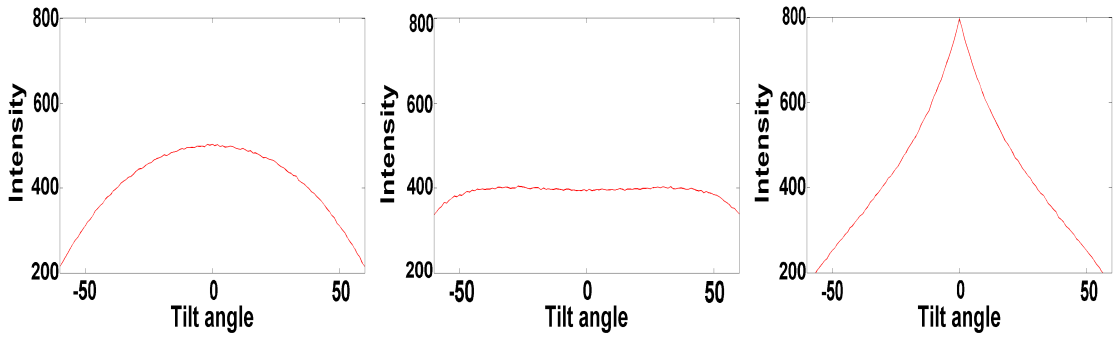

Figure 7.5 *Average intensity measured by detector from an area where the specimen is not present -rows 1:100- for different dose distribution methods: a) Constant model b) Cosine model C) Inverse-cosine model.*

are arranged from top to bottom. Projections are acquired from the cellular texture phantom. Total dose is 30250 e-/nm^2 and the number of the projections is 121 for all three experiments. Moreover, each column represents a micrograph corresponding to 0°, 30° and 60° tilted specimen from left to right. Comparing the images horizontally -intra model, increasing the tilt angle reduces the contrast, as the effective specimen thickness enhances. Moreover, average number of electrons reaches to the detector declines and deteriorates image formation in high angles (see the gradual alteration of warm colors into cold colors in each row of Fig. 7.6; range of the color-bars is constant for all the subfigures). Comparing the images vertically -inter model for the same tilt angle- shows that in low angles the contrast of the inverse-cosine model is better than the other two methods. However, by increasing the tilt angle contrast in the constant and inverse-cosine models drops dramatically. In high angles the cosine model results in the best contrast compared to the other methods. Applying the cosine model keeps the SNR constant in a tilt series.

To illustrate the effect of electron dose on contrast, intensity profiles corresponding to 0° tilt angle of Exp.1-3 (first column of Fig 7.6) are depicted in Fig. 7.7. The profiles are extracted from the 512^{th} row of the projections. In 0° angle, the electron dose of the constant model is 250 e-/nm^2, for the cosine model is 197.8 e-/nm^2 and for the inverse-cosine model is 398.2 e-/nm^2. The profiles indicate that applying higher electron dose generates sharper edges and enhances the contrast; the difference between highest and lowest intensities in Exp.3 is approximately 350 units while in Exp.1 and 2 is about 200 and 150 units respectively.

To conclude, it is guaranteed that the dose increment enhances the SNR. However as the total dose is highly restricted, it is important to consider how we distribute the dose in a tilt series to reconstruct high quality images. Effect of different data acquisition methods on the reconstruction will be evaluated in the following sections.

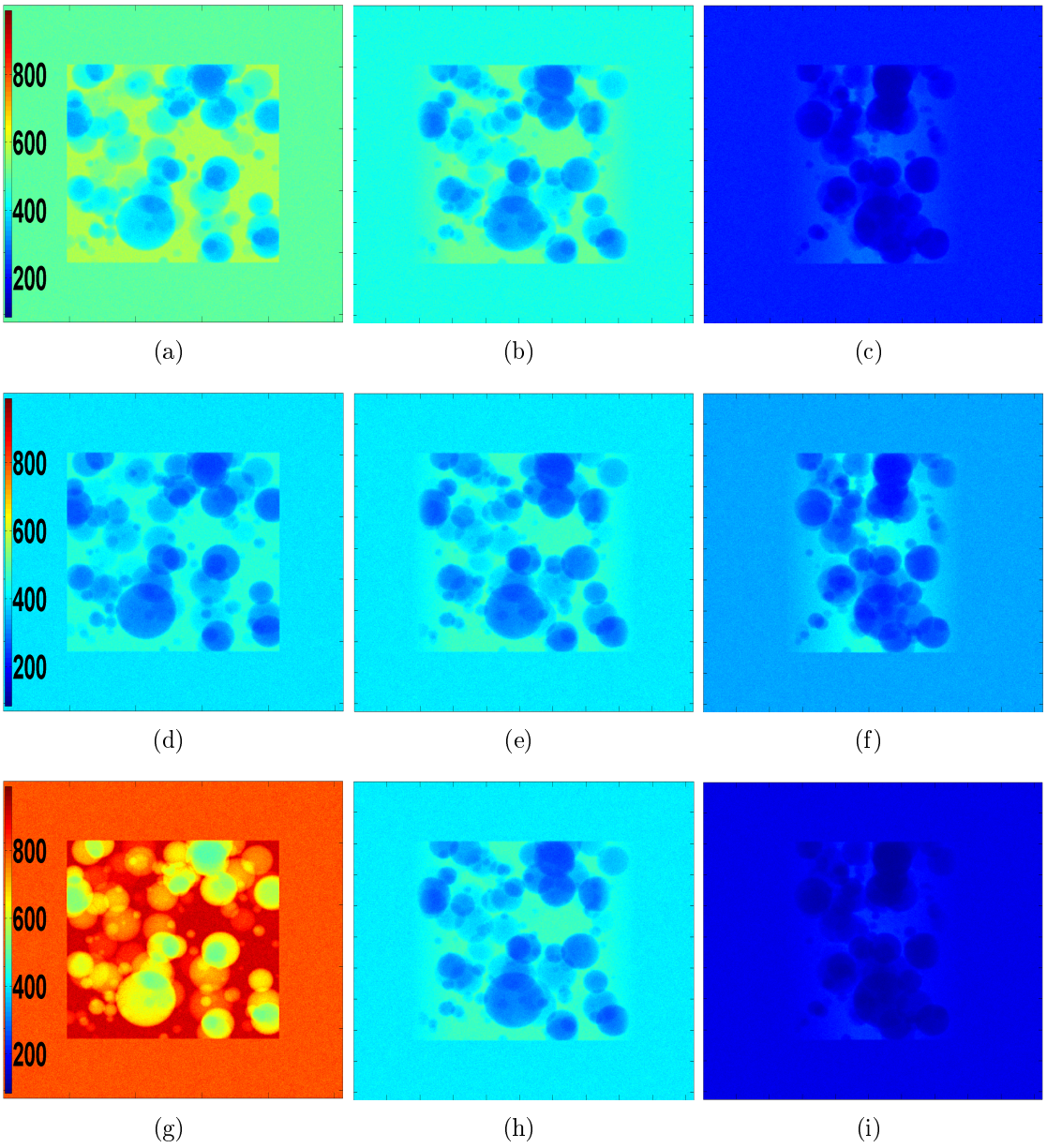

Figure 7.6 *Each row of figures corresponds to a model of dose distribution: constant, cosine and inverse-cosine models from top to bottom. Each column of figures corresponds to a tilt angle: 0, 30 and 60 degrees from left to right. Projections are acquired from the cellular texture phantom.*

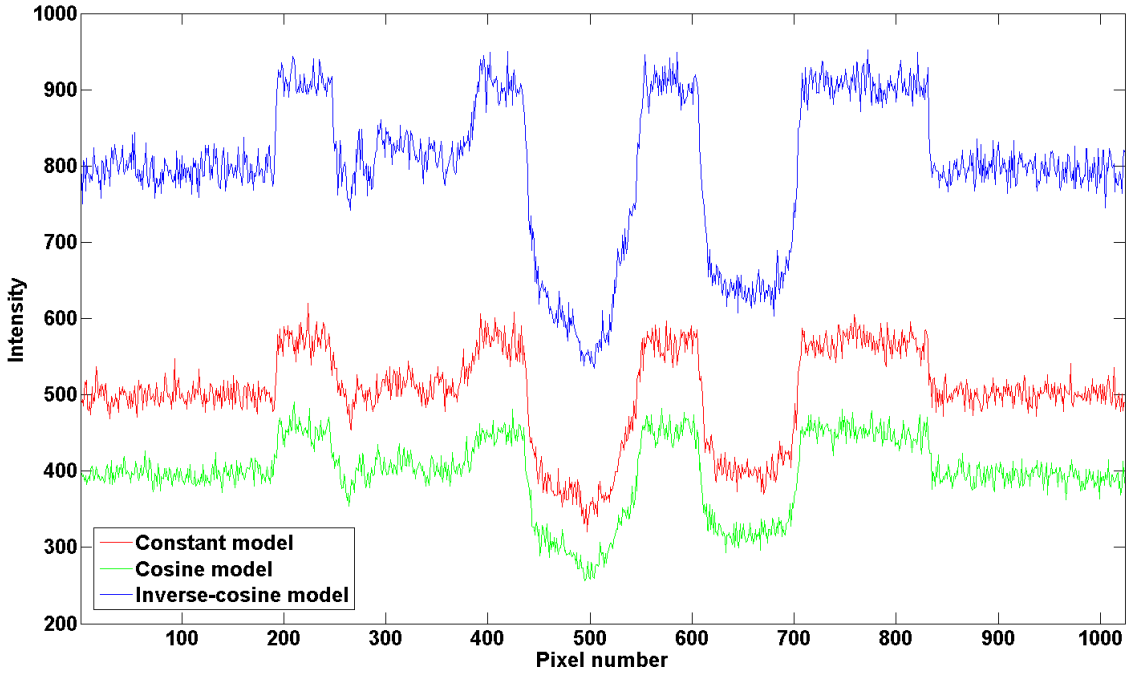

Figure 7.7 *Intensity profiles corresponding to* 0° *tilt angle for constant (red line), cosine (green line) and inverse-cosine (blue line) models of dose distribution.*

7.5 Reconstruction of Different Data Acquisition Methods

Noise, missing wedge and slab geometry of the sample cause resolution anisotropy in different directions of the reconstructed tomograms. To enhance the resolution, diverse approaches of dose and angular sampling are examined through Exp.1-6 (Table 6.6 defines the experiments). Acquired projections form the cellular texture phantom are reconstructed with FBP algorithm applying Hamming filter with the cut-off frequency of 0.5×Nyquist frequency. After reconstruction, to prepare the images for quantitative comparisons, firstly all negative values are set to zero. Then, the dynamic range of images is scaled to the range of the ground truth. To do so, a linear transformation is required to minimize the squared average of difference between ground truth and reconstructed images. Figure 7.8 and 7.9 show the middle slice of the reconstructed tomograms of the cell texture phantom from Exp.1-6 in XZ and XY planes respectively. As already mentioned, we define X-axis as the horizontal axis of the projection images, Y as the tilt axis, and Z as the direction of the electron beam.

Comparing the images subjectively in terms of dose distribution in Exp.1-3, the

cosine model generates images with sharp edges and low elongation in Z-direction. Saving electrons from low tilted angles and specifying them in high tilts leads to more homogeneous series of projections -the average of detected intensity is almost constant for all projections- and more edge-preserved reconstructions. With this approach, we equalize the role of all angles in the image reconstruction. In the other words, the cosine model of dose distribution neutralizes the effect of increment of the transience path during the specimen tilt. Thus, projections from the high tilts obtain the same contribution in the image reconstruction as the projections of the low tilted angles. On the other hand, employing the constant and inverse-cosine dose distribution methods deemphasizes the SNR of the high angles and thus their contribution in the image reconstruction. As a result, the elongation artifact increases and the resolution in Z-direction declines. So, the more the role of the high tilts decreases, the more the elongation artifact intensifies. Consequently, reconstruction of the projections acquired from the inverse-cosine model suffers more from the elongation artifact compared to the constant model of dose distribution.

Comparing the data acquisition approaches in terms of angle distribution, reconstructions of the experiments 1, 4 and 5 should be taken into account. As mentioned, FBP algorithm applying Hamming filter with the cut-off frequency of 0.5×Nyquist frequency is employed for the reconstruction task. Dose distribution for these three experiments obeys the constant model, so they differ only in the angle distribution method. Referring Fig. 7.8 and 7.9, Saxton's model reduced the elongation artifact more than other approaches which implies that increasing the sampling rate in the high angles enhances the resolution in Z-direction. Employing Saxton's model causes oversampling of the Fourier space in the regions close to the missing wedge. Therefore, we compensate the lack of SNR in highly tilted angles with the increment of the sampling frequency. Assessing the other angular sampling models verifies the conclusion: applying the inverse-Saxton model and the constant model of angle distribution has adverse effects on the reconstruction due to undersampling of the regions near to the missing wedge. Note that, when the cosine model of dose distribution and Saxton's approach combine together in Exp.6, the resultant reconstruction is boosted and shows the best subjective results. The reason is that we intensify the SNR of the projections corresponding to the high angles and increase the sampling rate in the regions close to the missing wedge at the same time resulting in a significant reduction in the elongation artifact.

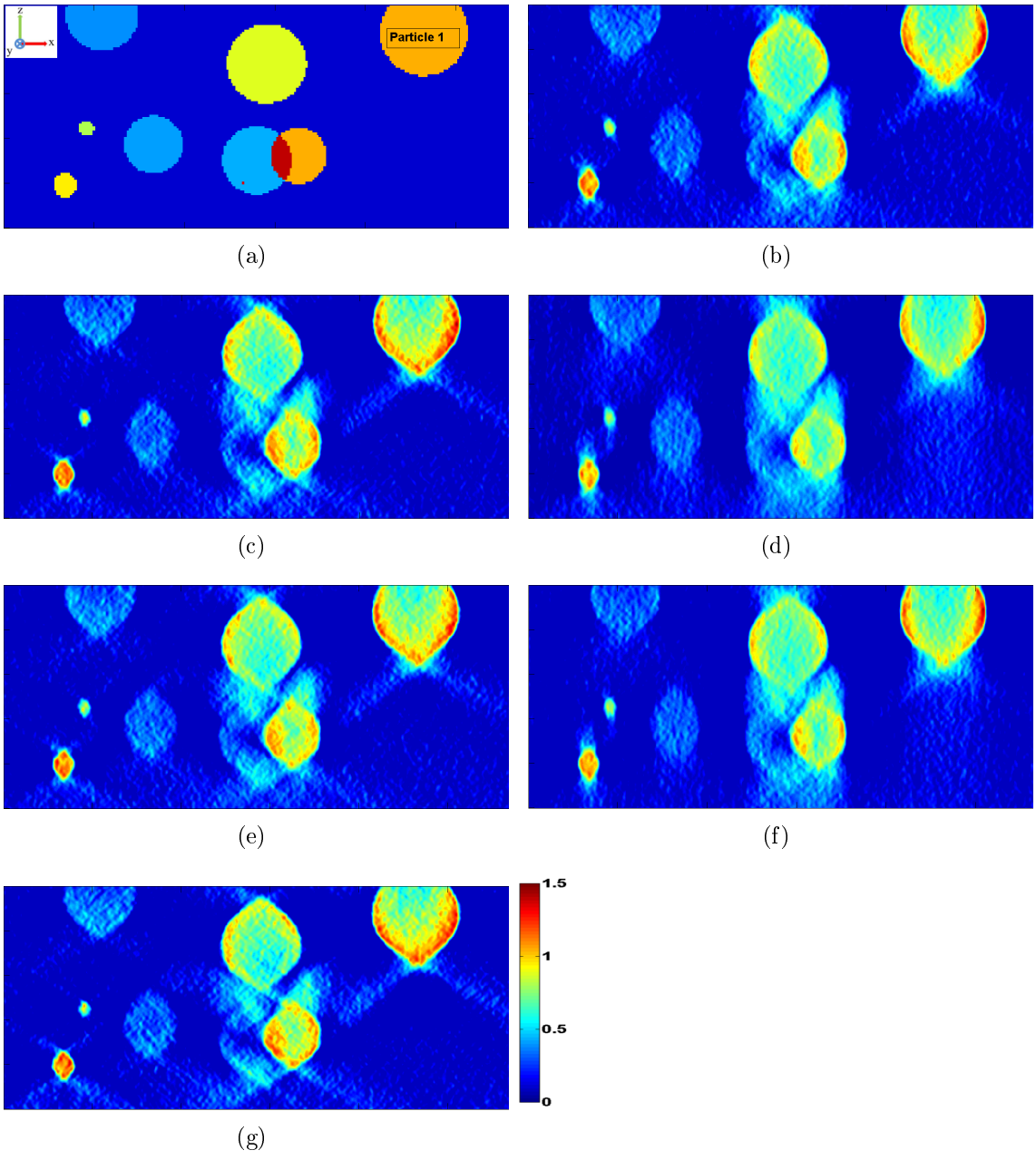

Figure 7.8 *a) Ground truth (cellular texture phantom). b-g) Reconstructed images of Exp.1-6 in XZ plane, employing FBP algorithm applying Hamming filter with cut-off frequency of 0.5×Nyquist frequency. Color bar for all figures ranges between 0 and 1.5.*

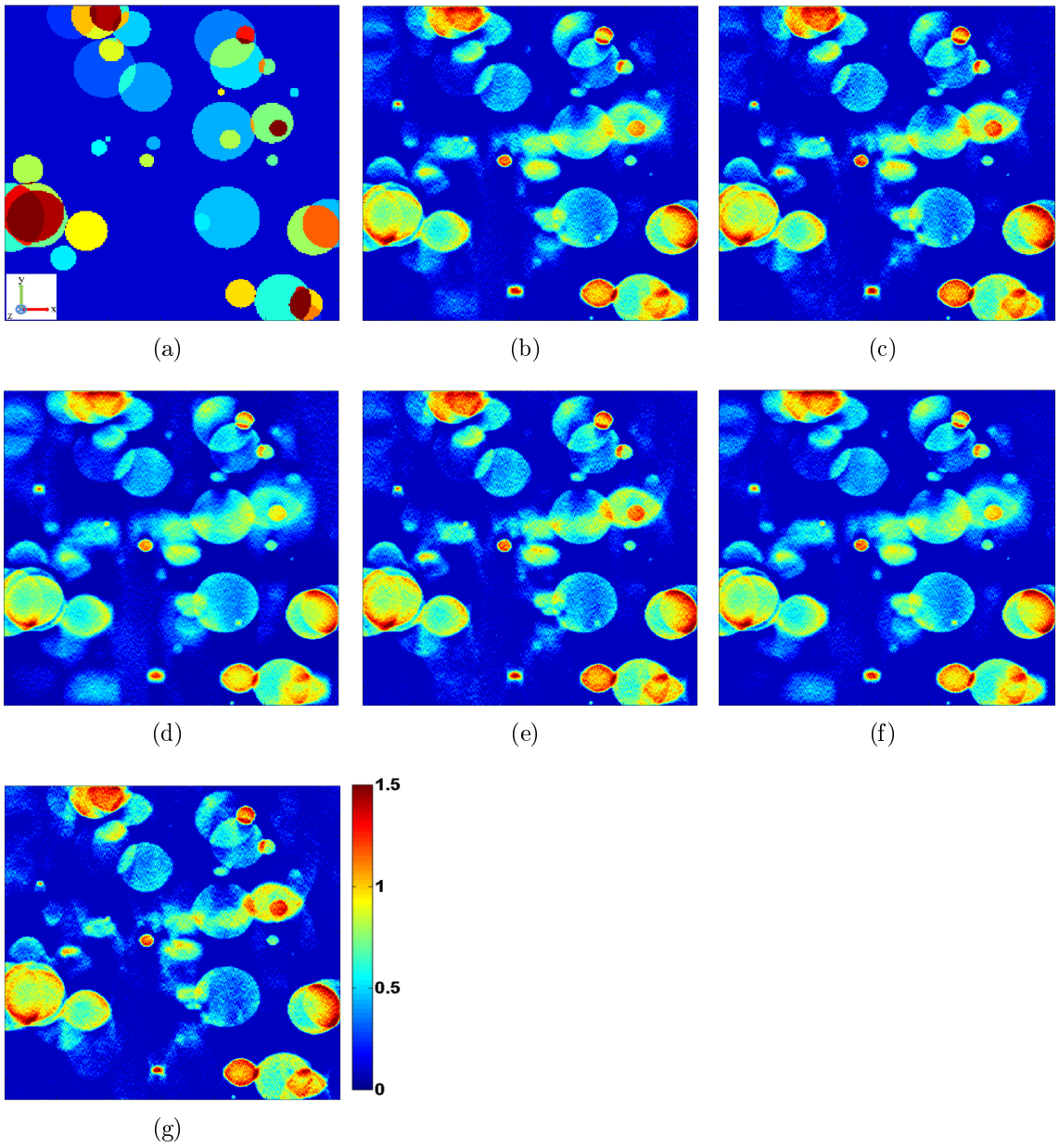

Figure 7.9 *a) Ground truth (cellular texture phantom). b-g) Reconstructed images of Exp.1-6 in XY plane, employing FBP algorithm applying Hamming filter with cut-off frequency of 0.5×Nyquist frequency. Color bar for all figures ranges between 0 and 1.5.*

7.6 Quantitative Assessment

7.6.1 Root Mean Square (RMS)

Root mean square (RMS) values corresponding to Exp.1-6 in XZ and XY planes are presented in Table 7.2. Definition of each experiment is described in Table 6.6. As stated before, employed phantom for these experiments is the cellular texture phantom. We applied filtered back projection (FBP) method for reconstructing the acquired projections, as it is the golden standard in image reconstruction. Hamming filter with the cut-off frequency of 0.5×Nyquist frequency is used in FBP. Final reconstructed images used for the quantitative assessments are scaled with respect to the ground truth. Inspecting the results numerically shows that among different dose distribution methods (Exp.1-3) the cosine model obtains the best RMS value. The RMS values imply that reducing the SNR of the highly tilted angles decreases their contribution in the image reconstruction and has adverse effects on it. Among different angle distribution approaches (Exp.1, 4 and 5) Saxton model gains the lowest RMS. The results imply that oversampling the Fourier space of the high angles improves the quality of the tomograms. Finally, the tomogram which employed both the cosine and Saxton methods (Exp.6) gains the smallest RMS value among all the experiments. Considering Table 7.2, the worst RMS values belong to the inverse-cosine model of dose distribution and inverse-Saxton model: the former method neglects the SNR of the projections corresponding to the regions of high angles and the latter suffers from undersampling of the Fourier space of this regions. In the previous section, subjectively we showed that the cosine model of dose distribution and Saxton's model reduce the elongation artifact, here the RMS values demonstrate the same results: the less the elongation artifact, the better the RMS value.

Table 7.2 *RMS values corresponding to the reconstructed images of Exp.1-6.*

Experiment	Exp.1	Exp.2	Exp.3	Exp.4	Exp.5	Exp.6
RMS (XZ plane)	0.1472	0.1403	0.1630	0.1424	0.1552	0.1390
RMS (XY plane)	0.234	0.2235	0.2519	0.2254	0.2459	0.2196

7.6.2 FRC_{ref}

Since the ground truth is known in advance (cellular texture phantom), to measure the resolution of the reconstructed images FRC_{ref} is employed. In the absence of

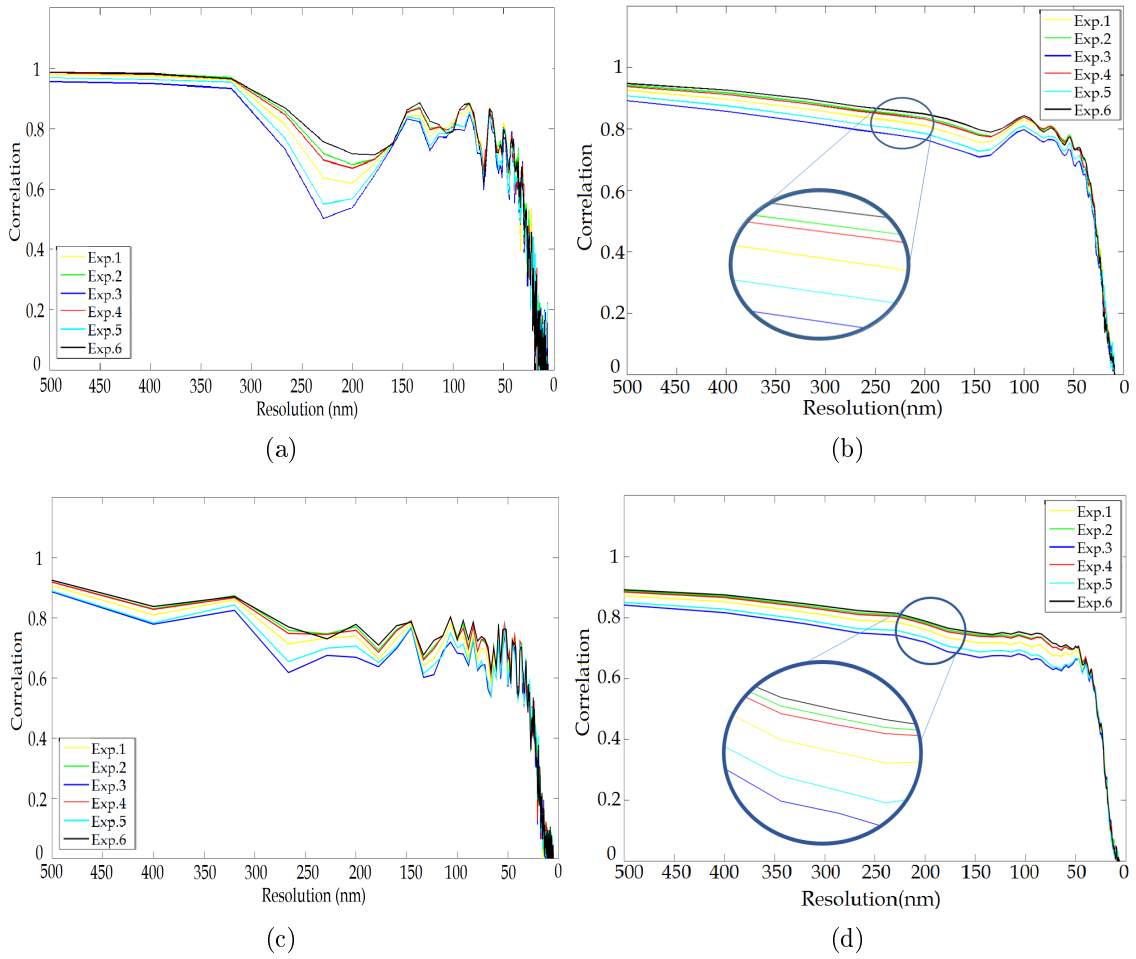

Figure 7.10 *FRC curves corresponding to the reconstructed images of Exp.1-6 in XZ (first row) and XY (second row) planes. a,c) the circular shape of the particles inside the reconstructed images causes hardly rugged FRC curves. b,d) moving average filter smooths the FRC curves -an arbitrary area for resolution > 100 nm is zoomed.*

the ground truth $\mathrm{FSC}_{e/o}$ can be considered as a substitution. Figure 7.10a and c illustrate how the FRC curves decline when the resolution increases. As the reconstructed images comprises of several " *circle form objects* " their corresponding FRC curves are rugged and need to be smoothed with a moving average kernel -here we applied an averaging filter with size 5 (see Fig. 7.10b and d). Considering the smoothed curves and 50% correlation criteria, average resolution of 28-29 nm can be approximated for all the reconstructions in both XZ and XY planes. Note that the FRC curves illustrate the average of the resolutions in all directions, and not directional resolution. Here, for both XZ and XY planes we have estimated the same resolutions $\approx$ 28-29 nm, despite the fact that the resolution in XZ plane is worse

than XY plane, since the elongation artifact occurs more heavily in XZ plane.

Considering the FRC curves, they do not allow us to judge the quality of the reconstructions clearly, since the curves are heavily twisted and entangled in high resolutions. However, observing their behavior in low resolutions >100 nm, they show an order on their resolving power: experiment 6 which advantages both the cosine dose distribution and Saxton method obtains the highest resolution. Experiments 2 and 4 which advantaging from either the cosine dose distribution or Saxton model generate almost the same reconstruction resolutions and ranked after Exp.6. Resolution of the images reconstructed from Exp.1 with the constant dose and angle distributions are worse compared to Exp.2, 4 and 6. Finally, inverse-Saxton model of angle distribution and inverse-cosine method of dose distribution obtains the lowest/the worst resolutions in comparison with the other methods. The order of the resolution results interpreted from the curves matches the order of the RMS values as expected.

7.6.3 Resolution Measurement in Z-Direction

In this section, we consider the middle slice of the reconstructed tomograms along Y-direction (each slice is in XZ plane) as the reference of our assessments. To extract proper edges in Z-direction, an object which shows the elongation effect more vividly is selected (particle 1 with respect to Fig. 7.8a). Now considering the ground truth, 10 vertical edges are selected from an area which contains both part of the object (particle 1) and background. Red lines in Fig. 7.11a illustrate the location of the extracted edges on the reconstructed slice of Exp.1, each of which comprising of 60 pixels long. To sample the intensity of the background adequately, the edges are elongated in the background. Since the intensity of the reconstructed particles declines towards their center, we selected the edges not deep in the particle side. Figure 7.11b shows the intensity of the extracted edges, starting from the particle and ending in the background. To fit a sigmoid function into the intensity profiles with a better approximation, the first intensity value of each edge is replicated for 20 times leading to Fig. 7.11c. Considering Eq. 5.7, for each edge an individual sigmoid function is fitted, and to determine the final ESF all sigmoids are averaged. It is important to consider that, averaging is imposed on the acquired sigmoids and not on the intensity profile of the edges, as by averaging them we neglect the effect of noise. Figure 7.12 (left column) shows the intensity values with blue circles and their corresponding average sigmoid with a red line as the ESF. Point spread

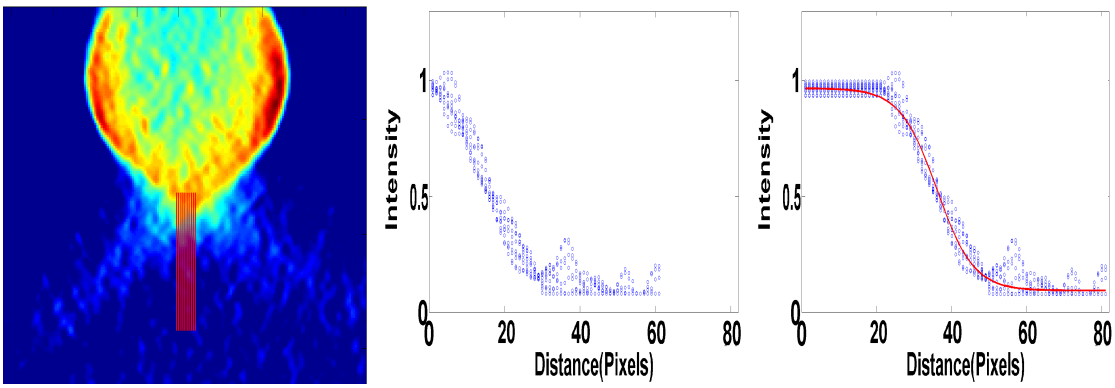

(a) (b) (c)

Figure 7.11 *a) Particle 1 from the reconstructed image of Exp.1 which illustrates how to select several vertical edges for ESF determination. Red lines show selected vertical edges each of which 60 pixels long. They are extracted based on the shape of particle 1 in the ground truth. b) Intensities corresponding to all edges. c) As the penetration of selected edges in the object part is short, the first intensity value of each edge is replicated for 20 times, thus the intensity profiles resemble a sigmoid function.*

function (PSF) is the first derivative of the ESF, thus we can calculate the PSF of each image. Corresponding PSF of each ESF is plotted in the right column of Fig. 7.12. The resolution can be determined by measuring full width at half maximum (FWHM) of PSF which is equal to $3.53 \times \tau$ according to Eq. 5.7; the thinner the plot the higher the resolution. Considering the resolution results in Table 7.3, the cosine dose distribution approach generates better resolution in Z-direction in comparison to the constant and inverse-cosine models of dose distribution. Furthermore, among different angle distribution methods, the Saxton model is superior in terms of resolution in Z-direction. The best resolution belongs to Exp.6 which advantages both the cosine and Saxton's methods at the same time. Resolutions in Z-direction strongly empower the previous interpretations acquired from the RMS and FRC_{ref} measurements. Note that the estimated resolution applying FRC_{ref} was about 28-29 nm, while referring to Table 7.3 resolution measurement in the Z-direction indicates worse results -except for Exp.6. The reason is that the output resolution of the FRC_{ref} approach is the average resolution of all directions, and since the resolutions in X- and Y-directions are better than Z-direction, the average resolution obtains better results. In addition, measuring the resolution in Z-direction is highly influenced by the elongation artifact which worsens the resolution in comparison to the other directions.

Table 7.3 *Resolution of the reconstructed images corresponding to Exp.1-6 in Z-direction. Images are reconstructed using FBP algorithm, applying Hamming filter with the cut-off frequency of 0.5×Nyquist frequency.*

Experiment	Exp.1	Exp.2	Exp.3	Exp.4	Exp.5	Exp.6
Resolution (nm)	43.39	34.62	44.71	33.52	49.21	24

To conclude, if we consider Exp.1 (constant dose distribution and constant angle distribution) as a benchmark among all data acquisition approaches, the resolution in Z-direction will improve if the emphasis on the high angles enhances. The emphasis can be regarded to intensifying the irradiation dose or increasing the sampling frequency. The former compensates for the increment of the transience path in highly tilted angles and the latter oversamples the Fourier space in this region. Considering the resolution of the benchmark, the results show that the cosine model of dose distribution enhances the resolution about 1.25 times and the Saxton model increases the resolution about 1.29. Combination of these two methods in Exp.6 enhances the resolution about 1.81 which is the best resolution among all approaches.

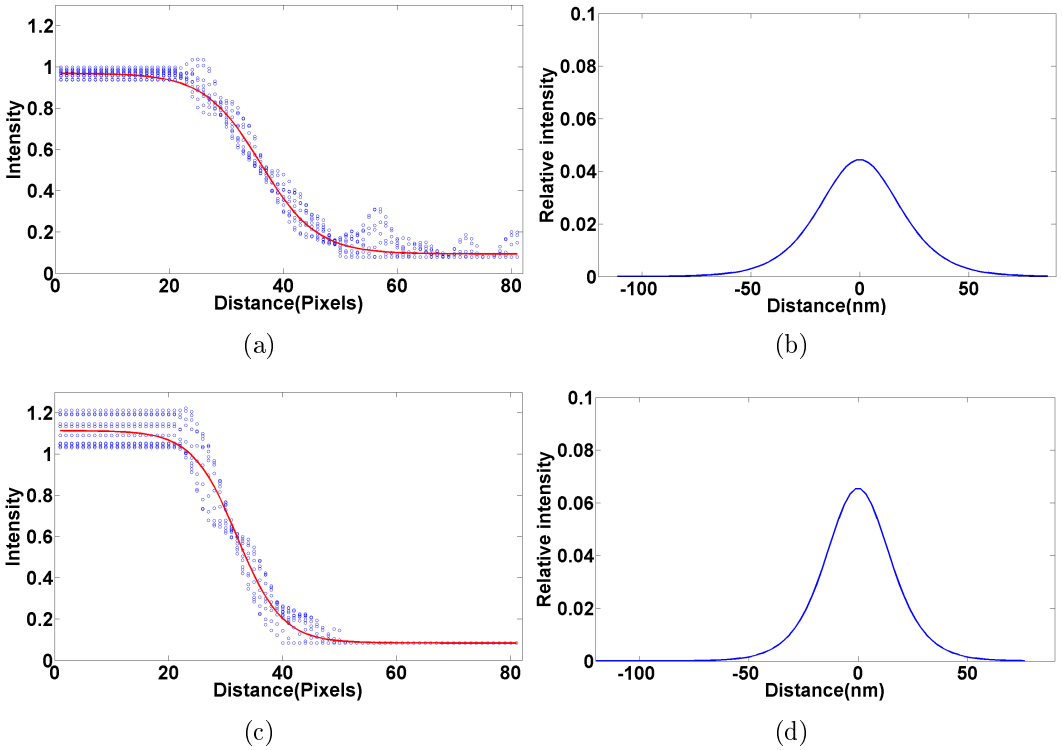

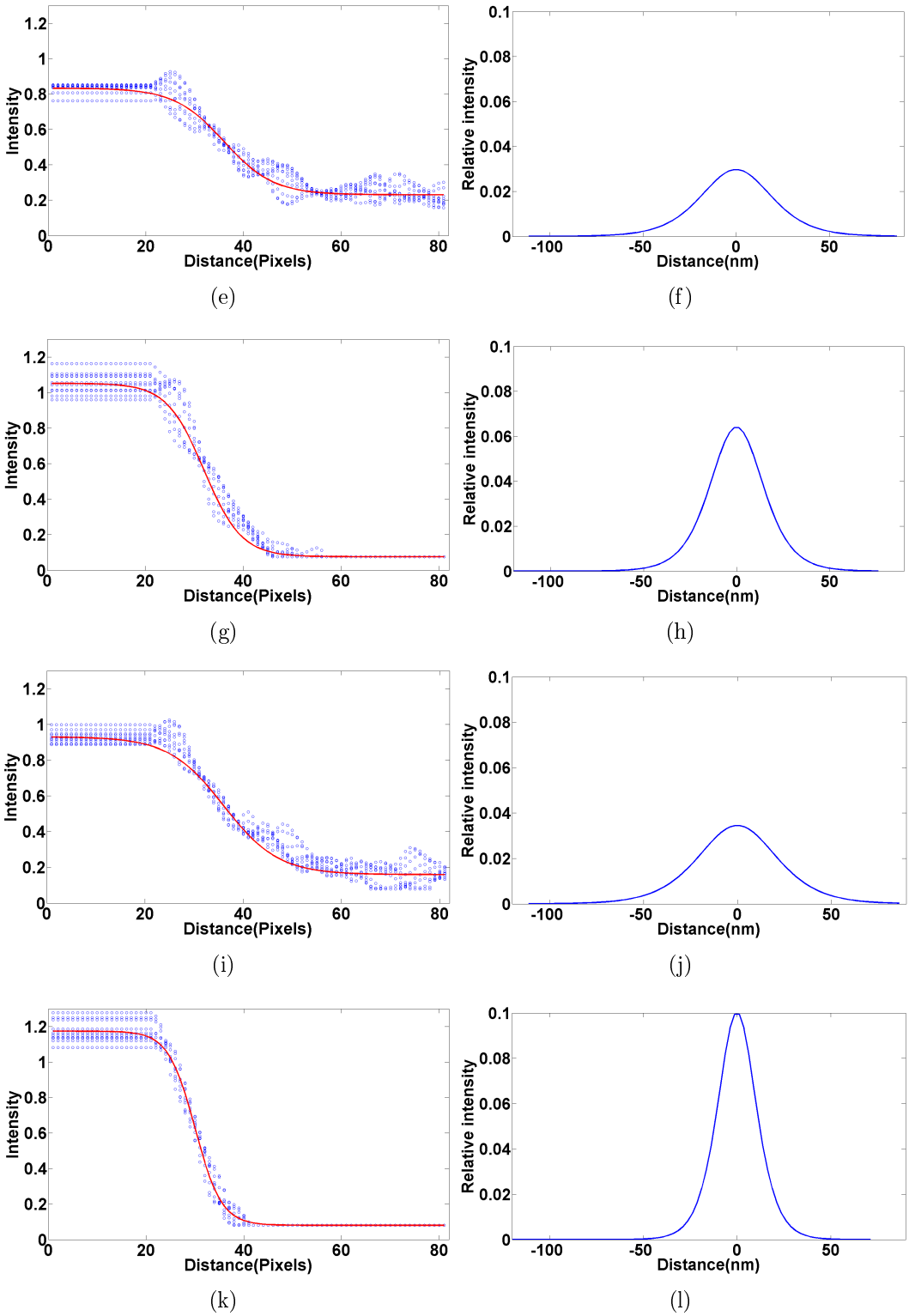

Figure 7.12 *ESF (left columns) and PSF (right columns) of Exp.1-6 in XZ plane from top to bottom. A thin PSF indicates better resolution in Z-direction.*

8. CONCLUSIONS

Generally to create a tomogram of an object, we are required to provide a stack of high quality 2D cross sectional projections in a full angular range. However, in electron tomography neither the quality of the projections nor full angular range around the object is provided. Specimen damage is one of the main limitations in ET which constrains the total electron dose and thus generating high SNR projections. The other main restriction in ET is the blind region of data acquisition called missing wedge. Typically in electron tomography, projections are limited to the range of $\pm$ 60° as a result of physical limitations of the specimen holder, in addition to the long transience path in high angles. Considering the low SNR of the projections, to produce images with relatively acceptable contrast different adjustments of the electron microscope such as defocus value, acceleration voltage and diaphragm aperture size were examined. Results indicate that reducing the acceleration voltage improves the contrast. Since the electron-specimen interaction increases, more electrons are deflected and intercepted which result in a better contrast. However, low acceleration voltage increases the specimen damage due to more inelastic interactions. Note that the acceleration voltage is correlated to the specimen thickness directly: acceleration voltage should be increased for thicker samples. Modifying the defocus value indicates that increasing the defocus value enhances the contrast of the projections, as interfering of the scattered and unscattered electron waves intensifies during the image formation. Nevertheless, it should be considered that defocus increment blurs the high resolution structures in the projections and declines the similarity of the acquired projections to the ground truth. Results of increasing the objective diaphragm size on image formation show enhancement in the brightness of the projections without considerable changes in the contrast. Theoretically, it was expected that low aperture size results in high contrast in the projections, since most of the electrons with high scattering angles will be intercepted by the aperture. However our experimental results imply that declining the number of electrons reaching to the detector intensifies the noise which neutralizes the effect of small aperture size.

Considering the missing wedge in ET, different approaches have been used to smooth its effect in the data acquisition stage such as non-constant dose and angle distribution models. Electrons can be distributed constantly so that all the projections receive equal number of electrons, or non-constantly where the number of electrons irradiating the specimen is related to the cosine of the tilt angles. Results show that among different dose distribution methods, the cosine model produces better tomograms in terms of RMS and resolution. Saving up the electron dose from low angles and spending them on high angles homogenizes the sinograms and compensates for the increment of the transience path. Discussing different angle distribution methods, Saxton's model reduces the elongation artifact more than other methods by elevating the sampling frequency in highly tilted angles. Oversampling the Fourier space of the regions close to the missing wedge increases the accuracy of the reconstructed tomograms. Results of the inverse-Saxton model verify that undersampling the region of high angles worsens the RMS value and the resolution in Z-direction. Moreover, comparing the numerical results shows that the experiment which combines the cosine model of dose distribution with Saxton model is superior in terms of resolution, RMS and elongation among all the experiments. This method, intensifies the SNR of the projections corresponding to the high angles, together with oversampling this region. Thus, it reduces the adverse effects of the slab geometry of the specimen and the missing wedge at the same time.

To conclude, the results of this study are important in low dose electron tomography as they show the possibility of reducing the adverse effects of missing wedge and slab geometry of the specimen in the data acquisition stage while the number of irradiating electrons are highly restricted.

REFERENCES

[1] J. Frank, "Introduction: Principles of electron tomography," in *Electron tomography*, pp. 1–15, New York, NY: Springer, 2006.

[2] C. A. Diebolder, A. J. Koster, and R. I. Koning, "Pushing the resolution limits in cryo electron tomography of biological structures," *Journal of Microscopy*, vol. 248, no. 1, pp. 1–5, 2012.

[3] L. Reimer and H. Kohl, *Transmission electron microscopy*. New York, NY: Springer, 2008.

[4] J. Frank, *Electron tomography*. New York, NY: Springer, 2006.

[5] W. Saxton, W. Baumeister, and M. Hahn, "Three-dimensional reconstruction of imperfect two-dimensional crystals," *Ultramicroscopy*, vol. 13, no. 1-2, pp. 57–70, 1984.

[6] R. Grimm, H. Singh, R. Rachel, D. Typke, W. Zillig, and W. Baumeister, "Electron tomography of ice-embedded prokaryotic cells," *Biophysical Journal*, vol. 74, no. 2, pp. 1031–1042, 1998.

[7] L. Reimer and H. Kohl, "Introduction," in *Transmission electron microscopy*, pp. 1–15, New York, NY: Springer, 2008.

[8] National Physical Laboratory, "Work function." `http://www.kayelaby.npl.co.uk/atomic_and_nuclear_physics/4_3/4_3.html`. accessed Dec. 2015.

[9] L. Reimer and H. Kohl, "Elements of a transmission electron microscope," in *Transmission electron microscopy*, ch. 4, pp. 77–141, New York, NY: Springer, 2008.

[10] H. Rullgård, L.-G. Öfverstedt, S. Masich, B. Daneholt, and O. Öktem, "Simulation of transmission electron microscope images of biological specimens," *Journal of Microscopy*, vol. 243, no. 3, pp. 234–256, 2011.

[11] Matter, "Introduction to electron microscopes." `http://www.materials.ac.uk/elearning/matter/introductiontoelectronmicroscopes/tem/`. accessed Dec. 2015.

[12] P. W. Hawkes, "The electron microscope as a structure projector," in *Electron tomography* (J. Frank, ed.), ch. 3, pp. 83–113, New York, NY: Springer, 2006.

[13] L. Reimer and H. Kohl, "Electron-specimen interactions," in *Transmission electron microscopy*, ch. 5, pp. 141–195, New York, NY: Springer, 2008.

[14] W. Wriggers, "Image formation in the electron microscope." `http://biomachina.org/courses/structures/08.html`. accessed Dec. 2015.

[15] L. Reimer and H. Kohl, "Scattering and phase contrast for amorphous specimens," in *Transmission electron microscopy*, ch. 6, pp. 195–273, New York, NY: Springer, 2008.

[16] J. Yamasaki, M. Mutoh, S. Ohta, S. Yuasa, S. Arai, K. Sasaki, and N. Tanaka, "Analysis of nonlinear intensity attenuation in bright-field tem images for correct 3d reconstruction of the density in micron-sized materials," *Microscopy*, vol. 63, no. 5, pp. 345–355, 2014.

[17] G. Zanetti, J. D. Riches, S. D. Fuller, and J. A. Briggs, "Contrast transfer function correction applied to cryo-electron tomography and sub-tomogram averaging," *Journal of Structural Biology*, vol. 168, no. 2, pp. 305–312, 2009.

[18] V. Lucic, F. Förster, and W. Baumeister, "Structural studies by electron tomography: From cells to molecules," *Annu. Rev. Biochem.*, vol. 74, no. 1, pp. 833–865, 2005.

[19] J.-J. Fernandez, "Computational methods for electron tomography," *Micron*, vol. 43, no. 10, pp. 1010–1030, 2012.

[20] A. J. Koster and M. Barcena, "Cryotomography: Low-dose automated tomography of frozen-hydrated specimens," in *Electron tomography* (J. Frank, ed.), ch. 4, pp. 113–163, New York, NY: Springer, 2006.

[21] N. D. Klein, K. R. Hurley, Z. V. Feng, and C. L. Haynes, "Dark field transmission electron microscopy as a tool for identifying inorganic nanoparticles in biological matrices," *Analytical Chemistry*, vol. 87, no. 8, pp. 4356–4362, 2015.

[22] E. Bladt, "Optimization of electron tomography for the three dimensional study of nanoparticle assemblies," Master's thesis, Universiteit Antwerpen, 2012-2013.

[23] G. McMullan, S. Chen, R. Henderson, and A. Faruqi, "Detective quantum efficiency of electron area detectors in electron microscopy," *Ultramicroscopy*, vol. 109, no. 9, pp. 1126–1143, 2009.

[24] J. M. Zuo, "Electron detection characteristics of a slow-scan ccd camera, imaging plates and film, and electron image restoration," *Microscopy Research and Technique*, vol. 49, no. 3, pp. 245–268, 2000.

[25] L. Dubbeldam, "Eledron spectrometers and voltage measurements," in *Electron beam testing technology* (J. T. L. Thong, ed.), ch. 5, pp. 211–242, New York, NY: Plenum Press, 1993.

[26] M. Barcena and A. J. Koster, "Electron tomography in life science," *Seminars in Cell and Developmental Biology*, vol. 20, no. 8, pp. 920–930, 2009.

[27] G. Owen and S. D., "An introduction to low dose electron tomography-from specimen preparation to data collection," *mod. Res. Educ. Top*, pp. 939–950, 2007.

[28] J. M. Plitzko and W. Baumeister, "Cryoelectron tomography (cet)," *Science of Microscopy*, pp. 535–604, 2007.

[29] P. Unwin and R. Henderson, "Molecular structure determination by electron microscopy of unstained crystalline specimens," *Journal of Molecular Biology*, vol. 94, no. 3, pp. 425–440, 1975.

[30] R. A. Crowther, L. A. Amos, J. T. Finch, D. J. Derosier, and A. Klug, "Three dimensional reconstructions of spherical viruses by fourier synthesis from electron micrographs," *Nature*, vol. 226, no. 5244, pp. 421–425, 1970.

[31] E. Sanchez-Monge Fernandez, "Image reconstruction with missing wedge," Master's thesis, Tampere University of Technology, 2011.

[32] J. C. Russ, *The image processing handbook*. Boca Raton, FL: CRC Press, 2011.

[33] R. C. Gonzalez and P. A. Wintz, *Digital image processing*. Reading, Mass.: Addison-Wesley, 1987.

[34] J. Kaipio and E. Somersalo, *Statistical and computational inverse problems*. New York, NY: Springer, 2005.

[35] U. Ruotsalainen, "Introduction to medical image processing: Lecture 2." *SGN-55006: Introduction to Medical Image Processing*, Tampere University of Technology, Finland, 2014.

[36] J. Jan, *Medical image processing, reconstruction, and restoration*. Boca Raton, FL: Taylor and Francis, 2006.

[37] S. W. Smith, *The scientist and engineer's guide to digital signal processing*. San Diego, Calif.: California Technical Pub., 2002.

[38] L. Seung-Wan, L. Chang-Lae, C. Hyo-Min, P. Hye-Suk, K. Dae-Hong, C. Yu-Na, and K. Hee-Joung, "Effects of reconstruction parameters on image noise and spatial resolution in cone-beam computed tomography," *J. Korean Phys. Soc.*, vol. 59, no. 4, p. 2825, 2011.

[39] Y. Zhang, H.-P. Chan, B. Sahiner, J. Wei, M. M. Goodsitt, L. M. Hadjiiski, J. Ge, and C. Zhou, "A comparative study of limited-angle cone-beam reconstruction methods for breast tomosynthesis," *Med. Phys.*, vol. 33, no. 10, p. 3781, 2006.

[40] S. Siltanen, "Inverse problems." `http://matriisi.ee.tut.fi/courses/MAT-52500/`. accessed Dec. 2015.

[41] A. C. Kak and M. Slaney, *Principles of computerized tomographic imaging*. New York, NY: IEEE Press, 1988.

[42] J. A. Fessler, "Iterative methods for image reconstruction." `http://web.eecs.umich.edu/~fessler/papers/files/talk/08/isbi-slides.pdf`. accessed Dec. 2015.

[43] L. A. Shepp and Y. Vardi, "Maximum likelihood reconstruction for emission tomography," *Journal of Computer Assisted Tomography*, vol. 7, no. 3, p. 571, 1983.

[44] T. Moon, "The expectation-maximization algorithm," *IEEE Signal Process. Mag.*, vol. 13, no. 6, pp. 47–60, 1996.

[45] A. J. Rockmore and A. Macovski, "A maximum likelihood approach to emission image reconstruction from projections," *IEEE Trans. Nucl. Sci.*, vol. 23, no. 4, pp. 1428–1432, 1976.

[46] F. J. Sigworth, P. C. Doerschuk, J.-M. Carazo, and S. H. Scheres, "An introduction to maximum-likelihood methods in cryo-em," *Methods in Enzymology*, pp. 263–294, 2010.

[47] U. Ruotsalainen, "Introduction to medical image processing: Lecture 4." *SGN-55006: Introduction to Medical Image Processing*, Tampere University of Technology, Finland, 2014.

[48] S. Alenius and U. Ruotsalainen, "Generalization of median root prior reconstruction," *IEEE Transactions on Medical Imaging*, vol. 21, no. 11, pp. 1413–1420, 2002.

[49] SVI, "Scientific volume imaging." `https://svi.nl/AiryDisk`. accessed Dec. 2015.

[50] Hyperphysics, "hyperphysics." `http://hyperphysics.phy-astr.gsu.edu/hbase/phyopt/raylei.html`. accessed Dec. 2015.

[51] P. a. Penczek, "Resolution measures in single particle analysis." `http://ncmi.bcm.edu/ncmi/events/workshops/workshops_7/proceeding/Wrks_EMAN_Resolution_05.pdf`. accessed Dec. 2015.

[52] G. Cardone, K. Grünewald, and A. C. Steven, "A resolution criterion for electron tomography based on cross-validation," *Journal of Structural Biology*, vol. 151, no. 2, pp. 117–129, 2005.

[53] H. Heidari Mezerji, W. Van den Broek, and S. Bals, "A practical method to determine the effective resolution in incoherent experimental electron tomography," *Ultramicroscopy*, vol. 111, no. 5, pp. 330–336, 2011.

[54] W. O. Saxton and W. Baumeister, "The correlation averaging of a regularly arranged bacterial cell envelope protein," *Journal of Microscopy*, vol. 127, no. 2, pp. 127–138, 1982.

[55] M. Van Heel, "Similarity measures between images," *Ultramicroscopy*, vol. 21, no. 1, pp. 95–100, 1987.

[56] H. Y. Liao and J. Frank, "Definition and estimation of resolution in single-particle reconstructions," *Structure*, vol. 18, no. 7, pp. 768–775, 2010.

[57] Wwpdb.org, "wwPDB: Worldwide protein data bank." `http://www.wwpdb.org/`. accessed Dec. 2015.

[58] Rcsb.org, "RCSB PDB." `http://www.rcsb.org/pdb/static.do?p=file_formats/pdb/index.html`. accessed Dec. 2015.

[59] E. Grahn, T. Moss, C. Helgstrand, K. Fridborg, M. Sundaram, K. Tars, H. Lago, N. J. Stonehouse, D. R. Davis, P. G. Stockley, and L. Liljas, "Structural basis of pyrimidine specificity in the MS2 RNA hairpin-coat-protein complex.," *RNA (New York, N.Y.)*, vol. 7, pp. 1616–27, nov 2001.

[60] PDB.org, "2BU1." `http://www.rcsb.org/pdb/explore.do?structureId=2bu1`. accessed Dec. 2015.

[61] Wikipedia, "MRC(file format)." `https://en.wikipedia.org/wiki/MRC_%28file_format%29`. accessed Dec. 2015.

[62] Wikipedia, "Spherical aberration." `https://en.wikipedia.org/wiki/Spherical_aberration`. accessed Dec. 2015.

[63] N. Mansurov, "What is chromatic aberration." `https://photographylife.com/what-is-chromatic-aberration`. accessed Dec. 2015.

APPENDIX - DOSE AND ANGLE DISTRIBUTIONS

Table 1 *Precise values of dose and angle distributions in Exp. 1-6. To read the table, firstly define the number of experiment in both dose and angle columns, each tilt angle and its corresponding dose are written in a same row*

Dose dist. (Exp. 1, 4, 5)	Dose dist. (Exp. 2)	Dose dist. (Exp. 3)	Dose dist. (Exp. 6)	Tilt Angle (Exp. 1,2,3)	Tilt Angle (Exp. 4, 6)	Tilt Angle (Exp. 5)
250	395.63	199.11	378.66	-60	-59.99	-59.99
250	384.07	199.15	371.53	-59	-59.35	-58.74
250	373.29	199.24	364.58	-58	-58.7	-57.49
250	363.2	199.39	357.81	-57	-58.04	-56.24
250	353.75	199.6	351.21	-56	-57.36	-54.99
250	344.88	199.88	344.78	-55	-56.68	-53.75
250	336.54	200.21	338.52	-54	-55.98	-52.5
250	328.69	200.61	332.43	-53	-55.27	-51.26
250	321.3	201.07	326.49	-52	-54.54	-50.03
250	314.33	201.6	320.72	-51	-53.8	-48.8
250	307.74	202.19	315.1	-50	-53.05	-47.57
250	301.52	202.84	309.63	-49	-52.29	-46.35
250	295.63	203.56	304.32	-48	-51.51	-45.14
250	290.05	204.35	299.15	-47	-50.72	-43.93
250	284.76	205.21	294.13	-46	-49.91	-42.73
250	279.75	206.14	289.25	-45	-49.09	-41.53
250	274.99	207.14	284.51	-44	-48.26	-40.35
250	270.47	208.21	279.91	-43	-47.42	-39.17
250	266.18	209.36	275.44	-42	-46.56	-38
250	262.1	210.59	271.11	-41	-45.68	-36.84
250	258.23	211.89	266.91	-40	-44.8	-35.69
250	254.54	213.28	262.84	-39	-43.9	-34.55
250	251.03	214.75	258.9	-38	-42.98	-33.42
250	247.69	216.31	255.08	-37	-42.05	-32.31
250	244.51	217.96	251.39	-36	-41.11	-31.2
250	241.48	219.7	247.82	-35	-40.16	-30.1
250	238.61	221.54	244.37	-34	-39.19	-29.02
250	235.86	223.47	241.03	-33	-38.21	-27.95
250	233.26	225.51	237.82	-32	-37.21	-26.89
250	230.78	227.66	234.72	-31	-36.2	-25.84
250	228.41	229.92	231.73	-30	-35.18	-24.81
250	226.17	232.29	228.85	-29	-34.15	-23.79
250	224.04	234.79	226.09	-28	-33.1	-22.78
250	222.01	237.42	223.43	-27	-32.04	-21.78
250	220.09	240.18	220.89	-26	-30.97	-20.8
250	218.26	243.07	218.45	-25	-29.88	-19.83
250	216.53	246.12	216.11	-24	-28.79	-18.87
250	214.9	249.32	213.88	-23	-27.68	-17.93
250	213.35	252.68	211.76	-22	-26.56	-17.01
250	211.89	256.21	209.73	-21	-25.43	-16.09
250	210.51	259.93	207.81	-20	-24.29	-15.19
250	209.21	263.83	205.98	-19	-23.15	-14.3
250	207.99	267.94	204.26	-18	-21.99	-13.43
250	206.85	272.26	202.63	-17	-20.82	-12.57

250	205.78	276.8	201.1	-16	-19.64	-11.72
250	204.79	281.59	199.67	-15	-18.45	-10.89
250	203.87	286.64	198.34	-14	-17.26	-10.07
250	203.02	291.96	197.1	-13	-16.06	-9.27
250	202.23	297.57	195.95	-12	-14.85	-8.48
250	201.52	303.5	194.9	-11	-13.64	-7.7
250	200.86	309.77	193.94	-10	-12.42	-6.94
250	200.28	316.4	193.07	-9	-11.19	-6.18
250	199.76	323.42	192.3	-8	-9.96	-5.45
250	199.3	330.86	191.62	-7	-8.72	-4.72
250	198.9	338.75	191.03	-6	-7.48	-4.01
250	198.57	347.15	190.53	-5	-6.24	-3.31
250	198.3	356.08	190.13	-4	-5	-2.62
250	198.08	365.59	189.81	-3	-3.75	-1.95
250	197.93	375.75	189.58	-2	-2.5	-1.29
250	197.84	386.6	189.45	-1	-1.25	-0.64
250	197.81	398.23	189.4	0	0	0
250	197.84	386.6	189.45	1	1.25	0.64
250	197.93	375.75	189.58	2	2.5	1.29
250	198.08	365.59	189.81	3	3.75	1.95
250	198.3	356.08	190.13	4	5	2.62
250	198.57	347.15	190.53	5	6.24	3.31
250	198.9	338.75	191.03	6	7.48	4.01
250	199.3	330.86	191.62	7	8.72	4.72
250	199.76	323.42	192.3	8	9.96	5.45
250	200.28	316.4	193.07	9	11.19	6.18
250	200.86	309.77	193.94	10	12.42	6.94
250	201.52	303.5	194.9	11	13.64	7.7
250	202.23	297.57	195.95	12	14.85	8.48
250	203.02	291.96	197.1	13	16.06	9.27
250	203.87	286.64	198.34	14	17.26	10.07
250	204.79	281.59	199.67	15	18.45	10.89
250	205.78	276.8	201.1	16	19.64	11.72
250	206.85	272.26	202.63	17	20.82	12.57
250	207.99	267.94	204.26	18	21.99	13.43
250	209.21	263.83	205.98	19	23.15	14.3
250	210.51	259.93	207.81	20	24.29	15.19
250	211.89	256.21	209.73	21	25.43	16.09
250	213.35	252.68	211.76	22	26.56	17.01
250	214.9	249.32	213.88	23	27.68	17.93
250	216.53	246.12	216.11	24	28.79	18.87
250	218.26	243.07	218.45	25	29.88	19.83
250	220.09	240.18	220.89	26	30.97	20.8
250	222.01	237.42	223.43	27	32.04	21.78
250	224.04	234.79	226.09	28	33.1	22.78
250	226.17	232.29	228.85	29	34.15	23.79
250	228.41	229.92	231.73	30	35.18	24.81

250	230.78	227.66	234.72	31	36.2	25.84
250	233.26	225.51	237.82	32	37.21	26.89
250	235.86	223.47	241.03	33	38.21	27.95
250	238.61	221.54	244.37	34	39.19	29.02
250	241.48	219.7	247.82	35	40.16	30.1
250	244.51	217.96	251.39	36	41.11	31.2
250	247.69	216.31	255.08	37	42.05	32.31
250	251.03	214.75	258.9	38	42.98	33.42
250	254.54	213.28	262.84	39	43.9	34.55
250	258.23	211.89	266.91	40	44.8	35.69
250	262.1	210.59	271.11	41	45.68	36.84
250	266.18	209.36	275.44	42	46.56	38
250	270.47	208.21	279.91	43	47.42	39.17
250	274.99	207.14	284.51	44	48.26	40.35
250	279.75	206.14	289.25	45	49.09	41.53
250	284.76	205.21	294.13	46	49.91	42.73
250	290.05	204.35	299.15	47	50.72	43.93
250	295.63	203.56	304.32	48	51.51	45.14
250	301.52	202.84	309.63	49	52.29	46.35
250	307.74	202.19	315.1	50	53.05	47.57
250	314.33	201.6	320.72	51	53.8	48.8
250	321.3	201.07	326.49	52	54.54	50.03
250	328.69	200.61	332.43	53	55.27	51.26
250	336.54	200.21	338.52	54	55.98	52.5
250	344.88	199.88	344.78	55	56.68	53.75
250	353.75	199.6	351.21	56	57.36	54.99
250	363.2	199.39	357.81	57	58.04	56.24
250	373.29	199.24	364.58	58	58.7	57.49
250	384.07	199.15	371.53	59	59.35	58.74
250	395.63	199.11	378.66	60	59.99	59.99